An adjoint model for the determination of the mean oceanic circulation, air-sea fluxes und mixing coefficients

Bestimmung von mittlerer ozeanischer Zirkulation, Oberflächenflüssen und Mischungskoeffizienten mittels der Adjungierten Methode

---

Reiner Schlitzer

Ber. Polarforsch. 156 (1995)
ISSN 0176 - 5027

Reiner Schlitzer

Fachbereich 1
Universität Bremen
Postfach 330440
28334 Bremen

jetzt

Alfred Wegener Institut für Polar und Meeresforschung
Postfach 120161
27515 Bremerhaven
Bundesrepublik Deutschland

Printed version of a habilitation thesis submitted to and accepted by the Physics Department of the University of Bremen (October, 1993).

Die vorliegende Arbeit ist die inhaltlich unveränderte Fassung einer Habilitationsschrift, die im Oktober 1993 vom Fachbereich Physik der Universität Bremen angenommen wurde.

Contents

Zusammenfassung ii
Summary iv

1 **Introduction** 1

2 **Hydrographic Station Data** 7
2.1 Spatial and Temporal Data Coverage 7
2.2 Use of the Hydrographic Data in the Model 10

3 **Model Setup and Strategy** 19
3.1 Model Grid and Geometry 19
3.2 Parameters and Model Equations 20
3.3 Clusters 22
3.4 Mixing Tensor 23
3.5 Cost Function 25
3.6 Adjoint Model 28

4 **Initialization of Model Parameters** 31
4.1 Pre-optimization 31
4.2 Iterative Procedure 32
4.3 "Independent Layer" Approach 35

5 **Model Calculations and Results** 39
5.1 Overview of Numerical Experiments 39
5.2 Calculations with the Upwind Differencing Scheme (UPW) 40
5.3 Calculations with the Centered-in-Space Differencing Scheme (CS) 68
5.4 Diapycnal Mixing Linked to Stability (CS-N) 73
5.5 Adding Heat Flux Constraints (CS-H) 76

6 **Discussion and Conclusions** 87

Acknowledgments 95

References 97

Zusammenfassung

In der vorliegenden Arbeit wird ein neues Modellkonzept zur Bestimmung der mittleren, großräumigen ozeanischen Zirkulation sowie von Oberflächenwärmeflüssen und Mischungskoeffizienten vorgestellt. Dieses Konzept beruht auf der sogenannten Adjungierten Methode und hat die Einbeziehung und Nutzung großer Mengen hydrographischer Daten zum Ziel. Es werden dabei mit dem Modell Strömungsfelder bestimmt, die mit den beobachteten Verteilungen von Temperatur und Salz als auch mit den aus geostrophischen Berechnungen gewonnenen Geschwindigkeitsscherungen konsistent sind. Das verwendete Modell überdeckt den gesamten Atlantik und hat realistische Topographie. Die Auflösung des Modellgitters reicht von 2.5×2.5° bis 10×10° in der Horizontalen und von 60 m bis 500 m in der Vertikalen. Als Anfangswerte der Strömungen im Modell werden aus den hydrographischen Daten berechnete geostrophische Geschwindigkeiten verwendet. Anfangswerte für Oberflächenwärmeflüsse und Mischungskoeffizienten werden der Literatur entnommen. Das Modell erfüllt Masse-, Wärme- und Salzerhaltungsgleichungen exakt und berechnet aus diesen und den aus den Daten berechneten Randbedingungen Modellverteilungen für Temperatur und den Salzgehalt. Das Modell vergleicht dann die simulierten Verteilungen mit den Temperatur- und Salzdaten und ermittelt aus der festgestellten Struktur der Abweichungen automatisch (mittels der Adjungierten Methode) einen Satz geänderter Strömungsgeschwindigkeiten, Oberflächenwärmeflüsse und Mischungskoeffizienten, der zu einer besseren Temperatur- und Salzsimulation führt. Die Optimierung der Modellströmungen erfolgt iterativ bis die bestmögliche Übereinstimmung zwischen Modellwerten und Beobachtungen erreicht ist. Dabei wird gewährleistet, daß die vertikalen Geschwindigkeitsscherungen nur wenig von geostrophischen Profilen abweichen.

Die Modellrechnungen zeigen, daß die Modellziele tatsächlich erreicht werden können und daß simulierte Verteilungen erzeugt werden, die sehr nahe bei den Beobachtungen liegen. Die Geschwindigkeitsscherungen der dazu notwendigen Strömungen weichen kaum von den geostrophischen Scherungen ab. Um bestmögliche Übereinstimmung von Modell und Daten zu erzielen, müssen die Werte für diapyknische Mischungskoeffizienten relativ klein gewählt werden. Setzt man Mischungskoeffizienten als konstant im gesamten Modellgebiet an, so ist ein Wert von $K_v = 0.4 \cdot 10^{-4}$ m^2 s^{-1} optimal, während bei einer Parametrisierung der diapyknischen Mischung mit der inversen Brunt-Väisälä Frequenz die besten Werte zwischen 0.1 $\cdot 10^{-4}$ m^2 s^{-1} in der Thermokline des tropischen Ozeans und 1.5 $\cdot 10^{-4}$ m^2 s^{-1} in den schwach geschichteten Wasserkörpern der polaren Becken und des tiefen Ostatlantiks liegen. Sensitivitätsläufe deuten auf eine Schwankungsbreite von ±100% bei diesen Werten. Bei allen Modelläufen zeigt sich ein Überwiegen der Verdunstung gegenüber dem Niederschlag zwischen 0.17 und 0.3 Sv im Atlantik. Mit Ausnahme des Weddell Beckens nimmt der Südatlantik Wärme aus der Atmosphäre auf. Dabei werden mit ca. 45 W m^{-2} die größten Werte am nördlichen Rand des Zirkumpolarstromes zwischen 40 and 60°S erreicht.

Die zonal integrierte meridional Zelle der Modellströmungen zeigt nordwärts gerichteten Transport im Oberflächen-, Zwischen- und Bodenwasser und nach Süden fließendes nordatlantisches Tiefenwasser dazwischen. Dabei wird im Südatlantik der nordwärts gerichtete Fluß in den obersten 1500 m Tiefe hauptsächlich durch Antarktisches Zwischen-wasser hervorgerufen, während der Beitrag des warmen Oberflächenwassers vergleichsweise gering ist. Erst im äquatorialen und subtropischen Nordatlantik überwiegt der Transport des warmen Oberflächenwassers den des Zwischenwassers. Im polaren Nordatlantik und im Weddell Becken findet man im Modell Tiefen- und Bodenwasserbildung. Absinken von Wasser zeigt sich außerdem in den Zentren der subtropischen Wirbeln, während im Südatlantik zwischen 45 and 65°S und im äquatorialen Atlantik Auftrieb überwiegt. Die Vertikaltransporte in 60 m Tiefe stimmen gut mit den aus Winddaten bestimmten Ekman-Divergenzen überein. Gute Übereinstimmung mit den hydrographischen Daten konnte im Modell für eine Vielzahl von Strömungsfeldern gefunden werden. Diese Strömungsfelder unterscheiden sich teilweise stark in der Stärke der meridionalen Zelle und der Größe des meridionalen Wärmeflusses. Ähnliche Ergebnisse wurden auch mit anderen Inversmodellen erzielt, und es scheint, daß der Informationsgehalt hydrographischer Daten nicht ausreicht, um integrale Transportraten weiter einzugrenzen. Offensichtlich ist die Einbeziehung weiterer, unabhängiger Messungen notwendig, um zu Verbesserungen zu gelangen. Zu diesem Zweck ist an eine Erweiterung des hier vorgestellten Modellkonzeptes gedacht, die die Nutzung von Daten zeitabhängiger Spurenstoffe (z.B. FCKW) im Ozean erlaubt. Erste Simulationen der ozeanischen FCKW Verteilung mit den hier vorgestellten Strömungsfeldern zeigen systematische Abweichungen von den Messungen, und man kann daher erwarten, daß diese zusätzlichen Daten zu einer besseren Einschränkung der möglichen Lösungen führt.

Summary

A new model approach based on the adjoint formalism and aimed at assimilating large sets of hydrographic data is presented. Goal of the model calculations is to obtain the mean, large-scale ocean circulation together with coefficients of iso- and diapycnal mixing and air-sea heat and fresh-water fluxes. Consistency with the measured distributions of temperature and salinity and with the principle of geostrophy is enforced. The model covers the entire Atlantic and has realistic topography. Model resolution is non-uniform and ranges from 2.5° to 10° horizontally and from 60 m to 500 m in the vertical. Model velocities are initialized with geostrophic flows calculated from original hydrographic station-data, and initial air-sea heat fluxes and mixing coefficients are taken from the literature. Mass, heat and salt budgets are satisfied exactly, and for given boundary conditions and model flows the model temperature and salinity distributions are calculated. Then horizontal flows and the air-sea fluxes are modified automatically (in directions provided by the adjoint model) until deviations between model temperatures and salinities and their measured counterparts (data) are minimized while keeping the vertical shear of the horizontal velocities (as given by the initial geostrophic flows) largely unchanged.

Model results show that the model temperature and salinity fields can indeed be brought to close agreement with the observed distributions. Modifications to the initial horizontal flows needed to achieve this agreement are found to consist mainly of constant velocity shifts in the vertical profiles. The final, optimal flow field thus is consistent with geostrophic dynamics and the present model can be regarded as a new approach to the classical problem of calculating reference velocities from hydrographic data. Different numerical experiments show that in order to obtain satisfactory agreement between model θ and salinity fields with observations small diapycnal mixing coefficients are required. In the case of constant coefficients in the entire model domain the optimal value is about $K_v = 0.4 \cdot 10^{-4}$ m^2 s^{-1}, and for a parameterization of diapycnal mixing with the inverse Brunt-Väisälä frequency K_v ranges from about $0.1 \cdot 10^{-4}$ m^2 s^{-1} in the thermocline of the tropical Atlantic to about $1.5 \cdot 10^{-4}$ m^2 s^{-1} in the weakly stratified waters below 500 m depth in the polar oceans and in the deep eastern Atlantic. Sensitivity runs show that acceptable solutions can be obtained with mixing coefficients within about ±100% of above values. All model solutions for the different cases considered show net fresh-water loss of the Atlantic (between 0.17 and 0.3 Sv) and net air-sea heat gain. With the exception of Weddell Sea, the south Atlantic almost everywhere is receiving heat, and a belt of relatively large heat gain (up to 45 W m^{-2}) is found along the path of the Antarctic Circumpolar Current between 40 and 60°S.

Zonally integrated model flows show a meridional overturning cell consisting of northward transport of intermediate, near-surface and bottom water which compensates the southward flow of North Atlantic Deep Water. In the south Atlantic the northward transport within the upper 1500 m consists mainly of intermediate water (Antarctic Intermediate Water); at the equator warm, near-surface water and intermediate water contribute about equally, and in the north Atlantic the northward transport is mainly in the surface layer. Deep and bottom water formation is observed in the Nordic Seas and in Weddell Sea. Between 45 and 65°S and in the equatorial region upwelling occurs whereas downwelling dominates in the centers of the subtropical gyres. Although not enforced by explicit constraints, zonally integrated vertical transports in 60 m depth correspond roughly with estimates of (zonally integrated) Ekman divergences. Satisfying model temperature and salinity distributions could be obtained for model circulations differing considerably in the strength of the respective meridional overturning cells and in the magnitude of the corresponding oceanic meridional heat transport. This result indicates a relatively large degree of uncertainty for the absolute strength of the meridional overturning cell, a finding that is in line with results of inverse models which are based on temperature and salinity data only. It is proposed, and intended as future model development, to include transient tracer distributions as additional constraints within the present model concept and require that the model not only reproduces realistic temperature and salinity fields but also matches the available tracer measurements. Simulations of the chlorofluoromethanes CFM-11 and CFM-12 using the present model solutions show systematic differences between model concentrations and data which indicates that independent information can be drawn from the tracer fields.

Chapter 1

Introduction

Maps of ocean currents often found in atlases, encyclopedias and oceanographic textbooks (see Fig. 1 for an example) tend to suggest that after almost one hundred years of research, oceanographers have discovered and identified all major current systems in the ocean and know the exact position and strength of the flows. This is not the case, even not for the surface circulation of the ocean, which, compared to deep flows, is easiest to observe and for which the longest history of data exists. Flow charts like in Fig. 1 rather have to be considered as attempts to combine diverse pieces of information which contain errors, are non-synoptic and fall far short of adequately describing the full complexity of ocean dynamics which begins to become apparent from the growing set of oceanographic data.

A major effort to improve our knowledge about the ocean circulation is currently underway (World Ocean Circulation Experiment, WOCE). Major goals of WOCE are "to develop models useful for predicting climate change and to collect the data necessary to test them" (WOCE, 1988). Within these general objectives the determination of the mean, large-scale circulation and the associated fluxes of heat and other properties in the ocean plays an important role. An understanding of the overall circulation patterns and the quantitatively correct determination of mean transport rates is seen as a prerequisite for the study of the full, complex system and for the purpose of making realistic forecasts on climate changes over long time-scales, knowledge of the mean oceanic transports of properties like heat and CO_2 is essential.

Most of the current knowledge about mean, large-scale ocean transport is derived from hydrographic data together with the principle of geostrophy. Due to the problem of unknown reference velocities, however, it is not possible to derive absolute velocities or realistic integrated transports from geostrophy alone, and usually the assumption is made that flow velocities vanish at some great depth (reference level). With typical velocities in most parts of the deep ocean on the order of $1 \cdot 10^{-2}$ m s^{-1} the error made by assuming the deep currents to be zero is relatively small for strong surface currents (e.g., Gulf Stream, Brazil Current, etc.) and, as a consequence, overview maps of ocean currents as in Fig. 1 are not affected much by different choices of deep reference velocities. Integrated transports of water and properties, however, depend strongly on the choice of reference velocity or reference depth. As a result, value ranges of transport estimates of, for instance, the southward

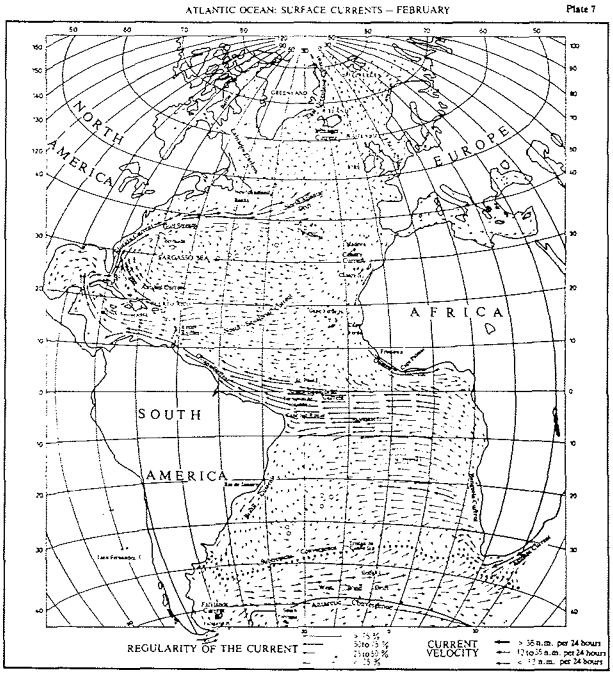

Adapted from G. SCHOTT (1944)

Fig. 1: Surface currents in the Atlantic in February (from: Tchernia, 1980).

flow of North Atlantic Deep Water (NADW) or the meridional transport of heat in the Atlantic shown in Fig. 2 are very large.

Numerous approaches have been developed to overcome the deficiency of the geostrophic method and to calculate absolute velocities by making use of distributions of additional properties (Wüst, 1935; Reid, 1989) and/or by applying additional dynamical equations or property conservation budgets (inverse methods: Schott and Stommel, 1978; Wunsch and Grant, 1982; Schlitzer, 1988). Dynamical models (Bryan, 1969) that are based on the momentum equation (or approximations of it) and are driven by winds and surface fluxes of fresh-water and heat are able to reproduce the diversity of small-scale and short-term phenomena in the ocean. However, it appears that integrated transports of mass or heat in these models are strongly dependent on details of the forcing fields (winds and surface fluxes). Because the ocean wind field and the air-sea surface fluxes are among the least-well known parameters of ocean research, attempts have been made to reduce the influence of the surface forcing on the model results by coupling the dynamical model stronger to hydrographic data in the ocean interior (Sarmiento and Bryan, 1982, Tziperman

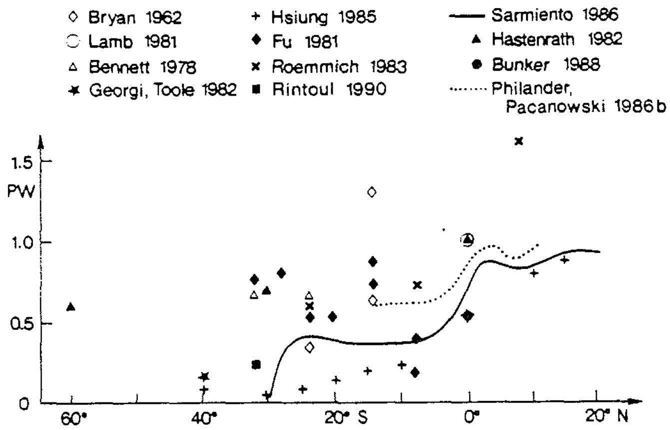

Fig. 2: Total northward heat transport (PW=10^{15} W) of the south and tropical Atlantic Ocean (from: Peterson and Stramma, (1991); their Fig. 28).

and Thacker, 1989). Drawbacks are the abandonment of exact property conservation or the immense computational cost of the model calculations.

The present model approach contains ideas and elements from many of the above-mentioned methods but differs widely with respect to putting different emphasis on data, dynamical equations and conservation laws and by using a new mathematical formulation which is based on the adjoint method (Le Dimet and Talagrand, 1986; Thacker, 1988b; Thacker, 1988a). As will be described in detail below, integral equations like mass, heat and salt budgets for the control volumes (boxes) of the model are considered the most important model equations and are satisfied exactly, whereas the vaguely known forcing parameters at the ocean surface and differential properties like geostrophic flow velocities, obtained as differences of nearby dynamic heights, are enforced in an approximate sense only. This strategy reflects the observation that integral quantities (like property distributions in the ocean) are known better and change less with time compared with, for instance, the surface forcing parameters wind, heat and fresh-water fluxes and compared with differential properties like dynamic height differences.

The dynamical principles of geostrophy, Ekman drift and linear vorticity balance are incorporated in the present model, however, these are treated as soft constraints and the model is allowed to deviate from these principles. This is a major difference to the approach of Tziperman and Thacker (1989) who also is using the adjoint technique and is aiming at the mean ocean circulation but whose model puts more emphasis on the dynamical principles (by applying approximated time-dependent momentum equations). Whereas Tziperman has to enforce stationarity of the circulation by additional terms in the cost function of his system, here, stationarity is assured by design of the model.

As a fundamental property of a steady model, conservation of mass, heat and salt is strictly enforced in the present approach. It is realized that flows calculated from available hydrographic data non-uniformly distributed in space and time are likely to be in disagreement with continuity. This has been shown, for example, by Wunsch and Grant (1982) who used non-synoptic hydrographic sections in their model and observed especially large mass divergences in the Gulf Stream region caused by temporal changes of the stream's position. Because of the steady-state condition, here, conservation laws are considered most important, and the standpoint is taken, that in order to satisfy them, the flows should be modified, not because geostrophy was invalid but because data coverage is expected to be insufficient to represent the true, mean state of the ocean or because errors in the hydrographic data lead to erroneous geostrophic flows. Thus, allowing the vertical shear of the model flows to deviate from the initial, geostrophic shear should not be regarded as abandonment of the principle of geostrophy but rather as a way to deal with doubts, whether the available hydrographic data correctly represent the mean, large-scale oceanic flows. Uncertainties of the vertical velocity shear from geostrophic calculations (including Ekman transports near the surface) are estimated, and the model velocity shear is only required to match the initial, geostrophic shear within these error margins.

This approach is different from, for instance, the inverse calculations of Wunsch and Grant (1982) who accept the geostrophic shear from hydrographic sections as being exact while compromising on mass, heat and salt conservation. Locally, the resulting flows of Wunsch and Grant are closely linked to the individual, non-synoptic hydrographic sections incorporated in their model and the overall circulation field represents a composite of instantaneous flows across different sections at different times. For the present model, conservation laws are not only important because of the emphasis on the long-term, steady ocean circulation, but satisfying them exactly is also a pre-requisite for the temperature, salinity and, in future, tracer simulations performed by the model. Any mass imbalance δm of a given control volume or box influences the corresponding property budgets (see below) by introducing artificial (non-physical) heat, salt and tracer sources or sinks of magnitude $Q_a \approx \delta m \cdot \bar{c}$ ($\bar{c}$ being the mean property concentration on the surfaces of the box). A positive imbalance ($\delta m > 0$, more water is entering the box than leaving) is equivalent to a net, artificial production of tracer inside the box whereas a negative mass imbalance ($\delta m < 0$, more water leaving than entering) results in a net, artificial decay. For the heat, salt and tracer simulations incorporated in the present model it is essential to avoid artificial property sources or sinks and this is ensured by requiring exact mass balances ($\delta m = 0$).

In inverse models (Wunsch, 1984b; Wunsch and Grant, 1982; Schlitzer, 1989; Schlitzer, 1988; Schlitzer, 1987; Rintoul, 1991), typically, closed volumes or boxes are defined using hydrographic sections and a vertical subdivision into isopycnal or constant depth layers. For the resulting boxes conservation equations are formulated. These include in most cases mass, heat and salt budgets, but, for instance, silicate or radiocarbon (^{14}C) budgets can be incorporated as well (Schlitzer, 1987). Taking the concentration values that appear in the advective and diffusive terms of the property budgets from observations (section data) leaves a set of linear equations that can be solved easily for the unknown flow velocities or reference velocities (Wunsch and Minster, 1982). Because the coefficients of the system are derived from data and contain errors, certain imbalances are tolerated in the budget equations. The advantage of this approach is that solutions and error covariances of the solutions can be obtained efficiently. A serious drawback is the requirement that measurements must be available on all interfaces of the model grid in order to define the model coefficient matrix. For models using only the basic hydrographic properties temperature and salinity this is not a serious restriction because of the large amount of available temperature and salinity measurements. However, for transient tracers like chlorofluoromethanes (CFMs) or tritium, which exhibit time-evolving oceanic distributions and for which much less data are available compared to T and S, very rarely sufficient observations are available for a given time to reliably define tracer concentrations on box interfaces or the time-rate of change of the tracer within a box.

With a future model evaluation of transient tracer data in mind, the present model is designed to be less demanding on completeness of the available data sets while still allowing to exploit the limited amounts of existing (tracer) data. It will be seen in detail below that mass, heat, salt and tracer (future development) budgets are satisfied exactly by the model and acceptable steady flow fields, air-sea fluxes and mixing coefficients are required to reproduce (or correctly simulate) the observed distributions of temperature, salt and tracer. Consistency with observations is checked and enforced for all boxes for which data are available. Given the large set of hydrographic data, model versus measurement comparisons for temperature and salinity can be made almost everywhere in the model domain. In contrast, consistency checks with, for instance, oceanic CFMs are usually restricted to small regions and a single time for which CFM data are available. These two *scenarios* are treated formally equally by the model, the only difference being that fewer model/data comparisons lead to weaker constraints on the final model solution. In addition to reproducing realistic property fields the vertical velocity shear of the horizontal model flows is required to be close to the vertical shear of geostrophic velocity profiles obtained from the hydrographic data. This constraint is equivalent to the traditional notion that the velocity shear or the shape of velocity profiles can be determined using the geostrophic method, but that a constant velocity offset (called the reference velocity) remains to be determined. It should be noted that at present the model is realized with temperature and salinity data only.

The optimal model solution (mean circulation, air-sea fluxes and mixing coefficients) is obtained iteratively, starting with geostrophic horizontal flows (calculated relative to a conveniently chosen reference level; here: 2500 db) and values for air-sea heat fluxes and iso- and diapycnal mixing coefficients taken from the literature. For this set of independent model parameters vertical flows as well as simulated model temperatures and salinities are calculated by solving mass-, heat- and salt conservation equations exactly. These dependent model parameters are compared with data (temperature and salinity data, estimates of air-sea fresh water fluxes, etc.) and consistency with data is measured by an overall model-data misfit (cost function F). The independent model parameters are then modified in a systematic way (determined by the adjoint model described below) that guarantees a subsequent decrease of the model-data misfit. This iterative procedure is repeated until the model-data misfit is minimal. At that point it has to determined to which degree the overall model goals have been satisfied, the resulting, optimal model flow field appearing most valuable when realistic simulations of temperature and salinity could be obtained with model vertical velocity shear as given by geostrophy.

In contrast to dynamical models (Bryan, 1969; Sarmiento and Bryan, 1982; Tziperman and Thacker, 1989), that include the time-evolution of oceanic flows and usually are able to reproduce, for example, seasonal variations of the velocity fields, in the present study, model flows are steady and represent the long-term mean ocean circulation. As a consequence, processes in the ocean that are known to be time dependent like for instance sporadic deep water formation or winter convection events can not be resolved (in time) in this model. Instead, the present model will try to reproduce the net effects of, for instance, deep water formation on temperature, salinity and tracer fields with a time-mean downwelling or deep water formation rate. Thus, care should be taken when comparing vertical velocities of the model in deep water formation areas with direct velocity measurements during convective events. Restriction to steady flows, as in the present model, represents an oversimplification of the real oceanic dynamics and, at the outset, it is not clear whether realistic temperature or salinity simulations can be obtained. In the deep water formation areas, it appears to be impossible to produce the observed, low temperatures of the deep and bottom waters by downward convection of surface waters with the relatively high annually averaged temperatures, and it can be expected that model surface temperatures and salinities in the formation areas will be biased towards the respective winter values.

The paper starts in section 2 with a description of the set of hydrographic data used for the present model study. Then, in section 3, the model strategy and a model setup for the Atlantic Ocean are presented; section 4 describes how the model is initialized, and in section 5 results of various numerical experiments are shown and discussed in the context of present-day oceanographic knowledge. Finally, conclusions are drawn and ideas for future model development are presented in section 6.

Chapter 2

Hydrographic Station Data

2.1 Spatial and Temporal Data Coverage

Fig. 3 shows the map of hydrographic stations used in this study. The data set was obtained by merging several large data atlases: (1) the Southern Ocean Atlas of Gordon *et al.* (1986), (2) a set of about 1200 additional, new stations in the south Atlantic (W. Nowlin, priv. communication), (3) a set of about 3000 stations covering the entire Atlantic (J. Reid, priv. communication), (4) a set of about 1200 stations from the north Atlantic occupied during the early 1980s (Fukumori *et al.*, 1991), and (5) a large number of hydrographic stations from the US NODC global archive that were not included in the other data sets. In total, the collection contains more than 9000 stations most of which contain top to bottom measurements. As can be seen in Fig. 3 the overall data coverage is good, however, even with a large data set like the present one some areas in the central south Atlantic, the western Weddell Sea and the Arctic Ocean remain poorly sampled.

The temporal distribution of the station data for three regions of the Atlantic (Nordic Seas [60°N - 90°N], central Atlantic [50°S - 60°N], Antarctic region [80°S - 50°S]) is shown in Fig. 4. Overall, the hydrographic data cover a period of almost 70 years from the early 1920's up to the present time. For the three regions considered, the Antarctic region exhibits the widest spread in time with a relatively large number of old stations from, for instance, the *Meteor* and *Discovery* expeditions (period from 1925 to 1939; Wüst, 1935; Deacon, 1937) together with more recent data between 1955 and 1990 which are most numerous in the mid 1970's (*ISOS*, Nowlin *et al.* 1977). In the central Atlantic and especially in the Nordic Seas the observations tend to fall into a narrower, more recent time interval with maxima around 1960 and 1980. Major expeditions (e.g., IGY, 1957-1958; GEOSECS, 1972-1973; TTO, 1981-1983) can easily be identified by individual peaks in the historical station distributions.

Fig. 4 also shows the number of stations for the different months of the year. In the central Atlantic (Fig. 4b) more stations have been occupied during February, March and April compared with other months, but on the average all seasons seem to be adequately represented. The situation is different in the subpolar and polar regions both in the north

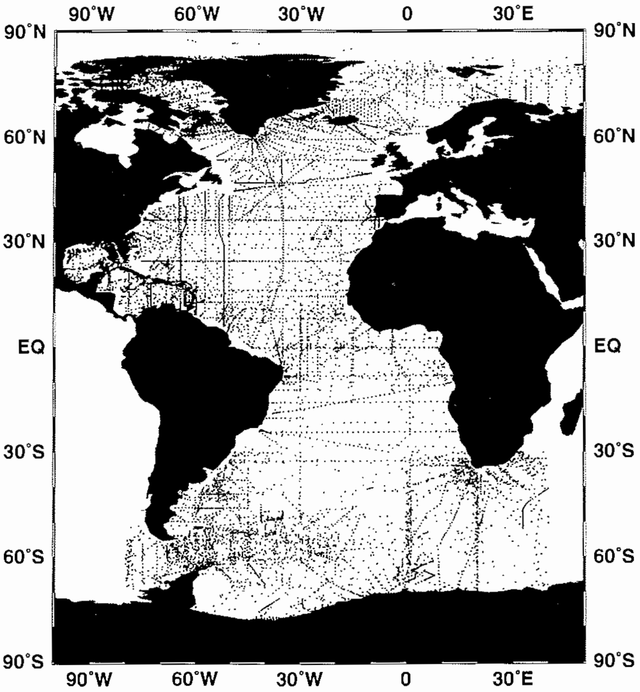

Fig. 3: Map of hydrographic stations used in this study. The data set contains more than 9000 stations most of which contain top to bottom measurements.

(a) 60°N - 90°N

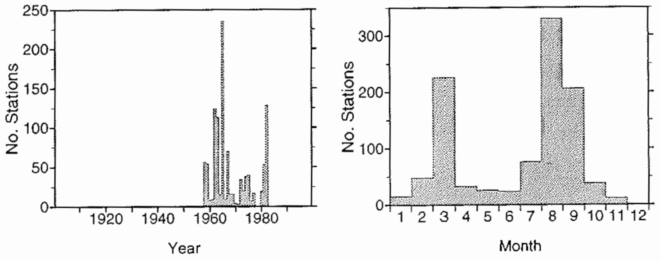

(b) 50°S - 60°N

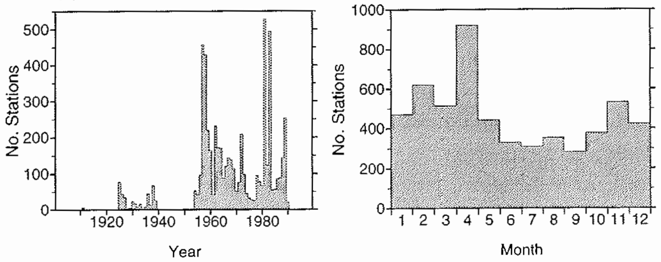

(c) 90°S - 50°S

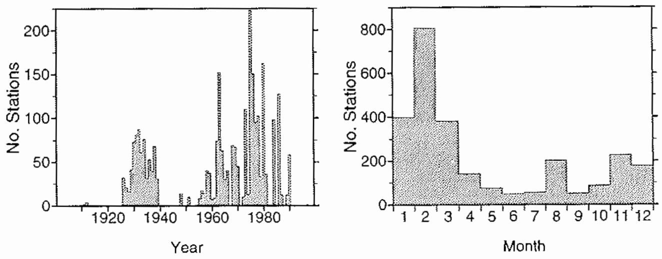

Fig. 4: Temporal distribution of available station-data for three regions of the Atlantic: (a) Nordic Seas, (b) central Atlantic and (c) southern Atlantic.

and south Atlantic (Figs. 4a and 4c). Due to unfavorable weather and ice conditions during winter and also due to the remoteness of these areas, observations tend to occur mainly during the respective summer months, and usually very few stations are occupied during the rest of the year and especially in winter and spring, when, from a scientific point of view, it might be most interesting to make the measurements. In the Nordic Seas a relatively large number of observations were made during March, probably reflecting the interest in deep water formation and winter convection processes, but summer data still dominate. The obvious bias of the observations in the polar and subpolar regions towards the respective summer seasons and possible consequences for the present study will be discussed below.

2.2 Use of the Hydrographic Data in the Model

The hydrographic data enter the model in their original form and the model does not depend on the availability of a gridded data set. This is a major difference to many other ocean circulation models which use the Levitus (1982) or Gordon *et al.* (1986) data sets. As described below, averaging of the original data over length scales comparable to the model resolution is performed in the course of the model setup. The resolution and smoothness of the resulting fields of temperature, salinity and velocity depend mainly on the resolution of the model and, in principle, small-scale structures contained in the original station-data can be exploited by designing models with sufficiently high spatial resolution. Use of the original data as opposed to gridded data sets has the additional advantage that statistical information about the data like variability and covariance can be gathered in the averaging process and subsequently be used in the model calculations (for details see below). Error information is usually not provided with gridded data sets.

For the model, the hydrographic data mainly serve two purposes: Firstly, they are used to calculate dynamic height and geostrophic velocity profiles. The model flow-field is initialized with the calculated geostrophic velocities and the geostrophic velocity profiles provide vertical velocity shear "data" which are used to constrain the horizontal model flows during the model calculations (see below). Secondly, the hydrographic data are used to obtain average potential temperature and salinity values defined on the model grid. Ultimately, the model will try to match the model-simulated temperatures and salinities with the average box temperature and salinity values derived from the data. The fields of density gradients along the three cartesian coordinates x, y, and z (positive values pointing eastward, northward and upward), which define the orientation of isopycnals, and the Brunt-Väisälä frequency, which is a measure of vertical stability, are also derived from the hydrographic data. These parameters are needed for the implementation of the isopycnal mixing tensor in the model. In the following, the procedures for deriving the different input data of the model from the original station data are described and selected results relevant for model design and the discussion of model results are presented and discussed.

Mean Profiles of Dynamic Height

At each corner point (node) of the model grid (see section 3.1) a mean profile of dynamic height relative to the sea-surface is calculated. For this, stations from a rectangular region surrounding the node are selected and dynamic height is calculated at a set of 50 standard levels from the surface down to 6500 db for each of the selected stations:

$$\Delta D_i = \int_{p_r}^{p_i} \delta dp \tag{2.1}$$

In (2.1) p_i is level pressure, p_r is the reference pressure (here: $p_r = 0$) and δ is the specific volume anomaly. The region from which stations are selected is gradually enlarged until at least five valid stations are found. Then, at each standard level p_i the (distance-weighted) mean dynamic height $\overline{\Delta D_i}$ as well as its variance $\sigma^2_{D_i}$ and the covariances with the other standard depths $\sigma^2_{D_{i,j}}$ are calculated and stored. Quality of the individual dynamic height profiles is checked visually and stations with bad data or insufficient vertical sampling are rejected from the averaging process. The variance of dynamic heights (relative to 0 db) at the bottom of a node and the size of the region from which stations are selected, are used to derive a quality indicator q for the particular node, which, when large, indicates large variability of dynamic heights and/or sparseness of data. This quality indicator is used to define weight factors in the cost function of the model (see section 3.4).

Geostrophic Flows

Once all the profiles of mean dynamic height are calculated for all nodes of the model grid, geostrophic velocity profiles u^* are calculated for each pair of nodes (although zonal (u^*) and meridional (v^*) velocities are calculated at the different model interfaces only u^* is referred to in the following). For this step, the dynamic heights at the two nodes are first referenced to a conveniently chosen level p_r (here: $p_r = 2500$ db; constant for the whole model domain). For pairs of nodes shallower than p_r, the bottom pressure of the deepest of the two nodes is used as reference pressure. Geostrophic velocities (in [m s^{-1}]) at the standard levels p_i are obtained as

$$u_i^* = \frac{10}{fL}[\overline{\Delta D_{A_i}} - \overline{\Delta D_{B_i}}] \tag{2.2}$$

where $\overline{\Delta D_{A_i}}$ and $\overline{\Delta D_{B_i}}$ are the mean dynamic heights (in [dyn m]) at the two nodes A and B, L is the distance between the two nodes (in [m]) and f is the Coriolis parameter (in [s^{-1}]. Dynamic height covariances (derived from the hydrographic data) are then used to calculate the covariance matrix of the geostrophic velocities at the 50 standard levels. The geostrophic velocities are averaged over the depth intervals of the model layers and Ekman velocities calculated from the Trenberth *et al.* (1989) winds are added to the geostrophic velocities of the top two layers (0 to 140 m depth) to obtain initial model horizontal flows. As an example, Fig. 5 shows a profile of zonal geostrophic velocity u^* (referenced to 2500 db) in the subtropical north Atlantic. Note that the vertical extent of the velocity points u_i^* reflects the layer thicknesses in the model.

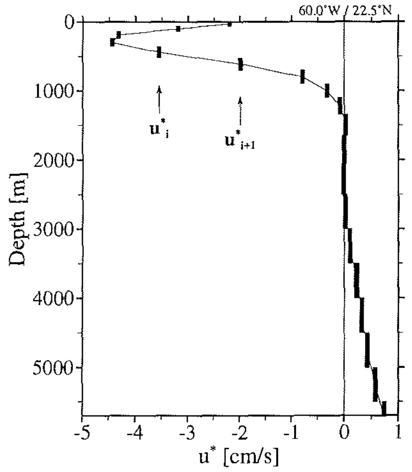

Fig. 5: Profile of zonal geostrophic velocity u^* relative to 2500 db in the subtropical north Atlantic. Solid bars are mean velocities of the model layers. The extend of the model layers is indicated by the length of the bars.

Fig. 6 shows geostrophic flows relative to 2500 db in 100 m depth in the Atlantic derived from the hydrographic stations shown in Fig. 3 with the method described above. Flow vectors represent vector-averaged nearby zonal and meridional velocities. Comparison with Fig. 1 shows that most of the major surface currents in the Atlantic (Antarctic Circumpolar Current, Benguela Current, South and North Equatorial Currents, Florida Current, Gulf Stream, North Atlantic Current, Canary Current) are reproduced by the geostrophic calculations, and the calculated flow field appears to be a good starting point for the actual model runs. Peak velocities in the strong currents are smaller than values obtained from direct current measurements which is attributable to spatial and temporal averaging resulting in relatively broad and slow flows (Olbers *et al.*, 1985). Close to the equator geostrophic velocities are sensitive to data errors and no clear circulation pattern evolves there. In this region the model flows are initially set to zero and are not coupled to the initial geostrophic estimates.

Geostrophy alone only allows determination of the vertical velocity shear $u^*_z = \partial u^* / \partial z$, and in Fig. 5 the velocity profile is arbitrarily fixed to zero at the reference level. Absolute velocities are obtained from the geostrophic flows by adding an unknown, constant velocity component (the reference velocity) to the profile. The notion that hydrographic data together with the principle of geostrophy only determine the shape of the velocity profile while the absolute values remain unknown is reflected in the model design. Model flows are initialized with the geostrophic flows, but in the course of the calculations, flow velocities are allowed to adjust in a way that largely preserves vertical velocity shear (as given by

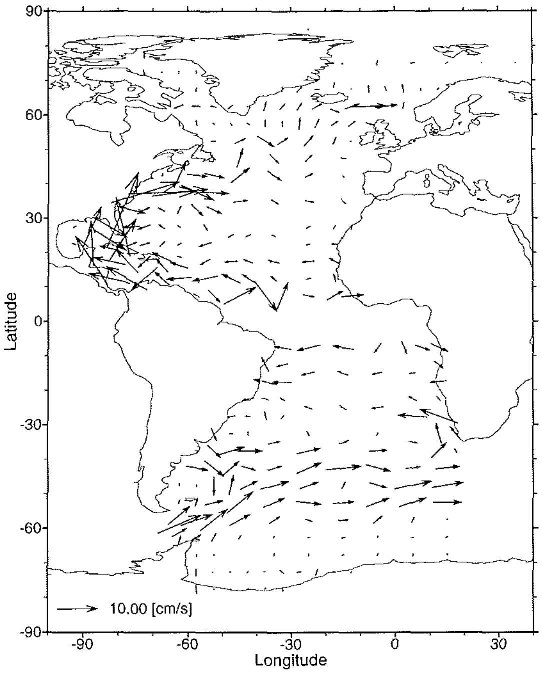

Fig. 6: Geostrophic flows relative to p_r = 2500 db in layer 2 (60 - 140 m). Arrows are vector averages of the east-west and north-south flows of individual boxes and centers of arrows are positioned at the box centers.

the geostrophic calculations) while accommodating constant velocity shifts (see sections 3.5 and 3.6).

Mean Property Distributions

For the control-volumes, or boxes, of the model (see section 3.1) mean potential temperatures θ_d and mean salinities s_d are calculated by averaging over all data points that lie in a given box. Data quality has been checked visually and outliers were rejected. The resulting three-dimensional distributions of θ_d and s_d are considered to be good representations of the mean oceanic distributions given the dense spatial station coverage (Fig. 3) and the large time interval for which data are available (Fig. 4). In the polar and subpolar regions, however, the θ_d and s_d distributions are biased towards the respective summer situations. As for the geostrophic flows, the extent to which small-scale structures of the real temperature and salinity fields are recovered in the averaged fields depends mainly on the resolution of the model grid, and, for instance, narrow boundary layers can, in principle, be adequately resolved by providing sufficient horizontal and vertical resolution.

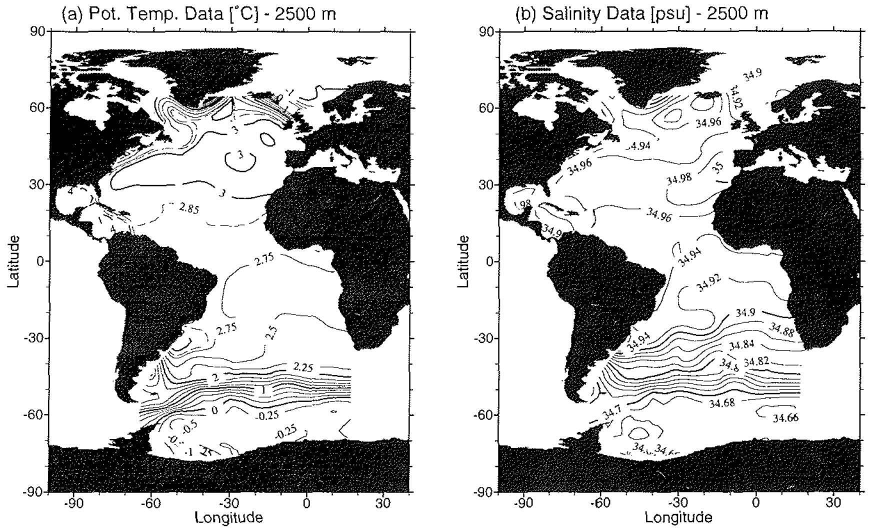

Fig. 7: Distributions of (a) averaged potential temperature and (b) averaged salinity in 2500 m depth in the Atlantic based on the original station-data shown in Fig 3.

As examples, Fig. 7 shows fields of averaged potential temperature and salinity in 2500 m depth obtained by averaging the original data over boxes extending typically 5 by 5 degrees in longitude and latitude and 500 m in depth and subsequent contouring. Potential temperature and salinity in the deep Atlantic are closely related and the distributions show the same main features. In the polar regions, both in the Weddell Sea and in the Nordic Seas deep water temperatures are below zero and salinities are relatively low. Towards the equator pronounced meridional property gradients are observed both in the north and south Atlantic which separate the polar waters from the warmer and more saline deep water in the central Atlantic. In the north, the position of the temperature and salinity fronts coincides with the overflow region (Denmark Strait and Iceland-Scotland ridge) which acts as a barrier separating the Nordic Seas from the central Atlantic. In the southern Atlantic the meridional property front follows the position of the Antarctic Circumpolar Current (ACC).

North Atlantic Deep Water (NADW) in 2500 m depth is warmer and more saline compared with deep water in the south Atlantic and apparently spreads southward along the western boundary. At the equator the southward spreading NADW seems to separate into two branches, one continuing southward along the South American coast and one turning eastward at the equator and turning southward along the South African coast. This branching of the NADW at the equator is also indicated in deep water oxygen and chlorofluoromethane distributions (Wüst, 1935; Weiss *et al.*, 1985). In section 5.2.4 the model-derived reference level velocities at 2500 db will be compared with the temperature and salinity fields given by Fig. 7, and the question is addressed whether the derived flows correspond to the structures found in the property fields.

Errors of the averaged θ_d values at this depth (obtained by error propagation using the data variance for the uncertainty of individual data points) in most regions are below 0.01 °C and are thus considerably smaller than the typical error of individual temperature measurements ($\sigma_\theta \approx 0.02$ °C). Probably due to the relatively large contribution of older data (Fig. 4c) errors of averaged temperatures are larger in the Southern Ocean (≈ 0.04 °C). The increased scatter of the data values could be caused by poorer quality of the old data or it might reflect long-term temperature changes of a few hundreds of a degree Celsius in the deep water of the south Atlantic over the last 70 years. Errors of the averaged salinity values are about 0.002 in the north Atlantic and lie between 0.003 and 0.01 in the south Atlantic. In both areas, these errors tend to be larger than the uncertainty of up-to-date individual salinity measurements ($\approx$0.002) and could be caused by the poor quality of some of the older salinity data especially in the south Atlantic where older data are most prominent (Fig. 4). It is important to note that the errors of the θ_d and s_d values are explicitly taken into account in the model by requiring that the model reproduce the observations only within the estimated error margins (see below).

Density Gradients

For the implementation of the isopycnal mixing tensor (needed to calculate diffusive property fluxes; see section 3.4) the components of the potential density gradient $\sigma_x = \partial\sigma/\partial x$, $\sigma_y = \partial\sigma/\partial y$, $\sigma_z = \partial\sigma/\partial z$ have to be known in the entire region of interest. The resulting density gradient $\nabla\sigma = [\sigma_x, \sigma_y, \sigma_z]^T$ is always perpendicular to surfaces of constant density (isopycnals) and thus locally defines their orientation. Because the components of $\nabla\sigma$ are differentials they are sensitive to errors in the hydrographic data and special care must be taken to identify and remove false data. In the present case, potential densities are calculated from the averaged, mean temperature and salinity values described above. Then, for each component of $\nabla\sigma$, its spatial distribution is inspected visually, outliers are removed and are replaced by weighted averages of nearby values.

As examples of results obtained with this labour-intensive but inevitable procedure the horizontal and vertical density gradients in 1000 m depth are shown in Fig. 8. Note that horizontal density gradients reflect the presence of (density) fronts which correspond to relatively strong geostrophic currents. Zonal density gradients σ_x can be associated with meridional flows, and meridional density gradients σ_y can be associated with zonal flows. This correspondence between ocean currents and density gradients is clearly reflected by the distributions of σ_x and σ_y in Fig. 8a and 8b. In general, σ_x in 1000 m depth is small in most parts of the Atlantic. Only east of Drake Passage, where the ACC turns northward, at the North American coast where the Gulf Stream flows northward and in the northeast Atlantic where the north Atlantic Current flows into the Norwegian Sea significant zonal density gradients are found. Similarly, the σ_y field (Fig. 8b) corresponds to the major zonal currents in the Atlantic at this depth: Antarctic Circumpolar Current near 50°S and the Gulf Stream east of 70°W.

The vertical density gradients σ_z in 1000 m depth (Fig. 8c) are maximal in the centers of the subtropical gyres near 30°N and 30°S where the thermocline is especially deep. In the equatorial Atlantic values are about half the maximal values and are nearly constant, and in the polar regions vertical stability is weak and vertical density gradients are very small. Overall, Fig. 8 demonstrates that with the given hydrographic data-base and rigorous quality control reliable fields of σ_x, σ_y, and σ_z can be obtained.

Brunt-Väisälä Frequency

In one of the numerical model runs described below, the diapycnal mixing coefficients are related to the vertical density stratification of the water column as expressed by the Brunt-Väisälä frequency. For this, the spatial distribution of the Brunt-Väisälä frequency

$$N = \sqrt{-\frac{g}{\rho_0}\frac{\Delta\rho}{\Delta z}} \tag{2.3}$$

has to be calculated in the whole model domain. In (2.3) g is the acceleration of gravity, ρ_0 is the mean density and $\Delta\rho$ is the potential density difference between a water parcel adiabatically displaced by a distance Δz from its equilibrium position and its (new) neighbourhood. At a given point in the ocean, profiles of Brunt-Väisälä frequencies are calculated for all hydrographic stations in a neighborhood of this point and then averaged to obtain a mean profile at that point. Again, data quality is checked visually and outliers are removed before averaging.

Fig. 9 shows the distribution of Brunt-Väisälä frequency obtained in this way along a meridional section through the Atlantic at 30°W. It is clearly seen that Brunt-Väisälä frequency and stability are maximal in the thermocline of the tropical Atlantic. Values decrease with depth and reach very small values in the deep water of the Weddell Sea, the Arctic Ocean and the eastern north Atlantic (between 10 and 35°N) where water mass properties are almost constant. Note the deepening of the isolines at the centers of the subtropical gyres and the relative maximum at about 4000 m depth between 30°S and the equator at the interface between the Antarctic Bottom Water (AABW) and the overlying NADW.

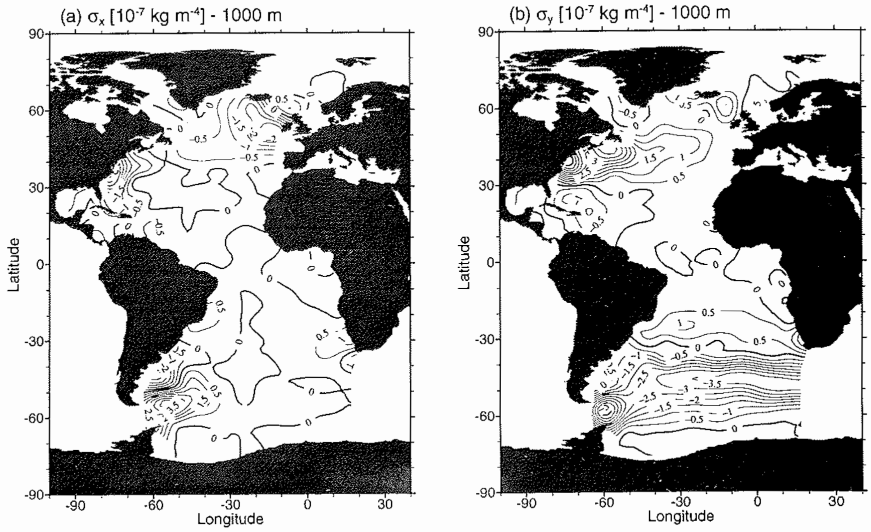

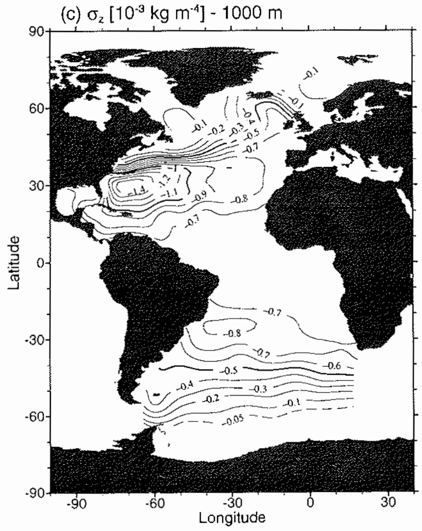

Fig 8: Distributions of horizontal and vertical potential density gradients in 1000 m depth in the Atlantic: (a) σ_x, (b) σ_y and (c) σ_z. Gradients are derived from the averaged temperature and salinity fields.

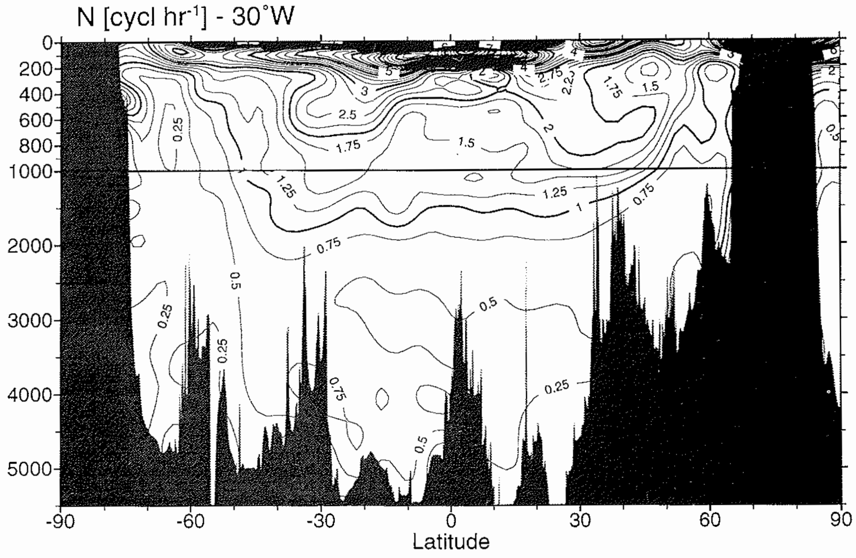

Fig. 9: Brunt-Väisälä frequency N along a meridional section at 30°W in the Atlantic. Values are based on averaged temperature and salinity data. Note the change in depth-scale at 1000 m.

Chapter 3

Model Setup and Strategy

As shown in section 2 large amounts of historical hydrographic data are available for the entire Atlantic. Probably with the exception of the polar regions, this data base seems to adequately represent the annually averaged, long-term distributions of temperature, salinity and geostrophic velocities. In the following section a new model approach is presented that makes use of the large sets of available hydrographic data. Goal of the model calculations is to determine the mean, large-scale ocean transports together with air-sea heat and fresh-water fluxes and coefficients of iso- and diapycnal mixing.

3.1 Model Grid and Geometry

The model covers the entire Atlantic (Fig. 10a) and has realistic topography based on the US Navy bathymetric data (5' by 5' resolution) which are averaged over the grid-dimensions. The model domain is subdivided on a rectangular grid with non-uniform resolution ranging from 2.5° to 10° horizontally. By allowing non-uniform horizontal resolution, smaller scale features like the Florida Current, the Gulf Stream, the Brazil Current and the Antarctic Circumpolar Current (ACC) in Drake Passage can be included and resolved reasonably well without the need to carry the relatively high resolution to more quiet and smooth regions like the eastern parts of the subtropical gyres. In this way the size of the model can be kept small enough to be tractable while supporting reasonably high spatial resolution in special regions of interest. In the vertical, the model domain is subdivided along constant depth horizons (Fig. 10b) into a maximum of 20 layers with vertical resolution varying between 60 m at the surface and 500 m in the deep ocean. Model velocities u, v and w are defined at the centers of the interfaces whereas model temperatures and salinities are defined at the box centers.

The choice of model domain and geometry outlined in Fig. 10a was guided by the objective to minimize the total length of open ocean boundaries. For the calculation of property distributions, boundary conditions have to be provided along open ocean boundaries, and especially for transient tracers which will be incorporated in future versions of the model, specification of these boundary conditions is problematic because of lack of data. In the

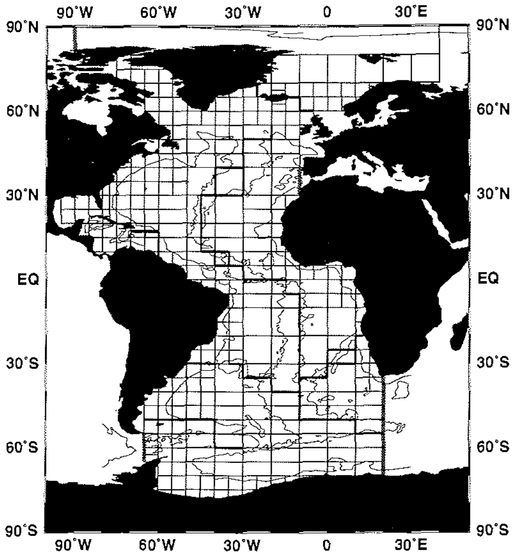

Fig. 10: Horizontal (Fig. 10a) and vertical (Fig. 10b) model grid. Solid lines in Fig. 10a indicate the model representation of major ridge-systems and gray-shaded bars indicate open ocean boundaries. Depth contour in Fig. 10a is the 4000 m depth isoline. In Fig. 10b the position of two nodes A and B is indicated. At the nodes mean dynamic height profiles are calculated which are then used to derive geostrophic velocities u.

model, there are four open ocean boundaries for the exchange with the Pacific, the Indian Ocean and the Mediterranean.

3.2 Parameters and Model Equations

Horizontal flows u and v defined at the centers of the box interfaces (Fig. 10b), air-sea heat fluxes Q, and two parameters p_{kh} and p_{kv} linked to the horizontal and vertical mixing coefficients form the set of independent model parameters:

$$\mathbf{p}^* = [..., u_i, ..., v_j, ...Q_k, ..., p_{kh}, p_{kv}]^T \tag{3.1}$$

These are the basic model parameters, they have to be initialized to start the model and they are modified in the variational procedure following initialization. Given a set of independent parameters $\mathbf{p}^*$, a set of additional, dependent parameters

$$\tilde{\mathbf{p}} = [w_1, ..., w_n, \theta_1, ..., \theta_n, s_1, ..., s_n]^T \tag{3.2}$$

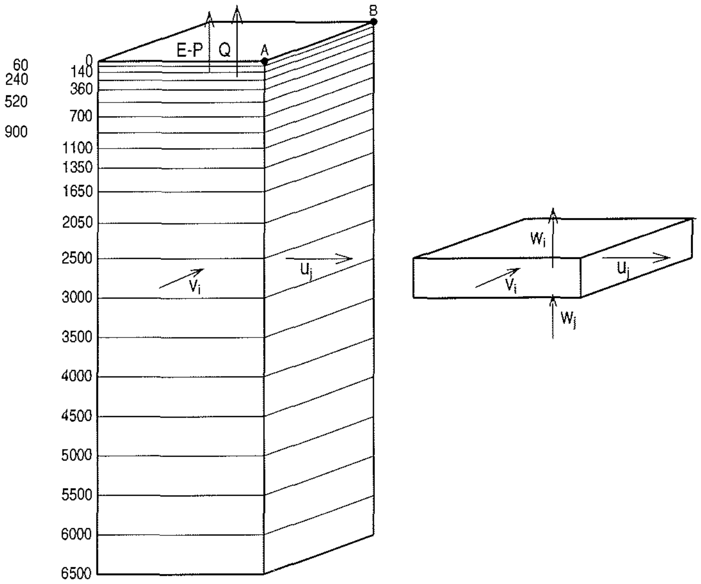

Fig. 10: Continued.

are uniquely determined by employing mass, heat and salt budget equations. In (3.2) n is the number of boxes, w are the vertical flows, θ are the model simulated potential temperatures and s are the simulated salinities.

The vertical flows w are calculated column-wise starting with the bottom box, and for each box the vertical flow through its top surface is set to compensate any net divergence resulting from the horizontal flows u and v and the vertical flow through the bottom surface of the box. Note that the vertical flows through the air-sea interfaces which represent the fresh water fluxes *E-P* due to evaporation minus precipitation and river-runoff is calculated together with and in the same way as the vertical flows in the ocean interior. Also note that calculation of the w as described above guarantees that model mass balances

$$\sum_i A_i u_i + \sum_j A_j v_j + \sum_k A_k w_k = 0 \qquad (3.3)$$

are satisfied exactly. In (3.3) summation is over all interfaces of the box, A is the area of an interface and has either positive or negative sign depending on whether a positive flow (eastward, northward or upward) enters or leaves the box.

The calculation of model potential temperatures is based on the steady-state heat balance equation including advective and diffusive transport and air-sea heat fluxes:

$$\begin{aligned}\sum_i A_i[u_i\theta_i^* - K_h\Delta\theta_i/L_i] \quad &+ \textstyle\sum_j A_j[v_j\theta_j^* - K_h\Delta\theta_j/L_j] \\ &+ \textstyle\sum_k A_k[w_k\theta_k^* - K_v\Delta\theta_k/L_k] \quad - Q = 0\end{aligned} \tag{3.4}$$

where the three terms represent zonal, meridional and vertical components of heat transport, summation again is over all interfaces of a box, A is the signed area of an interface, L is the distance between the box centers to both sides of an interface, K_h and K_v are iso- and diapycnal mixing coefficients, θ^* is the temperature transported by a flow, $\Delta\theta$ is the temperature difference between the two boxes and Q is the heat-flux across the air-sea interface and only appears in the heat budgets of surface boxes.

The salt budget equations used to calculate model salinities are similar to the heat budgets except that there is no salt transport through the air-sea interface (although there is a fresh water flux). Formulation of the steady-state budget equations for heat or salt, in both cases, yields a quadratic system of linear equations for the unknown model temperatures or salinities. The resulting linear systems are large (dimension n_b = number of boxes) but sparse because each box only exchanges with a small number of neighbors. An iterative method (Lanczos algorithm see Paige and Saunders, (1982)) that takes advantage of the sparsity of the coefficient matrix and only requires storage of the non-zero elements is used to solve for the model temperatures and salinities.

Two different numerical differencing schemes ("upwind" and "centered-in-space") have been implemented and model results for these two cases are presented and compared in section 5. For the upwind scheme the temperature θ^* or salinity s^* transported by a given horizontal or vertical flow (see (3.4)) is taken as the temperature (salinity) of the box in which the flow originates whereas for the centered-in-space scheme θ^* (s^*) is taken as the arithmetic mean of the temperatures (salinities) of the two boxes involved. At the open ocean boundaries, temperatures and salinities derived from the original station data (Fig. 3) are provided as boundary conditions. Formally, the boundary terms as well as the air-sea heat fluxes Q are transferred to the right-hand-side of (3.4) because these terms do not contain factors of unknown temperatures or salinities.

3.3 Clusters

In principle, the heat and salt budgets are formulated for the individual model boxes, resulting in the present case in large linear systems of dimension n_b=4375. For reasons of computational efficiency, it was decided to perform some of the model runs with heat and salt budgets defined on a coarser grid of n_c=1777 clusters which are obtained by combining two or more of the model boxes. The choice of clusters (Fig. 11) was guided by the overall structure of the temperature and salinity distributions in the Atlantic. The horizontal extent of the clusters was allowed to be large in directions of small property gradients (generally in zonal direction) whereas the original model resolution was preserved

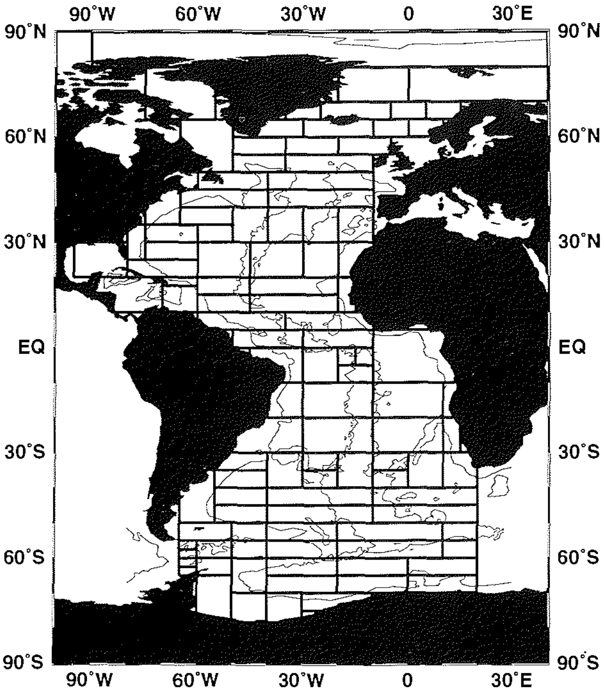

Fig. 11: Map showing the control volumes (clusters) used for some model temperature and salinity calculations. Depth contour is the 4000 m depth isoline.

in directions with large property gradients (meridionally). Note that the vertical model resolution was not altered by the introduction of clusters.

3.4 Mixing Tensor

The mixing coefficients K_h and K_v in the budget equations are linked to the model parameters p_{kh} and p_{kv}:

$$K_h = C_h(x, y, z)p_{kh}^2 \tag{3.5}$$

$$K_v = C_v(x, y, z)p_{kv}^2 \tag{3.6}$$

where C_h and C_v are spatially varying functions through which different mixing parameterizations can be implemented. Note that, although the mixing parameters p_{kh} and p_{kv} that are modified by the model can take on any real value, the mixing coefficients K_h and K_v are guaranteed to be positive by setting them proportional to the square of the respective mixing parameters. Two cases of different mixing parameterizations are examined below:

(1) a simple case with C_h and C_v constant in the entire model domain and (2) the case with C_v given by the inverse Brunt-Väisälä frequency:

$$K_v = a_0 N^{-1} \tag{3.7}$$

A parameterization of the form (3.7) was proposed by Gargett (1984) and Gargett and Holloway (1984) based on studies of internal wave breaking and observational evidence. Although still debated in the scientific community, (3.7) is used here for a first numerical experiment that goes beyond the assumption of constant K_v and follows the intuitive notion that vertical mixing is suppressed in regions of enhanced stability. The unknown factor a_0 corresponds to p_{kv}^2 in the present formalism and is determined in the course of the model optimization. It should be emphasized that (3.7) by no means represents the only possible parameterization of K_v. Other forms (e.g., Pacanowski and Philander, 1981; Sarmiento *et al.*, 1976) have been considered and can equally well be implemented in the model with unknown scaling factors determined by the model optimization.

In the heat budget equation (3.4) a diagonal mixing tensor

$$\mathbf{K} = \begin{bmatrix} K_h & 0 & 0 \\ 0 & K_h & 0 \\ 0 & 0 & K_v \end{bmatrix} \tag{3.8}$$

is implicitly assumed. Because K_h is much larger in the ocean than K_v, (3.8) states that strong mixing is occuring in the horizontal (cartesian coordinates x and y) whereas weak mixing takes place in the vertical (cartesian coordinate z). However, from potential energy considerations it seems more reasonable to choose the principal axis of the mixing tensor according to the orientation of isopycnal surfaces rather than using cartesian coordinates. Then, mixing is strong along isopycnal surfaces (new coordinates x' and y' which span the tangent plane of an isopycnal at a given point) and weak perpendicular to the isopycnal surface (diapycnal mixing in the direction z'). Given the orientation of an isopycnal surface by the local density gradient $\nabla\sigma$ (see section 2.2.4) the diagonal mixing tensor in the isopycnal coordinate system can be transformed into the original, cartesian coordinate system of the model (Redi, 1982):

$$\mathbf{K^I} = \frac{K_h}{\sigma_x^2 + \sigma_y^2 + \sigma_z^2} \begin{bmatrix} \sigma_z^2 + \sigma_y^2 + \epsilon\sigma_x^2 & (\epsilon - 1)\sigma_x\sigma_y & (\epsilon - 1)\sigma_x\sigma_z \\ (\epsilon - 1)\sigma_x\sigma_y & \sigma_z^2 + \sigma_x^2 + \epsilon\sigma_y^2 & (\epsilon - 1)\sigma_y\sigma_z \\ (\epsilon - 1)\sigma_x\sigma_z & (\epsilon - 1)\sigma_y\sigma_z & \sigma_x^2 + \sigma_y^2 + \epsilon\sigma_z^2 \end{bmatrix} \tag{3.9}$$

where $\mathbf{K^I}$ is the isopycnal mixing tensor expressed in cartesian coordinates, σ_x etc. are the components of the density gradient, K_h is the isopycnal mixing coefficient and $\epsilon = K_v/K_h$ is the ratio of diapycnal and isopycnal mixing coefficients.

Note that in the case of horizontal isopycnals, e.g., $\sigma_x = 0$ and $\sigma_y = 0$, (3.9) reduces to the simple, diagonal mixing tensor (3.8). In general, the flux of a property c by mixing is given by

$$\mathrm{j_c} = \mathbf{K^I}\nabla c \tag{3.10}$$

which for each component of $\mathbf{j_c} = [j_{c_x}, j_{c_y}, j_{c_z}]^T$ involves all three components of the property gradient

$$\nabla c = [\frac{\partial c}{\partial x}, \frac{\partial c}{\partial y}, \frac{\partial c}{\partial z}]^T \tag{3.11}$$

and leads to a more complicated form of heat and salt budgets compared with (3.4). Model runs have been performed for constant mixing coefficients K_h and K_v and cartesian mixing tensor (3.8) (standard run) and for the case K_h=const, $K_v \sim N^{-1}$ applying the isopycnal mixing tensor (3.9). Results for the different runs are presented and discussed in section 5.

3.5 Cost Function

Once the complete set of model parameters

$$\mathbf{p} = [\mathbf{p}^*, \tilde{\mathbf{p}}]^T \tag{3.12}$$

consisting of the independent parameters $\mathbf{p}^*$ and the dependent parameters $\tilde{\mathbf{p}}$ is calculated (section 3.2), the current model state is evaluated by calculating the value of the cost function. The cost function F accumulates penalties for all undesired features of the model solution. A large value of the cost functions indicates that the current model solution is far from the desired state, and goal of the subsequent model calculations is to minimize the value of F, thereby forcing the model in the wanted direction.

The characteristics of the desired model solution are determined by the form of the cost function and definition of the cost function is an important step during model setup. All terms contributing to the cost function of the present study are discussed in the following. A summary of these terms and their mathematical form is given in Table 1.

(1) Outside the equatorial band (10°S - 10°N) the vertical shear $u_z = \partial u/\partial z$ and $v_z = \partial v/\partial z$ of the horizontal flows is required to be close to the vertical shear $u_z^* = \partial u^*/\partial z$ and $v_z^* = \partial v^*/\partial z$ of the initial geostrophic flows. Adding a constant offset velocity (the reference velocity u_r and v_r) to a vertical profile of u or v does not change the vertical shear and can be accomplished without being penalized. Changing the shape of the vertical profile, however, will lead to a contribution to the cost function. The weight factors α_p of this term change spatially depending on statistical information (quality indicator derived from data variability and availability) obtained while calculating mean dynamic height profiles (see section 2.2.1). In order to keep the size of term 1 small, the vertical shear of model flows is required to be close to the initial vertical shear of the geostrophic profiles in areas with good station coverage and small variability of the dynamic heights (α_p small) whereas larger deviations of the vertical shear are tolerated in regions with few data and/or large variability (α_p large). Term 1 links the horizontal flows of the model to the dynamical principle of geostrophy. Whereas the integral budgets equations of mass, heat and salt (model

Table 1: Summary of terms contributing to the cost function. Each term appears in the cost function with its individual weight factor (for explanations see text).

No.	Meaning	Mathematical Form
1	Deviations from initial geostrophic shear u_z^* and v_z^*	$\sum_i[(u_{z_i} - u^*_{z_i})/(\alpha_p\sigma_{u^*_z})]^4 +$ $\sum_i[(v_{z_i} - v^*_{z_i})/(\alpha_p\sigma_{v^*_z})]^4$
2	Deviations from fresh-water flux data $E\text{-}P_d$	$\sum_i[(E\text{-}P_i - E\text{-}P_{di})/\sigma_{E\text{-}P}]^2$
3	Horizontal smoothness of fresh-water fluxes $E\text{-}P$	$\sum_i[(E\text{-}P_e - 2E\text{-}P_i + E\text{-}P_w)^2 +$ $(E\text{-}P_n - 2E\text{-}P_i + E\text{-}P_s)^2]$
4	Deviations from linear vorticity balance	$\sum[\beta v + f\partial w/\partial z]^2$
5	Horizontal smoothness of vertical velocities w_i	$\sum_i[(w_e - 2w_i + w_w)^2 +$ $(w_n - 2w_i + w_s)^2]$
6	Horizontal smoothness of reference velocities u_r	$\sum_i[(u_{re} - 2u_{ri} + u_{rw})^2 +$ $(u_{rn} - 2u_{ri} + u_{rs})^2]$
7	Horizontal (zonal) smoothness of horizontal velocities in equatorial band	$\sum_i(u_e - 2u_i + u_w)^2$
8	Deviations from *a priori* transports T	$\sum[(\sum_i u_i - T)/\sigma_T]^2$
9	Deviations from air-sea heat-flux data Q_d	$\sum_i[(Q_i - Q_{di})/\sigma_Q]^2$
10	Horizontal smoothness of air-sea heat-fluxes Q	$\sum_i[(Q_e - 2Q_i + Q_w)^2 +$ $(Q_n - 2Q_i + Q_s)^2]$
11	Deviations from temperature data θ_d	$\sum[(\theta_m - \theta_d)/\sigma_{\theta_d}]^2$
12	Deviations from salinity data s_d	$\sum[(s_m - s_d)/\sigma_{s_d}]^2$
13	Penalize systematic temperature deviations	$\sum[\sum_{NH}(\theta_m - \theta_d)/\sigma_{\theta_d}]^2$
14	Penalize systematic salinity deviations	$\sum[\sum_{NH}(s_m - s_d)/\sigma_{s_d}]^2$
15	Deviations from mixing coefficient "data"	$[(p_{kh} - P_{kh})/\sigma_{P_{kh}}]^2; [(p_{kv} - P_{kv})/\sigma_{P_{kv}}]^2$

equations) are required to be satisfied exactly by the model, the geostrophic constraint is only enforced in an approximate way. Note that this term is raised to the fourth power in order to suppress occasional, large shear deviations.

(2) The fresh-water fluxes *E-P* through the air-sea interface are required to be close ($\sigma_{E\text{-}P_d} = \pm 50\%$) to independent estimates of *E-P* data. The *E-P* data used in this study are derived from (Hellermann, 1973) and were obtained from NCAR (Boulder).

(3) The spatial distribution of fresh-water fluxes *E-P* is required to be smooth. Smoothness in this term, as well as in other smoothness requirements following below, is enforced by penalizing the second derivatives of the fields in west-east and south-north directions.

(4) As additional dynamical principle the model enforces the linear vorticity balance by linking the vertical derivative of vertical velocities $\partial w/\partial z$ with the meridional velocities v. This constraint is not applied in the equatorial region (10°S - 10°N) and in the bottom-most and top-most three layers of each box-column (see Fig. 10b).

(5) For each layer in the model the horizontal distribution of w is required to be smooth.

(6) The horizontal distribution of reference velocities u_r and v_r introduced by the model is required to be smooth.

(7) In the equatorial band (10°S - 10°N) the field of horizontal velocities is required to be smooth in west-east direction while no restriction is applied for the south-north direction. This term represents the only constraint on horizontal flows near the equator (except for an *a priori* transport constraint discussed in item 8). In the given form, item 7 "tolerates" the observed mostly zonally oriented equatorial currents and counter-currents.

(8) *A priori* knowledge about the strength of ocean currents is incorporated into the model by requiring that the corresponding model transports (sum over the interfaces contributing to the flow) are close to the *a priori* values. The present model contains a number of such transport constraints: (a) upper-layer (0-520 m) meridional transport across equator close to 20 Sv, (b) Drake-Passage throughflow close to 124 Sv (Nowlin *et al.*, 1977), (c) Gulf-Stream at Cape Cod close to 120 Sv (Fofonoff, 1981), (d) Florida Current close to 30 Sv (Leaman *et al.*, 1989; Niiler and Richardson, 1973), (e) Brazil Current at 30°S close to 20 Sv (Peterson and Stramma, 1991), (f) Iceland-Scotland shallow inflow into Norwegian Basin close to 15 Sv , (g) Bering Straits inflow into Arctic Ocean close to 1 Sv (Coachman and Aagaard, 1974) and (h) lower layer (520-1500 m) westward flow from Mediterranean boundary close to 3 Sv (outflow through Strait of Gibraltar plus entrainment; note that model boundary is about 5°west of Gibraltar).

(9) Model air-sea heat fluxes Q are required to be close ($\sigma_{Q_d} = \pm 50\%$) to the independent heat-flux estimates Q_d of Oberhuber (1988).

(10) The horizontal distribution of Q is required to be smooth. In the southern part of the south Atlantic for which Oberhuber does not provide data, this is the only constraint on Q.

(11 and 12) The simulated temperatures and salinities are required to be close to the observed temperature and salinity fields (box-wise comparison).

(13 and 14) In addition to box-wise comparisons represented by terms 11 and 12 above, this term penalizes systematic deviations (under- or overestimations of model temperatures or salinities) within an entire neighborhood of a box by first calculating the mean, normalized deviation within the neighborhood and then adding the square of this value to the cost function.

(15) The parameters p_{kh} and p_{kv} are required to be close to *a priori* values.

Terms 1 and 11 through 14 are considered the most important terms in the cost function. Minimizing these contributions is synonymous with seeking a model solution that reproduces the measured temperature and salinity distributions as closely as possible, while leaving the shape of the geostrophic velocity profiles largely unchanged. The purpose of the additional terms is to add more physics (linear vorticity balance), to incorporate *a priori* knowledge on transport rates, air-sea fluxes and mixing coefficients and to enforce spatial smoothness of the resulting fields.

3.6 Adjoint Model

One of the primary features of the model is its ability to automatically produce new model states that are "better" than previous ones with respect to the criteria specified in the cost function F. For a given (imperfect) model state $\mathbf{p}$ this involves the determination of a direction in model space (the vector space spanned by the independent parameters) along which a smaller value of the cost function can be found. In the case of constrained minimization (minimize F while satisfying a set of model equations $E_i = 0$) such a descent direction is efficiently calculated by the method of Lagrange multipliers (Thacker, 1988b; Hestenes, 1975).

With the model equations (here: mass, heat and salt budgets for all boxes respectively clusters; total number: $n_e = n_b + 2 * n_c$) written in the form

$$E_i = 0 \qquad\qquad i = 1, ..., n_e \tag{3.13}$$

and the cost function F defined above, the Lagrangian L is given by

$$L = F + \sum_{i=1}^{n_e} \lambda_i E_i \tag{3.14}$$

where λ_i are n_e yet unknown Lagrange multipliers. Note that $L = L(\mathbf{p}, \lambda)$ is a function of model parameters $\mathbf{p}$ and the Lagrange multipliers λ. The minimum of F is a stationary point of L and all partial derivatives of L with respect to model parameters p_i and Lagrange multipliers λ_j (calculated as though the p_i^*, $\tilde{p}_i$ and λ_j were independent) vanish:

$$\frac{\partial L}{\partial \lambda_j} = E_j = 0 \tag{3.15}$$

$$\frac{\partial L}{\partial \tilde{p}_i} = \frac{\partial F}{\partial \tilde{p}_i} + \sum_{j=1}^{n_e} \lambda_j \frac{\partial E_j}{\partial \tilde{p}_i} = 0 \tag{3.16}$$

$$\frac{\partial L}{\partial p_i^*} = \frac{\partial F}{\partial p_i^*} + \sum_{j=1}^{n_e} \lambda_j \frac{\partial E_j}{\partial p_i^*} = 0 \tag{3.17}$$

Differentiation with respect to the Lagrange multipliers (3.15) recovers the model equations (3.13), and differentiation with respect to the dependent and independent model parameters $\tilde{p}_i$ and p_i^* yields the *adjoint equations* (3.16) and (3.17). Seeking the minimum of F is equivalent to finding a model solution that satisfies (3.15), (3.16) and (3.17). In practice the minimum of F is approached by an iterative procedure. The Lagrange multipliers λ are calculated by solving (3.16) with $\partial L/\partial \tilde{p}_i$ set to zero. Introducing the λ into (3.17) then yields the gradient of F given by $\nabla F = \partial L/\partial p_i^*$. The gradient of F is then passed to a descent algorithm (here: limited memory, quasi-Newton conjugate gradient algorithm; Gilbert and Lemaréchal, 1989) to obtain a new, improved model state $\mathbf{p}_{new}$ with a smaller value of the cost function F.

(3.16) represents a system of $n_e = n_b + 2 * n_c$ linear equations in the $n_e = n_b + 2 * n_c$ unknown Lagrange multipliers λ_j. This linear system can be separated into three smaller linear systems because model temperatures θ do not appear in the mass- and salt budgets and model salinities s do not appear in the mass- and heat budgets. The vector of Lagrange multipliers λ can then be calculated by solving two systems of dimension n_c and one system of dimension n_b successively. As in the case of solving for the unknown model temperatures and salinities (section 3.2) the Lanczos algorithm is used to calculate the Lagrange multipliers.

Overall, the model calculations proceed according to the following steps:

(S0) Initialize the independent parameters $\mathbf{p}^*$ by setting the horizontal flows u and v to the geostrophic flows u^* and v^* and the air-sea heat fluxes Q as well as the mixing parameters p_{kh} and p_{kv} to values found in the literature (see below).

(S1) Calculate dependent parameters $\tilde{\mathbf{p}}$ using steady-state mass, heat and salt budgets.

(S2) Calculate the value of the cost function F.

(S3) Calculate the gradient of F, $\nabla F = \partial L/\partial p^*$ by solving the adjoint equations (3.16) and (3.17).

(S4) Use ∇F in a descent algorithm to obtain a new, improved set of independent model parameters $\mathbf{p}^*{}_{new}$.

(S5) Back to (1) unless a stopping criteria (i.e., indicating that the value of the cost function is sufficiently close to its minimum) is met.

Step S1 is usually referred to as running the "forward model". Its most computationally intensive part is calculation of the model temperature and salinity fields, which involves solving two large (but sparse) sets of linear equations. The calculation of the w is comparatively cheap. For each run of the forward model, one run of the adjoint model (step S3) is needed to complete an iteration. The computational cost running the adjoint model is comparable with running the forward model.

It should be pointed out that the main purpose of the adjoint model is to calculate the directional gradient of the cost function, e.g. a direction in parameter-space along which the cost function F decreases. In principle, this gradient could also be calculated by perturbing a single independent parameter $p_i^{*'} = p_i^* + \delta p_i^*$ at a time and recalculating the value of the cost function $F_i^{'}$ for this perturbed parameter set thereby obtaining the i-th component of the gradient $\partial F / \partial p_i^* = (F_i^{'} - F)/\delta p_i^*$. Repeating this procedure for all independent parameters then yields the full gradient vector. Regarding the large number of model parameters (here: n_p=7757), however, this procedure is impractical because it would involve n_p runs of the forward model in order to calculate the gradient of F once. The great advantage of the adjoint formalism is, that it allows the calculation of the gradient much more efficiently, namely with only one additional forward run instead of n_p. From an oceanographer's point of view the role of the adjoint formalism, as a means of efficiently calculating the gradient, is mainly technical. The oceanographically important features and the overall characteristics of the model and the solution which is obtained, however, are determined by the design of the forward model and, in the present case, by the definition of the cost function.

Chapter 4

Initialization of Model Parameters

In order to start the model iterative loop defined by (S1) to (S5), the independent model parameters p^* (horizontal flows u and v, the air-sea heat-fluxes Q and the mixing parameters p_{kh} and p_{kv}) have to be initialized. This is done by setting the horizontal flows to the geostrophic flows relative to $p_r = 2500$ db which are calculated from the hydrographic data (see section 2.2.2 and Fig. 6), the air-sea heat fluxes to values derived from Oberhuber's (1988) annual mean, net downward heat flux data and the mixing parameters to values found in the literature ($K_h = 500$ m^2 s^{-1} and $K_v = 0.5 \cdot 10^{-4}$ m^2 s^{-1}; Olbers *et al.*, 1985; Olbers and Wenzel, 1989). South of 40°S, where Oberhuber does not provide annual mean net heat flux data, the initial model heat fluxes are set to zero. Because of this lack of independent heat flux estimates, model heat fluxes in these regions can vary freely and are not tied to "data".

4.1 Pre-optimization

While reproducing the major current systems in the Atlantic (Fig. 6), the geostrophic flows used to initialize the model exhibit severe deficiencies. The vertical flows w associated with the u and v (see section 3.2 for method of calculating w) are orders of magnitudes too large and change chaotically (often reversing direction) from one model column to the next. Resulting air-sea fresh water fluxes *E-P* are of the same magnitude as interior w and are thus incompatible with *E-P* estimates. This behavior is not unexpected, because in the model the vertical flows are given as residuals of (large) horizontal flows and even small errors and inconsistencies in the horizontal flow field lead to large uncertainties of the associated vertical flows.

The unrealistic vertical flows and especially the huge *E-P* fluxes of the initial flow field can not be expected to produce realistic temperature or salinity simulations. For instance, the large magnitudes of the w and the frequent upwelling/downwelling reversals result in vertically relatively homogenous property fields and prevent the establishment of a thermocline in the tropical and subtropical regions. *E-P* fluxes affect surface salinities and the huge initial *E-P* values (positive and negative) lead to a salinity distribution at the ocean surface consisting of very large and very small values that shows no resemblance with observations. Therefore a *pre-optimization* of the model flows was run before including temperature and salinity simulations in the model. Two different procedures have been employed. They are described and evaluated in the following.

4.2 Iterative Procedure

The first pre-optimization method represents a specialization of the general model approach with a simplified cost function F. Terms 9 through 15 of F (see Table 1) are removed by setting their weight factors to zero, no temperature or salinity simulations are performed, the set of dependent parameters is restricted to the vertical flows w and mass budgets represent the only model equations. Terms 2 and 3 in the cost function are now the most important terms because these penalize the initially chaotic behavior of the *E-P* fluxes and act to enforce consistency with *E-P* data and lead to a smooth distribution of model *E-P*. Term 5 guarantees that the w fields at every level in the interior are smooth and term 8 enforces *a priori* transport estimates to be satisfied. Elimination of temperature and salinity simulations reduces the computational cost per iteration considerably and pre-optimization proved to be an efficient way of producing a nearly geostrophic flow field with relatively smooth and small vertical flows in the interior and realistic fresh-water fluxes at the air-sea interface.

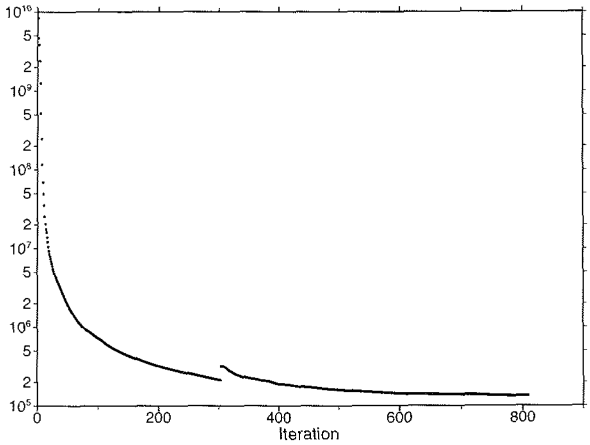

Fig. 12: Cost function versus iteration number for the pre-optimization. The discontinuity near iteration 300 is due to a change of weight factors.

The decrease of the value of the cost function F during pre-optimization is shown in Fig. 12. The large value at the beginning is mainly due to the terms related with the

E-P fluxes and the interior vertical flows (terms 2, 3 and 5) while the deviations from geostrophic shear (term 1) are zero at the beginning. After about 800 iterations the value of the cost function has been reduced by almost five orders of magnitude and the minimum of F is reached. As an example of results from these calculations the vertical velocities in 1650 m depth after pre-optimization are shown in Fig. 13. Values are small and smooth almost everywhere in the Atlantic except in the subpolar north Atlantic where prevailing downwelling indicates deep water formation in the Greenland Basin and downward motion south of the overflows. Obviously, the unrealistically large values and chaotic behavior of the w in the initial flow field are removed. Also, air-sea fresh water fluxes after pre-optimization (not shown) are compatible with independent *E-P* estimates.

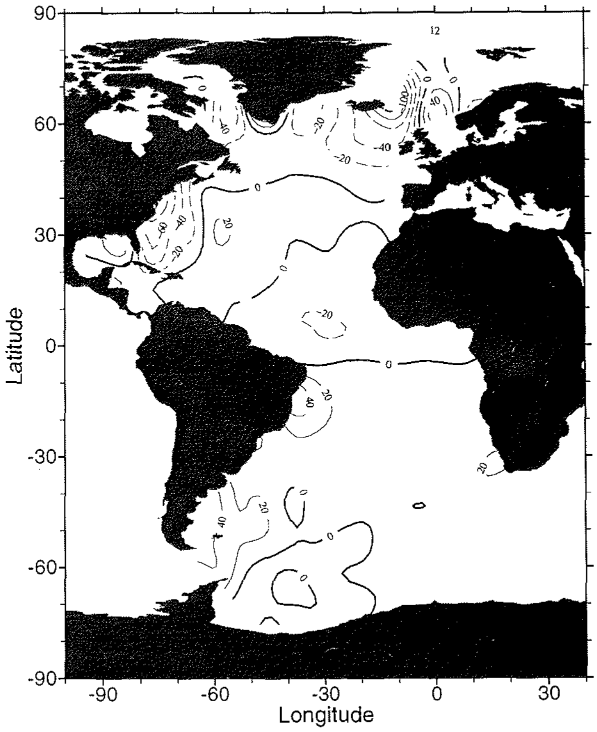

Fig. 13: Vertical velocities w [10^{-7} m s^{-1}] in 1650 m depth after pre-optimization (iterative procedure).

The adjusted flow velocities in 100 m depth after pre-optimization and the differences to the initial geostrophic flows (see Fig. 6) are shown in Fig. 14. As can be seen in Fig. 14b,

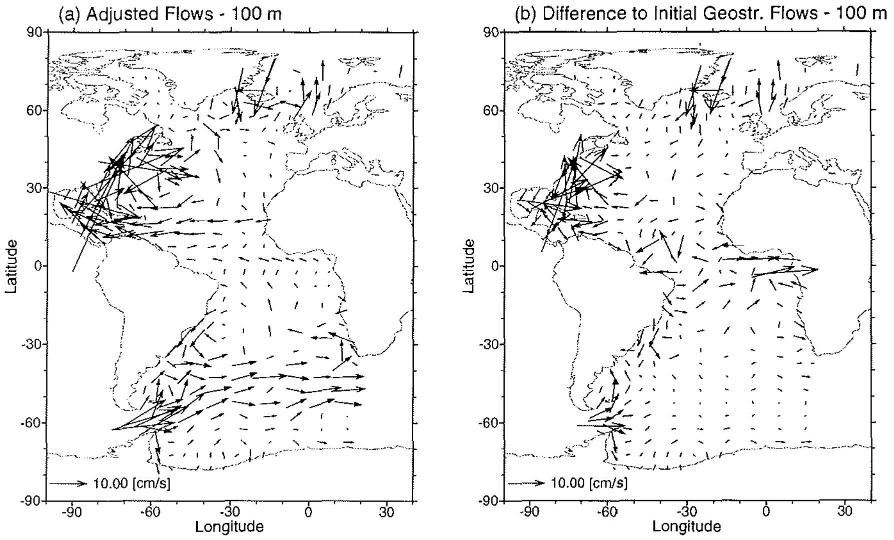

Fig. 14: (a) Horizontal flows in layer 2 (60 - 140 m) after pre-optimization (iterative procedure) and (b) difference to initial geostrophic flows from Fig. 6.

velocity modifications are considerable, especially near boundaries and in the equatorial region. The large velocity increases in Drake Passage, along the Brazilian coast, in Florida Straits and in the Gulf Stream area are mostly due to *a priori* transport constraints that in all cases enforce more intense flows compared with the transport rates provided by the geostrophic calculations. Changes in the equatorial region are mainly caused by term 7 in the cost function, which penalizes abrupt changes of horizontal flows in the zonal but not the meridional direction, and, as Fig. 14a nicely shows, produces zonally coherent current bands not unlike the ones observed in the real ocean.

In summary, it can be stated that the iterative pre-optimization procedure is successful in applying modifications to the initial horizontal velocities yielding a perfectly mass conserving flow field which accommodates *a priori* transport constraints, zonal current bands near the equator and, most importantly, smooth fields of w in the ocean interior and realistic *E-P* fluxes at the air-sea interface. However, despite the simplifications of the cost function and the omission of temperature and salinity simulations during pre-optimization, the computational effort is still high and alternative procedures with less computational load are desirable. One such approach is described below.

4.3 "Independent Layer" Approach

Whereas in the iterative procedure described above the goal was to obtain smooth horizontal distributions of w at all model levels and realistic *E-P* fluxes at the air-sea interface, here the unrealistic w's and *E-P* fluxes of the initial geostrophic flow field are removed by enforcing zero vertical velocities w at all levels and zero *E-P* fluxes at the ocean surface thereby ignoring any vertical flows between the layers of the model and treating them as being independent. Later, when temperature and salinity simulations are included, the model is expected to establish non-zero w's consistent with the θ and salinity distributions.

Corrections δu and δv to the initial geostrophic velocities u^* and v^* are calculated on a layer by layer basis. For each box within a given layer, mass conservation is enforced considering horizontal flows only

$$\sum_i A_i u'_i + \sum_j A_j v'_j = 0 \tag{4.1}$$

where A_i and A_j are signed interface areas and $u' = u^* + \delta u$ and $v' = v^* + \delta v$ are the adjusted velocities. Formulation of these (2-D) mass budgets for all boxes of a model layer results in a set of linear equations

$$\mathbf{B}\mathbf{x} = \mathbf{\Gamma} \tag{4.2}$$

where the coefficient matrix $\mathbf{B}$ contains the A_i and A_j, $\mathbf{x} = [\delta u,\ \delta v]^T$ is the vector of yet unknown velocity corrections and the Γ_i are mass divergences of the boxes given by the initial geostrophic flows. Because there are more box-interfaces than boxes, the linear systems (4.2) are underdetermined and have an infinite number of solutions. Here, the goal is to determine the minimum norm ($\|\mathbf{x}\|$ minimal) solution, e.g. the smallest possible corrections required to make the initial geostrophic velocity field mass conserving in two dimensions.

Minimum norm solutions to (4.2) can be obtained by singular-value decomposition (Wunsch and Minster, 1982; Menke, 1984). In the present case, the solution $\mathbf{x}$ is obtained iteratively involving a procedure similar to the full model iterations (see section 3.6). A cost function f is defined composed of the squared norms of the residuals to (4.2) and of the solution vector

$$f = (\mathbf{B}\mathbf{x} - \mathbf{\Gamma})^T(\mathbf{B}\mathbf{x} - \mathbf{\Gamma}) + \alpha\mathbf{x}^T\mathbf{x} \tag{4.3}$$

with $\alpha \approx 10^{-5}$ being a small constant.

The calculations are started with $\mathbf{x} \equiv 0$, the gradient of the cost function f with respect to the unknowns

$$\nabla f = 2(\mathbf{B}^T\mathbf{B}\mathbf{x} - \mathbf{B}^T\mathbf{\Gamma} + \alpha\mathbf{x}) \tag{4.4}$$

is calculated and this gradient is passed to a descent algorithm that produces an improved solution vector. Then, the gradient (4.4) is calculated for the improved solution and an even better solution vector is obtained. The iterative procedure is similar to the overall model strategy outlined in section 3.6, except that solving (4.2) corresponds to an unconstrained minimization problem (no model equations present) and no Lagrange multipliers or adjoints are involved. In general, the requirements of small residuals and of a small solution vector cannot be satisfied simultaneously and the factor α in the cost function f can be used to control the relative size of these two terms. Here it was chosen so that the remaining residuals in the 2-D mass budgets correspond to small vertical velocities w and E-P fluxes of the order of $0.5 \cdot 10^{-7}$ m s^{-1}.

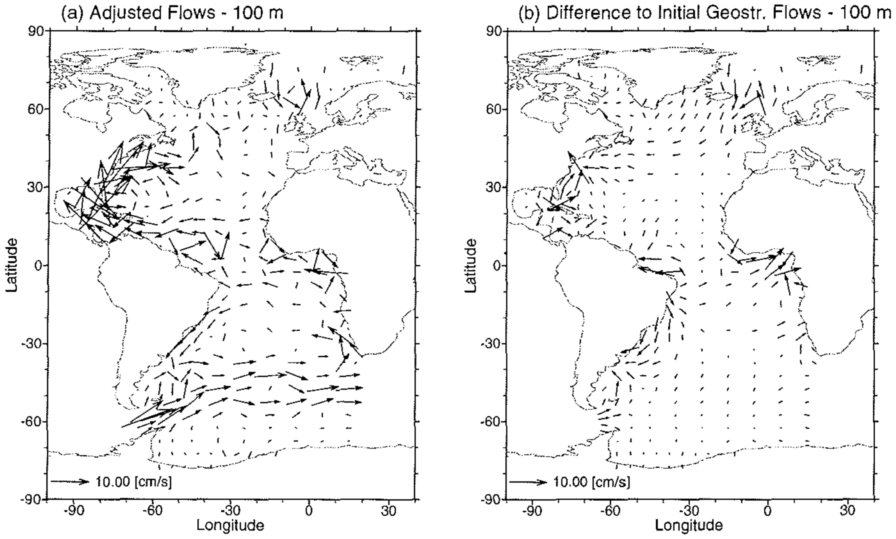

Fig. 15: (a) Horizontal flows in layer 2 (60 - 140 m) after pre-optimization (independent layer approach) and (b) difference to initial geostrophic flows from Fig. 6.

Fig. 15 shows the resulting velocity field in 100 m depth and the difference to the initial geostrophic flows obtained with this method. The overall magnitude of velocity modifications (Fig. 15b) is smaller compared with the modifications introduced by the iterative procedure described in section 4.2 (Fig. 14b). Differences between the two methods are most pronounced in areas where *a priori* transport constraints are active in the iterative procedure (Drake Passage, Florida Straits, Gulf Stream area) and in the equatorial region, where term 7 of the cost function (see Table 1) leads to zonal current bands that do not develop when the "independent layer" approach is used.

Besides these differences there is a great deal of similarity in the results of both methods. Fig. 15b shows, that although there are no transport constraints active in the "independent layer" approach, nevertheless transports along the Brazilian coast and through Drake Passage and Florida Straits are increased considerably obviously in order to allow mass conserving closure of gyres and along-stream coherence of major currents. The spatial pattern of velocity increases (Fig. 15b) suggests that the geostrophic calculations underes-

Table 2: Comparison and assessment of pre-optimization procedures.

	Iterative Procedure		"Independent Layer"
+	*E-P* fluxes close to independent estimates	+	*E-P* close to zero
+	Fields of w smooth	+	w close to zero
+	Vertical velocity shear close to geostrophic shear	−	No vertical coherence of velocity modifications
+	*A priori* flux constraints active	−	No *a priori* flux constraints included
+	Smoothness constraint (7) in equatorial region	−	No smoothness constraint in equatorial region
−−	Computationally expensive	++	Computationally very cheap

timate the strength of strong currents especially in narrow straits and passages as compared with open ocean areas, where the same currents are usually much broader and slower. In the case of the Gulf Stream system obviously the geostrophic calculations miss a large part of the Florida Current transport probably due to too coarse resolution . Its strength is increased after adjustment, but, obviously in order to keep overall modifications small (minimum $\|\mathbf{x}\|$), this velocity increase is insufficient in magnitude and the speed of the Gulf Stream east of Cape Hatteras has to be reduced because of continuity. In the South Atlantic the Brazil Current that is missing in the initial geostrophic fields, is present after adjustment even when no *a priori* transport constraints are applied (Fig. 15b). It is obvious that the Brazil Current is required as the link between the westward flowing South Equatorial Current and the eastward flowing South Atlantic Current near 40°S.

Both pre-optimization methods successfully remove the unrealistically large magnitudes and the chaotic structure of the initial w and *E-P* fields. The iterative procedure (section 4.2) is the more sophisticated of the two methods, because, in addition to controlling the w and *E-P* fields, other constraints are applied, and the final flow field exhibits desirable features that are not obtained with the "independent layer" approach (Table 2): (a) *a priori* transport constraints are satisfied in Drake Passage, Florida Straits, etc.; (b) zonally coherent current bands in the equatorial region appear; (c) the shear of the geostrophic velocity profiles is largely preserved and (d) w's and *E-P* fluxes are not required to be zero but can accommodate realistic features like deep water formation in the Nordic Seas and can reproduce the overall pattern of air-sea fresh-water fluxes.

However, achieving these advantages requires a considerable amount of computations and one can argue that a cheap method like the "independent layer" approach produces a circulation pattern that is realistic enough to start the full model (including temperature and salinity simulations) with it. Both possibilities have been applied. The Atlantic model, results of which are presented in the next section, has been started with a pre-optimized flow field using the iterative procedure, whereas the Gulf Stream model in section 6 was run with pre-optimized velocities obtained with the "independent layer" approach.

Chapter 5

Model Calculations and Results

5.1 Overview of Numerical Experiments

The full model, including simulations of temperature and salinity, was started using horizontal flows from the iterative pre-optimization procedure (section 4.2), annual mean, net air-sea heat fluxes from Oberhuber (1988) and first-guess values for the mixing coefficients (K_h = 500 m^2 s^{-1} and K_v = 0.5 $\cdot 10^{-4}$ m^2 s^{-1}; Olbers *et al.*, 1985; Olbers and Wenzel, 1989). As outlined in section 3.6, the model proceeds in an iterative way (steps S1 to S5) where each iteration involves one forward model run (calculation of the dependent parameters w, model temperatures θ and model salinities s), the evaluation of the current model state through calculation of the cost function F, one run of the adjoint model for the calculation of the gradient of F and the calculation of a new, improved set of horizontal flows, air-sea heat fluxes and mixing coefficients. Once started, this iterative loop continues until a stopping criteria indicating a sufficient decrease of the value of F and of the norm of the gradient vector is met and the optimal solution is returned.

Several numerical experiments have been run to study the effect of different differencing schemes, different mixing parameterizations and different representations of the mixing tensor on the solution. Table 3 gives a summary of these numerical experiments. The first experiment (UPW) is with the upwind differencing scheme for the heat and salt budgets (see section 3.2), constant mixing coefficients K_h and K_v in the entire model domain, a

Table 3: Summary of numerical experiments run with the Atlantic model.

Name	Scheme	Clusters	Mixing Param.	Mixing Tensor	Remarks
UPW	upwind	1777	K_h const.; K_v const.	cartesian	Standard case.
CS	centered	1777	K_h const.; K_v const.	cartesian	Centered-in-space differencing scheme.
CS-N	centered	1777	K_h const.; $K_v \sim N^{-1}$	isopycnal	Diapycnal mixing linked to stability.
CS-H	centered	1777	K_h const.; K_v const.	cartesian	Larger meridional heat transport.

mixing tensor that is diagonal in cartesian coordinates and a reduced horizontal resolution for the heat and salt simulations (1777 clusters, see Fig. 11). Results of this run are presented in detail below, and the solutions of the other experiments are later discussed in the context of this standard case. The CS experiment is similar to the UPW case except that the centered-in-space differencing scheme is used instead of the upwind scheme. In contrast to the upwind scheme, the centered-in-space differencing scheme is second order in space and avoids the large artificial mixing of the upwind scheme for steady problems (Roach, 1982). It is also used in all other model runs. Experiment CS-N has spatially varying diapycnal mixing coefficients linked to the inverse Brunt-Väisälä frequency N^{-1} (see section 3.4 and Fig. 9) and a mixing tensor given by (3.9) which is diagonal in isopycnal coordinates. This run is used to estimate the empirical constant a_0 in the parameterization $K_v = a_0 N^{-1}$. Finally, for experiment CS-H constant mixing coefficients and the simple mixing tensor (3.8) are chosen as for CS, but now additional constraints on the meridional heat transport are added to the cost function in order to enforce a stronger meridional overturning cell in the model solution. Weight factors of the different terms in the cost function F and the *a priori* volume transport constraints are identical for all model runs.

It should be emphasized that, despite terms 1 and 11 to 14 in the cost function (see Table 1), it is not clear from the outset whether the overall model goal of closely reproducing the measured distributions of temperature and salinity (expressed by terms 11 to 14) while preserving the vertical velocity shear from geostrophic calculations (term 1) can actually be met by a steady, coarse resolution model. The extent to which these objectives are ultimately satisfied is an important model result and has to be determined from the final optimal model solution. The presentation and discussion of model results therefore starts with a comparison of model temperature and salinity distributions with the observed fields followed by an analysis of the modifications of the geostrophic velocity shear necessary to achieve realistic property fields. Then (after verification of the most important model goals) the model circulation as well as integrated mass and heat transports, air-sea heat and fresh-water fluxes and mixing coefficients are presented and discussed. The contour plots of various fields shown below are obtained using an objective analysis algorithm with variable scale-lengths (Schlitzer, 1993) to produce gridded fields from the original, irregularly spaced data points and subsequent contouring.

5.2 Calculations with the Upwind Differencing Scheme (UPW)

Fig. 16 shows the decrease of the cost function versus iteration number for the UPW experiment. Discontinuities are due to model alterations and developments in the course of the run (e.g., the addition of term 2 in the cost function after about 50 iterations) and to adjustments of the weight factors in the cost function which were performed whenever it appeared that one or more terms of F remained unacceptably large. After a total of 2009 iterations the minimum of F had been found and the calculations terminated. Compared

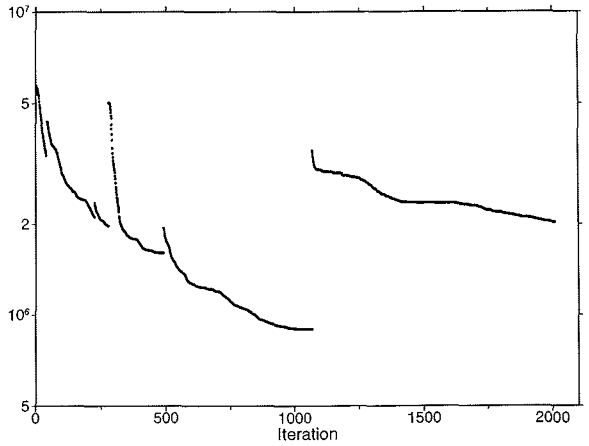

Fig. 16: Cost function versus iteration number for experiment UPW. Discontinuities are due to model alterations and adjustments of weight factors.

with the large decrease of the cost function during pre-optimization of about five orders of magnitude (Fig. 12), the overall decrease of F after inclusion of temperature and salinity simulations is relatively small and amounts to about one order of magnitude (discontinuities taken into account). This suggests that the flow field produced by the pre-optimization procedure which is used as starting point for the full model is already close to the final model solution. It will be seen below that the general pattern of horizontal flows is largely left unchanged, but that significant differences between pre-optimization and full model solutions are observed for integrated mass, heat and salt transports and also in the fields of vertical velocities w.

Model Temperatures and Salinities

Fig. 17 shows the distribution of potential temperature in 190 m depth obtained from the original station data (Fig. 17a) together with the model predicted temperatures in layer 3 (140 - 240 m depth; Fig. 17b). Main features in the data are the temperature maxima in the west Atlantic at about 20°S and 20°N reflecting the deepening of the isopycnals towards the centers of the subtropical gyres, significantly lower temperatures in the eastern tropical and subtropical Atlantic, and a tongue of this colder water apparently spreading north-westward across the equator. Poleward from the subtropical gyres there are strong meridional temperature gradients in both hemispheres, and temperatures in subpolar and polar region are relatively homogeneous and close to freezing.

The model simulated temperatures in layer 3 (Fig. 17b) closely resemble the measured field. The overall temperature range at this depth (ca. -1 to 20°C) and the main features in

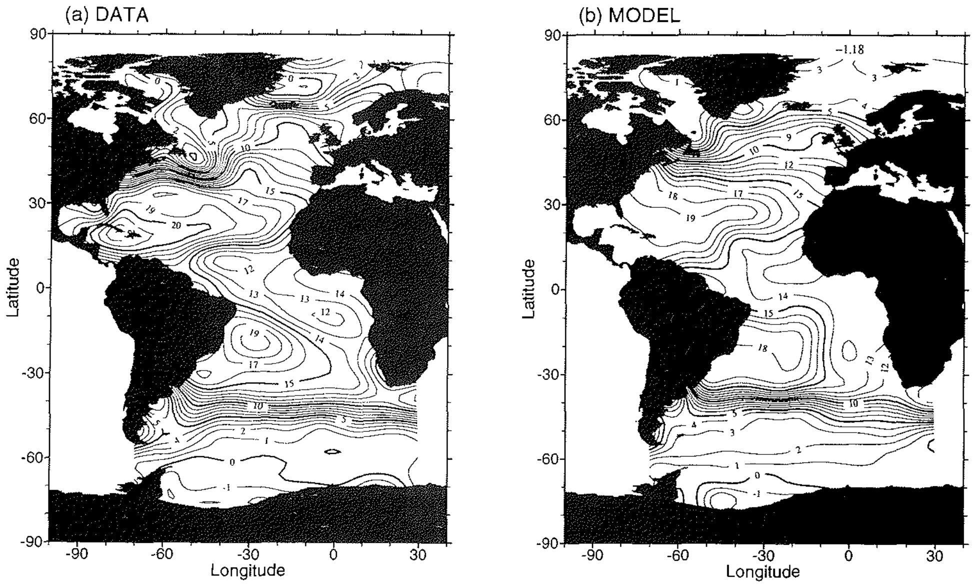

Fig. 17: Potential temperatures [°C] in layer 3 (140 - 240 m) for data (Fig. 17a) and UPW model solution (Fig. 17b).

the data are correctly reproduced by the model. As in the data, temperature maxima are found at about 20°S and 20°N in the western Atlantic, and maximal temperatures (19°C) are only slightly smaller than the observed values. In the eastern tropical and subtropical Atlantic temperatures are much lower (about 13°C) and (as observed in the data) a tongue of this colder water reaches into the western north Atlantic. In the south Atlantic the transition between subtropical and circumpolar waters is in very good agreement with the data, and the mean position of the 10°C isotherm in the model is found only about 150 km further north as in the data. Also, in the Weddell Sea (especially in its eastern portion) model temperatures are in very good agreement with the data. In the north Atlantic the overall structure in the temperature field is also correctly reproduced (compare positions of the 15, 10 and 5°C isotherms), however, it is this region where deviations between data and model appear to most pronounced. Critical regions are the Greenland and Norwegian seas and the Labrador Sea with Baffin Bay where the model temperature distributions are too homogenous compared with the data.

Temperature and salinity fields in about 200 m depth share many common features as can be seen by comparing Fig. 17 with the salinity distributions in model layer 3 shown in Fig. 18. The centers of the subtropical gyres in the west Atlantic are marked by pronounced salinity maxima, whereas the eastern parts of the tropical and subtropical Atlantic and

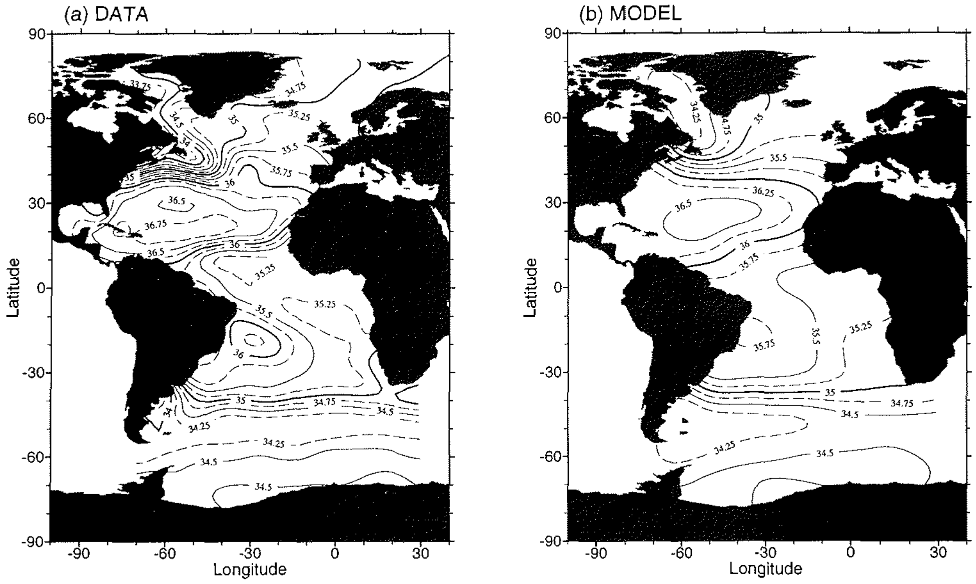

Fig. 18: Salinity [psu] in layer 3 (140 - 240 m) for data (Fig. 18a) and UPW model solution (Fig. 18b).

the polar and subpolar regions are much fresher. The transition zones generally coincide with the regions of large temperature gradients in Fig. 17. Like for temperature, the model salinity distribution (Fig. 18b) is in good agreement with the data. Again, the overall salinity range at about 200 m depth in the Atlantic (ca. 34.2 to 36.7 psu) is correctly reproduced, there are salinity maxima in the western Atlantic near 20°S and 20°N and fresher waters in the eastern tropical and subtropical Atlantic, the Southern Ocean south of about 40°S and in the north Atlantic and Arctic Ocean. The subtropical salinity maxima are somewhat weaker compared with the data and (as for temperature) the salinity distributions in the Labrador Sea and the Greenland/Norwegian seas appear to be too uniform.

Figures 19 and 20 show meridional sections of potential temperature (Figs. 19a and 19b) and salinity (Figs. 20a and 20b) along 30°W for the data and the model simulations. In the entire depth range, agreement between model simulations and data is good, both for temperature and salinity. Note that features like the deepening of the isolines near 30°S and 30°N (the northern one substantially deeper than the southern one), the presence of Mediterranean Water in about 1200 m depth at 30°N, the northward spreading of relatively fresh Antarctic Intermediate Water (AAIW) (about 800 m depth) and Antarctic Bottom Water (AABW) at the bottom and the southward spreading of higher saline North Atlantic

(a) DATA

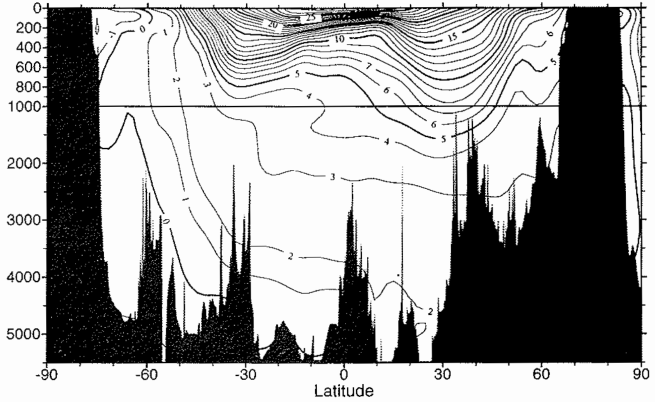

(b) MODEL

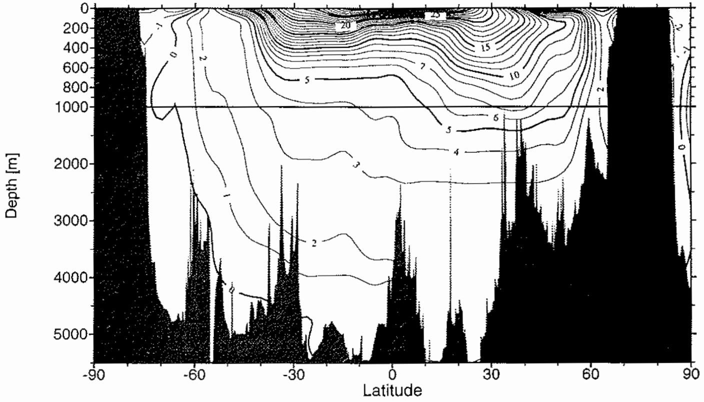

Fig. 19: Meridional section of potential temperatures [°C] along 30°W for data (Fig. 19a) and UPW model solution (Fig. 19b). Note the change in depth-scale at 1000 m.

Deep Water (NADW) are all reflected in the model temperature and salinity distributions.

In summary, despite small, systematic deviations found especially in the polar and subpolar north Atlantic, the overall agreement between model temperatures and salinities and observations is satisfactory. This is remarkable considering the relatively coarse spatial resolution of the model, the simplified representation of mixing in this first numerical experiment and the fact that in this steady model seasonal or interannual variability like winter convection processes are not included.

Modification of the Vertical Velocity Shear

At each (horizontal) velocity grid-point of the model the contribution of the entire velocity profile to term 1 of the cost function, e.g. the deviation from the "shape" of the initial geostrophic profile, is calculated, and the logarithm of this quantity is shown in Fig. 21. Values are between 0.1 and 50 almost everywhere in the model domain indicating that modifications of the vertical velocity shear are small and acceptable in a statistical sense. Larger values (greater than 100) are found only in the Gulf Stream region or in areas of the subpolar north and south Atlantic that are either poorly covered by hydrographic station data (see Fig. 3) or for which the available data are mainly representative for the respective summer seasons (Fig. 4). Note that in the equatorial area the model shear is unconstrained and not tied to initial estimates.

As examples, profiles of horizontal model velocities (solid bars with stars) at five selected positions in the Atlantic are shown in Fig. 22 together with the initial geostrophic profiles (solid bars). At all locations except for point (b) in the Gulf Stream the most noticeable difference between initial and final profiles are constant velocity shifts with only minor, additional modifications to the shape of the profiles. The magnitudes of the observed velocity offsets represent the previously unknown reference velocities u_r and are shown in the next section. Modifications of the shapes of the geostrophic velocity profiles are allowed in the model as a way of dealing with faulty or non-representative hydrographic data, however, term 1 in the cost function was included to keep such modifications small and to retain as much information as possible from the initial geostrophic calculations. The actual magnitude of changes to the shape of the velocity profiles for the final, optimal model solution (Fig. 22) are considered to be small and compatible with geostrophy, considering errors, variability and degree of representativeness of the available hydrographic data.

At profile (b), obviously, the *a priori* transport constraints of increasing the Gulf Stream transport (to 120 Sv from only 60 Sv in the initial geostrophic field) and yet avoiding eastward flow in the NADW layers which could lead to unrealistic deep temperature and salinity fields can only be satisfied by increasing the eastward flow in the upper layers while leaving the deep velocities largely unchanged. In the light of newer transport estimates of the Gulf Stream at Cape Hatteras and at 55°W (Leaman *et al.*, 1989; Richardson, 1985) a value of 120 Sv in the upper 1000 m used here as *a priori* constraint appears to be on the higher end of presently accepted values. Using smaller *a priori* values instead will relax the need in the model to excessively increase the shallow eastward flow at profile b.

Overall, it can be stated that the approach of incorporating the information of geostrophic

(a) DATA

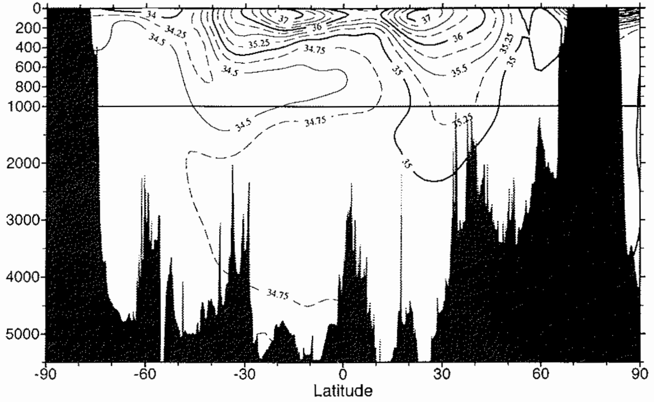

(b) MODEL

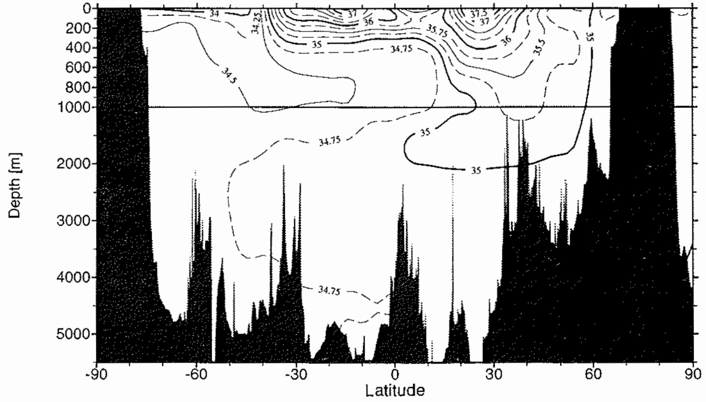

Fig. 20: Meridional section of salinity [psu] along 30°W for data (Fig. 20a) and UPW model solution (Fig. 20b). Note the change in depth-scale at 1000 m.

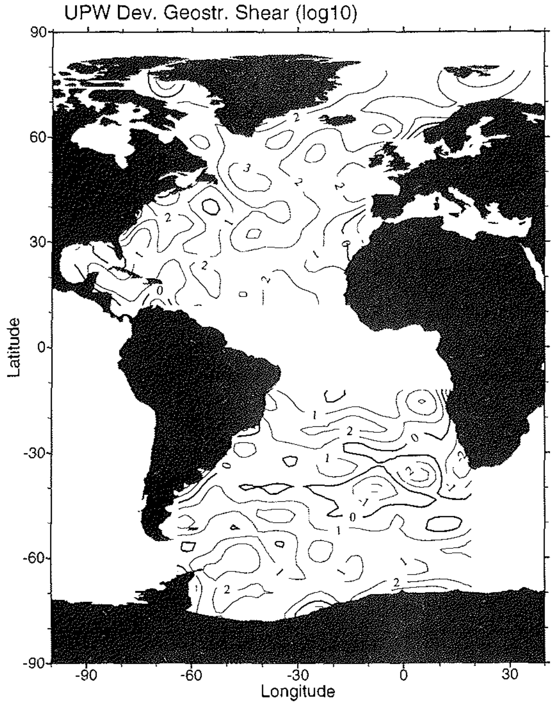

Fig. 21: Logarithm of vertical shear modification of entire velocity profiles for the UPW experiment. Note that in the equatorial area model velocity shear is unconstrained.

velocity calculations in the model using term 1 of the cost function is successful. The specific form of term 1 allows constant velocity offsets corresponding to the unknown reference velocities of geostrophic calculations without penalty. Modifications of the shear which are plausible because of errors, non-synopticity and partially poor coverage of the hydrographic data are accommodated for, but by penalizing these modifications the shape of the model profiles can be kept close to the geostrophic profiles. As a basic result of the UPW calculations it can be stated that the temperature and salinity distributions of the Atlantic can be closely reproduced with a steady flow field that is consistent with geostrophy.

Reference Velocities

The velocity offsets between final model solution and geostrophic profiles represent the reference velocities u_r left unknown by the geostrophic calculations. The field of these reference velocities is shown in Fig. 23. Consistent with common oceanographic belief,

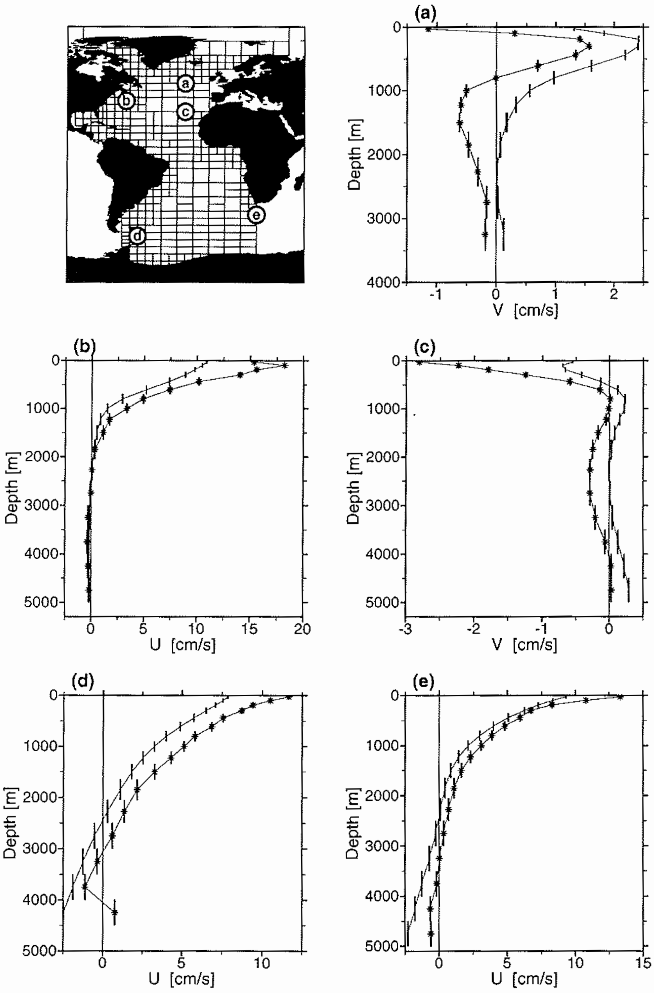

Fig. 22: Profiles of horizontal velocities at five locations (a-e) in the Atlantic. Solid bars are initial, geostrophic velocities relative to 2500 m depth and solid bars with stars are for the UPW model flows.

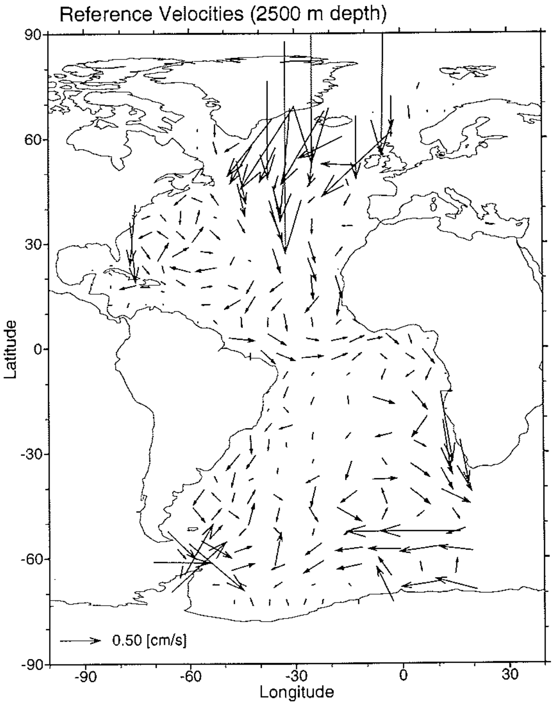

Fig. 23: Model velocities in 2500 m depth (reference velocities u_r) for the UPW experiment.

the flows at the reference depth (2500 m) which is within the NADW layer are to the south. Largest southward velocities are observed south of the overflow regions (about 60°N) and near Labrador Sea, the major source regions for NADW (Warren, 1981). At about 50°N the southward flow branches into a component flowing southwestward as a boundary current along the American coast (velocities between 0.2 and $1.7 \cdot 10^{-2}$ m s^{-1}) and into a component that continues southward in the central and eastern parts of the north Atlantic. In the model solution, this central component dominates.

North of the equator there is a large westward component of the flow, and most of the southward transport of NADW at this depth is guided to the western equatorial Atlantic. At the equator the flow separates again, one component flowing eastward along the equator and then turning southward at the African coast and the other component continuing southward along the Brazilian coast down to about 50°S, where the NADW is incorporated into the eastward flowing circumpolar waters. Most of the southward transport of NADW in the south Atlantic appears to be concentrated in the western boundary current and in the flow along the African coast. Eastward flows of about $1 \cdot 10^{-2}$ m s^{-1} are found in 2500 m depth in Drake Passage which are in accordance with direct current meter measurements (Nowlin *et al.*, 1977) indicating mean eastward velocities of about 1 to $2 \cdot 10^{-2}$ m s^{-1} at this depth.

The general pattern of model-derived velocities in 2500 m depth shown in Fig. 23 is supported by the distributions of temperature and salinity at this depth (Fig. 7). In the north Atlantic the southward flow of NADW along the American coast is hinted in the temperature and salinity fields as tongues of relatively cold and fresh water, but also the southward flow in the central and eastern part seems to be indicated in the property fields by a south-eastward directed deflection of the 34.96 salinity isoline at about 40°N, by the southward turning tongue of high salinity in the northeast Atlantic and by the increased southward extent of the 2.85 temperature isoline near 15°N in the east Atlantic. Southward flows of NADW in the western boundary current as well as in the central and eastern Atlantic are also seen in a map of deep flow velocities (2000 m depth) of Defant (1941; reproduced as Fig. 3.9 in Reid (1981)). Chlorofluoromethane data (Weiss *et al.*, 1985), however, indicate that, at least for the Upper North Atlantic Deep Water (about 1700 m depth), most of the southward transport occurs within the western boundary current suggesting that the model probably underestimates the strength of the deep western boundary current relative to the southward flow in the central north Atlantic. A possible explanation for this apparent underestimation of narrow boundary currents (see also the discussion on Florida and Brazil currents above) is the relatively large grid-size of the present model excluding the resolution of boundary current and its inner recirculation. Results from an application of the present model approach in the Gulf Stream area using a finer horizontal grid (2° in longitude by 1° in latitude) are presented in section 6 and reveal a strong, coherent deep western boundary current with higher flow velocities as in Fig. 23 and the northeastward recirculation in the interior.

The branching of the NADW in the equatorial west Atlantic into an eastward and southward component is clearly reflected in the temperature and salinity distributions (Fig. 7) where relatively warm and saline waters are found along the equator and southward

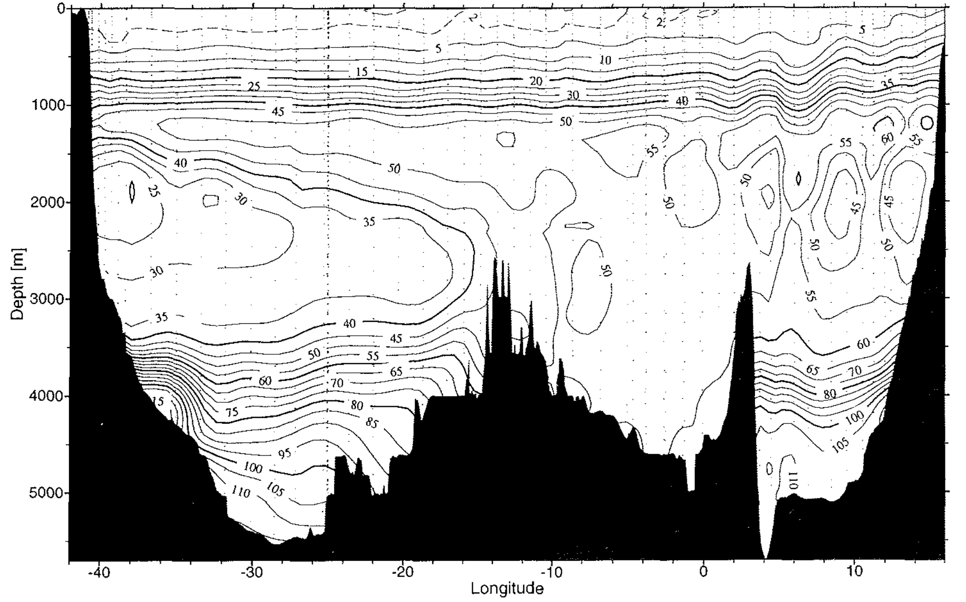

Fig. 24: Silicate [μmol kg^{-1}] along a zonal section at about 28°S in the south Atlantic based on data (small dots) from the South Atlantic Ventilation Experiment (SAVE, Lgs. 3 and 4).

along the Brazilian coast. Deep waters in the central sub-tropical south Atlantic are comparatively colder and fresher. Branching of the NADW flow at the equator has been shown to occur in numerical models (Kawase, 1987) and is also indicated in oxygen (Wüst, 1935) and chlorofluoromethane distributions (Weiss *et al.*, 1985) in this area.

The southward transport of NADW in the south Atlantic is illustrated by the silicate section in Fig. 24 that is based on data from the South Atlantic Ventilation Experiment (SAVE legs 3 and 4) and runs from about 24°S at the Brazilian coast to 30°S at the African coast. Silicate is well suited for the analysis of deep flows in the south Atlantic because of a large concentration difference between NADW and waters of Antarctic origin. In Fig. 24, NADW is easily identified by silicate minima found between 1700 and 3300 m depth at the western end of the section and at about 2000 m depth (multiple minima) at the eastern end. The silicate minimum at the Brazilian coast (21 μmol kg^{-1} in about 2000 m depth) is more pronounced compared with the minima in the east suggesting that the major component of southward flowing NADW is along the South American coast. The weaker silicate minima at the African coast are seen to represent the NADW that flows eastward along the equator and turns southward along the African coast as observed

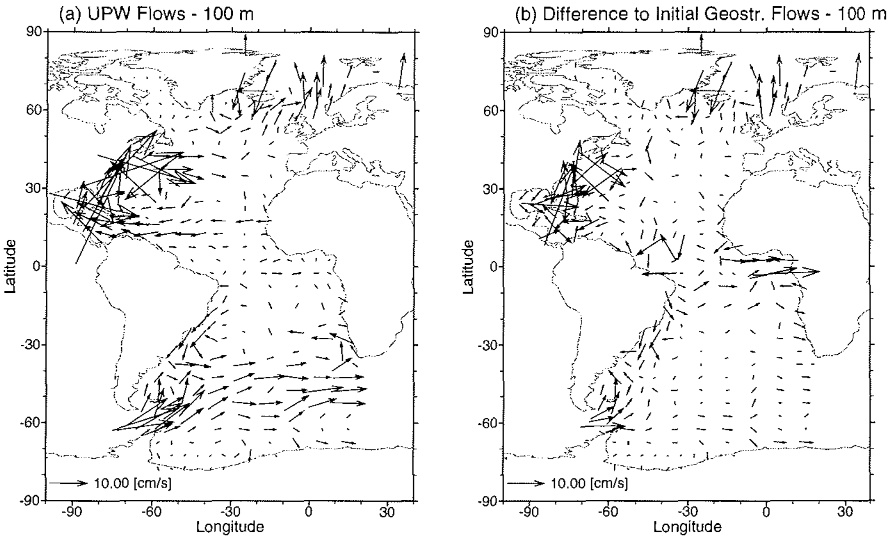

Fig. 25: Model velocities in layer 2 (60 - 140 m) (Fig. 25a) and velocity differences to the initial geostrophic velocities (Fig. 25b) for the UPW experiment.

in the UPW solution (Fig. 23). Although the strengths of the silicate minima can not directly be converted into strength of the respective flows, because of silicate respiration in the eastern tropical Atlantic (van Bennekom and Berger, 1984), it nevertheless appears that the western boundary branch of the southward flowing NADW dominates over the southward flow in the east Atlantic. This is not correctly reproduced in the model solution, again probably because of insufficient spatial resolution leading to an underestimation of the western boundary current. Additional support for the existence of the southward flow of NADW along the South-African coast comes from Defant's (1941) map of deep flows (see above) and from the southward turning of the temperature and salinity isolines in Fig. 7 in this region.

Horizontal Circulation

Horizontal model flows of the UPW solution in layer 2 (60 - 140 m) are shown in Fig. 25a together with the velocity differences to the initial geostrophic field (Fig. 25b). The dominant feature in the near-surface model circulation of the south Atlantic is the Antarctic Circumpolar Current (ACC) with peak velocities of about 20 $\cdot 10^{-2}$ m s^{-1} in Drake Passage. East of Drake Passage the ACC shifts northward (the Malvinas (Falkland) Current is clearly visible), widens and mean ACC velocities decrease to about 10 $\cdot 10^{-2}$ m s^{-1} in the open south Atlantic. Along the Brazilian coast a relative broad Brazil Current is flowing southward which meets circumpolar waters in the Brazil-Malvinas confluence zone at about 40°S. At this latitude the Brazil Current turns eastward and forms the South Atlantic Current which itself turns northward at the southern tip of south Africa feeding the Benguela Current. The Benguela Current flows northeastward into the subtropical south Atlantic and supplies the waters for the Brazil Current. Overall this circulation pattern of the model agrees well with flow charts of Peterson and Stramma (1991) and Reid (1989). Details of the circulation like the individual current bands of the ACC and the separation between ACC and the South Atlantic Current are not reproduced by the model because of limited horizontal resolution.

In the equatorial region, where geostrophy can not be used to constrain the model flows, velocities are small and, due to term 7 in the cost function, mostly zonally oriented. At the surface (not shown) there is a band-like structure resembling south- and northequatorial currents with an indication of a countercurrent in between, and in layer 2 (Fig. 25a) the consistent eastward flows just south of the equator might be a weak indication of the equatorial undercurrent. In the region between 10°S and 10°N "external guidance" of the model flows is weakest because geostrophy and linear vorticity balance are not applied there. Obviously, the smoothness constraints (term 7 in cost function) tend to produce flows that are weak compared with direct measurements (Richardson and Walsh, 1986). It is the equatorial region where model flows deviate most from the real ocean circulation, indicating the importance of the geostrophic calculations in other regions of the model where realistic flows are obtained.

The model circulation in the north Atlantic consists of a North Equatorial Current part of which flows through the Caribbean with the other part forming the Antilles Current. Both combine in the Florida Current that flows northward with maximal velocities of $40 \cdot 10^{-2}$ m s^{-1} and continues northeastward in the Gulf Stream (20 to $30 \cdot 10^{-2}$ m s^{-1}). Most of the Gulf Stream transport is locally recirculated, the rest feeding the North Atlantic Current and the Canary Current. The North Atlantic Current enters the Norwegian Sea providing warm and salty water to the polar ocean. As for the south Atlantic, the overall model circulation in the north Atlantic agrees well with present day knowledge, but again, due to limited spatial resolution, the model does not reveal the full complexity and small-scale structure of the circulation which, for instance, is obtained when closely spaced, synoptic hydrographic observations are analysed. Comparison of the UPW flows with the pre-optimized velocity field (Fig. 14) used to start the UPW calculations, shows that changes of the horizontal flows in the course of the UPW calculations are small and that the pre-optimized flow field already contains most of the important currents seen in Fig. 25a.

As an example of mid-depth flows, model velocities in 800 m depth are shown in Fig. 26a together with velocity differences to the initial geostrophic field (Fig. 26b). From the meridional salinity section in Fig. 20a it can be seen that this depth roughly coincides with the depth of the salinity minimum layer so that, in the south Atlantic, Fig. 26a describes the flow of Antarctic Intermediate Water (AAIW).

Relatively large flow velocities at 800 m depth of between 5 to $15 \cdot 10^{-2}$ m s^{-1} are found in the ACC, in the Gulf Stream and its inner recirculation and in Denmark Strait. Whereas the ACC velocities are only slightly larger than the geostrophic estimates (see

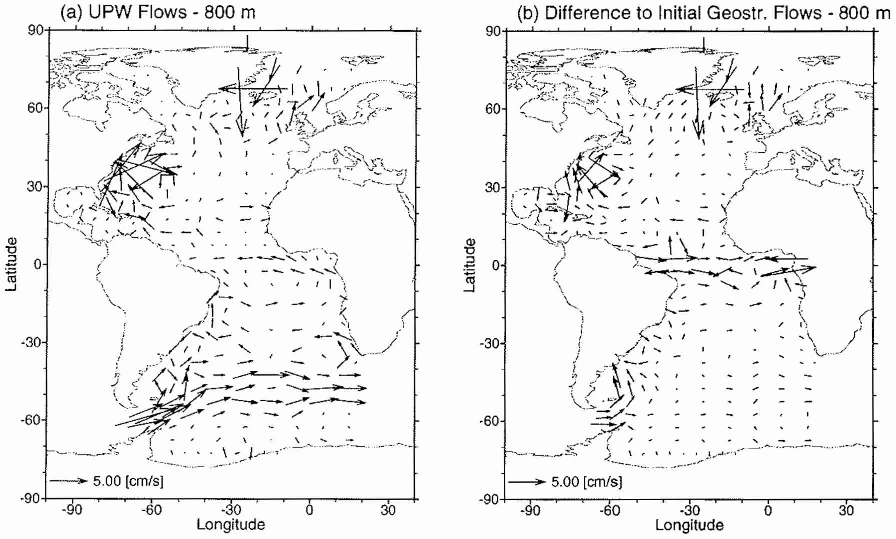

Fig. 26: Model velocities in layer 7 (700 - 900 m) (Fig. 26a) and velocity differences to the initial geostrophic velocities (Fig. 26b) for the UPW experiment.

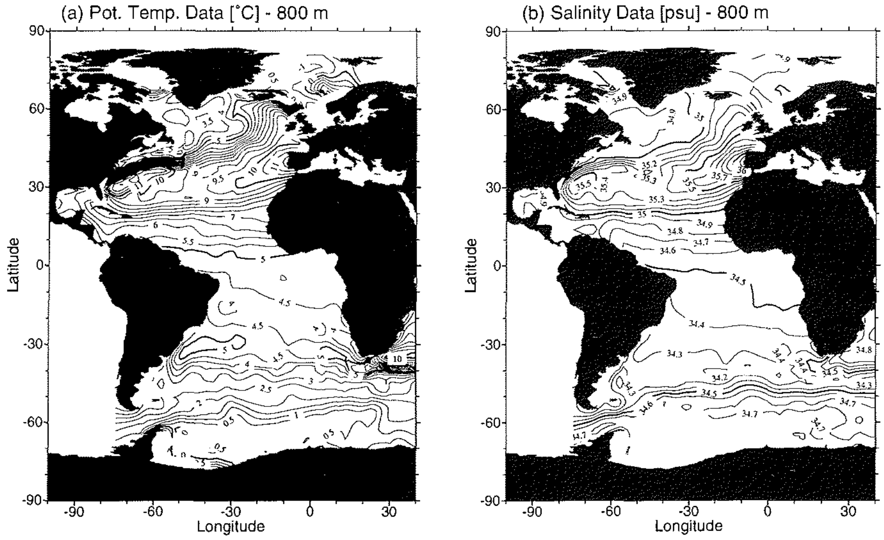

Fig 27: Distributions of (a) averaged potential temperature and (b) averaged salinity in 800 m depth in the Atlantic based on the original station-data shown in Fig 3.

Fig. 26b), the strong recirculation cell of the Gulf Stream and the large southward flows in Denmark Strait are increased by the model obviously in order to satisfy *a priori* transport constraints and to produce realistic deep water temperatures and salinities by providing cold and relatively fresh water from the Nordic Seas. In the subtropical south Atlantic at about 32°S there are two counter-clockwise gyres centered near 40°W and 5°E with flow velocities of about $2 \cdot 10^{-2}$ m s^{-1}. The northern branches of these gyres provide a net northwestward mass flux that splits into southward and northward boundary flows near 25°S at the Brazilian coast. In the model solution the northward boundary flow is deflected eastward at about 12°S, then turns northward at the African coast and flows westward along the equator into the tropical west Atlantic. As a net effect, AAIW is transported northward into the north Atlantic.

Evidence for the mid-depth model flows in Fig. 26a can be found in the temperature and salinity distributions in 800 m depth obtained from the available station data (Fig. 3) shown in Fig. 27. In the south Atlantic the marked meridional salinity front following the position of the 34.5 isoline (Fig. 27b) corresponds to the path of the ACC. The southward and northward deflections of the 34.3 and 34.4 isolines at the Brazilian coast are indications for the splitting of the currents observed in this area, and the two relative temperature maxima defined by the 5°C isotherms in the western and eastern subtropical south Atlantic (Fig. 27a) are indicative for the two gyres found in the model solution at these locations.

The southward and northward branching of the flows at about 25°S near the Brazilian coast is also supported by the distribution of chlorofluoromethanes in AAIW described by Warner and Weiss (1992). In the subtropical northwest Atlantic the temperature and salinity maxima support the deep reaching Gulf Stream recirculation cell and the presence of warm and salty waters in the northeast Atlantic corresponds to the northeasterly flows west of the British islands.

Comparison of the model flows in the south Atlantic with the map of adjusted steric height at 800 db of Reid (1989) shows a great deal of similarity in the two circulation fields. For instance, both maps agree in the position of the ACC, in the Argentine Basin they both show two meanders of the ACC extending northward up to 40°S with an intrusion of subtropical water in-between, and in the Weddell Sea weak clockwise circulation (the Weddell Gyre) is indicated in both pictures. Differences are the two mid-depth subtropical gyres in the UPW solution where Reid shows only one such counter-clockwise circulation extending across the entire Atlantic and the eastward flow in the tropical south Atlantic that occurs further south in the model solution compared with Reid's map. The temperature and salinity fields in Fig. 27 seem to support for the existence of two separate gyres at 32°S and it should be noted that data coverage in Reid's analysis is poor and probably insufficient to resolve sub-basin scale features in this area. Two distinct gyres in the subtropical south Atlantic are also seen in the map of dynamic height in 500 m depth (relative to 1500 m) of Burkov *et al.* (1973; map reproduced as Fig. 3.11 in Reid (1981)).

Meridional Mass and Heat Transport

Zonally integrated meridional and vertical transports are shown by arrows and by transport contours in Figs. 28a and 28b, respectively. The overall meridional overturning cell of the model consists of mean northward transport in the upper 1300 m of the water column, deep water formation in the Nordic Seas and Arctic Ocean, southward flow through Denmark Strait and overflow across the Iceland-Scotland Ridge (about 63°N), further sinking south of the overflows and mean southward transport in the deep Atlantic (NADW). In the south Atlantic the NADW layer rises and is incorporated into circumpolar waters between 40 and 50°S. About 8 Sv of the southward flowing NADW in the model solution derive directly from the deep water formation areas north of the overflows and about 4 Sv of mid-depth water from south of the overflows are admixed to it by entrainment during downward motion along the continental slope. These values are in good agreement with transport estimates of Swallow and Worthington (1969) and Worthington (1970).

In the south Atlantic between 70 and 45°S where property isolines rise sharply (see Figs. 19a and 20a) strong and consistent upwelling is observed over large areas and at all depths. At 1650 and 360 m depth this upwelling amounts to 37 and 25 Sv, respectively. Sverdrup (1933) attributes the upwelling of deep water in the Southern Ocean to the Ekman surface divergence caused by the specific latitudinal dependence of wind-stress in this area. Using the Trenberth *et al.* (1989) winds an Ekman divergence of 12 Sv is obtained for the Atlantic sector south of 45°S which explains about half of the observed upwelling rate in the UPW solution. Gordon (1971) analyses the integrated meridional volume transport

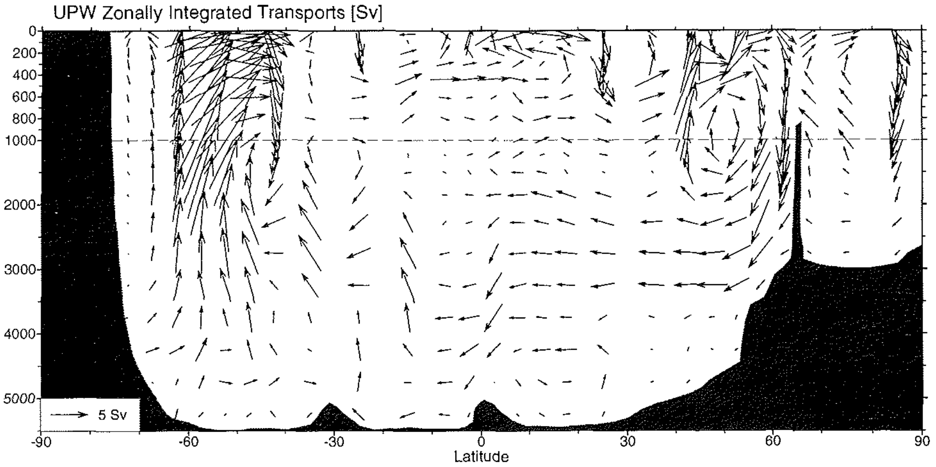

Fig. 28: Zonally integrated meridional and vertical volume transports for the UPW experiment displayed as (a) arrow field and (b) transport contour map. Arrows in Fig. 28a are vector averages of nearby horizontal and vertical transports, and transport contours are obtained by objective analysis of the vertically integrated transports and subsequent contouring. Note that Fig. 28b only extents to about 30°S and that the vertical scale changes at 1000 m depth in both figures.

around Antarctica and he also considers about one half of the upwelling to be wind induced whereas the other half is initiated by bottom water production. Highest upwelling rates in the UPW solution are found in the latitudinal band between 58 and 62°S (Figs. 28a and Fig. 30 below) which is in agreement with results of Gordon (1971). Note that the northward component of the flows in the upper 1000 m depth at about 50°S reflects the northward shift of the ACC in the south Atlantic.

To the north of the Antarctic upwelling region, at about 45°S, downwelling is observed from the surface down to about 2500 m depth (Fig. 28a). This downwelling corresponds to the tongue of low salinity water in Fig. 20a reaching from the surface at about 50°S downward and northward and ultimately feeding the layer of northward spreading AAIW. In the southern Weddell Sea downwelling prevails. However, the sinking rate is relatively small (1.3 Sv) and waters do not penetrate deeper than about 2000 m depth.

Downwelling also is observed in the centers of the subtropical gyres at about 25°S and 25°N (Fig. 28b). The water that subducts at 25°S flows northward between 200 and 600 m depth and its upper portion upwells to the surface in the equatorial region. Zonally integrated upwelling rates between 20°S and 15°N decrease rapidly with depth and amount to 9.8 and 4.2 Sv at 60 and 360 m, respectively. These values are consistent with estimates of Wunsch (1984b) obtained by inversion of hydrographic and radiocarbon data. The mean northward transport of near-surface water across the equator feeds the subduction in the north Atlantic subtropical gyre. At 25°N the downward transport (about 12 Sv) is larger

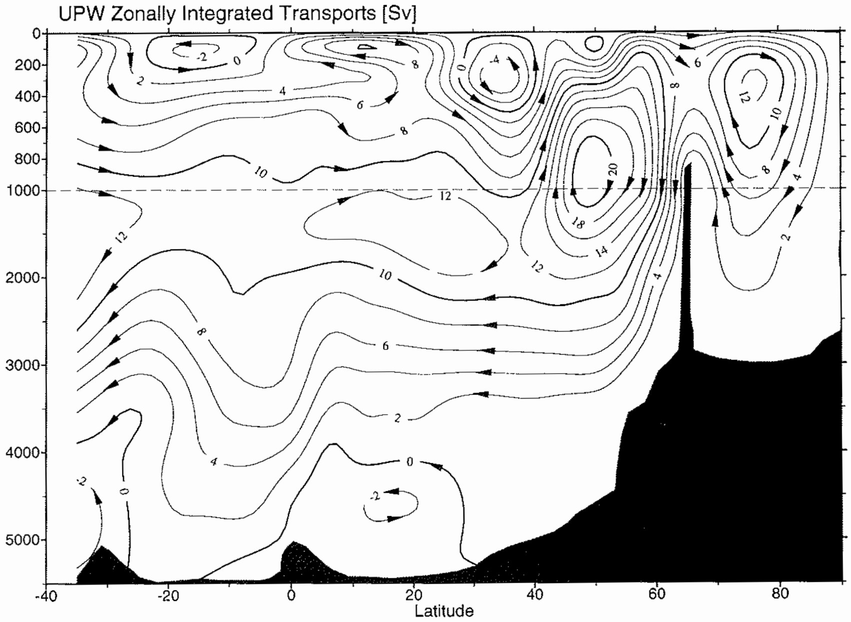
UPW Zonally Integrated Transports [Sv]

Fig. 28: Continued.

Table 4: Integrated meridional volume transports [Sv] at 30°S, the equator and 30°N for four isopycnal layers and three different model states (for definitions of layer interfaces see Table 5). Positive values indicate northward transport.

Layer	Initial	Pre-Optimized	UPW
30° N			
1	-9.49	14.61	8.49
2	0.59	-5.00	1.10
3	0.61	-10.85	-10.60
4	1.23	0.43	-0.25
Equator			
1	0	9.24	2.00
2	0	11.92	8.21
3	0	-21.12	-11.36
4	0	-0.43	0.26
30° S			
1	15.49	7.44	2.18
2	19.50	1.50	10.00
3	-0.95	-12.75	-15.80
4	1.51	3.96	3.06

than at 25°S and reaches greater depths (about 700 m). Near 40°N waters from intermediate depths rise close to the surface and the upper part of this upwelled waters flows into the Nordic Sea and Arctic Ocean. The rising of mid-depth waters near 40°N corresponds to the upward sloping of temperature and salinity isolines in that region (see Figs. 19a and 20a) with relatively homogenous distributions to the north. This homogenization might be the consequence of the mid-depth local overturning cell consisting of the 40°N upwelling and entrainment into the overflows at about 60°N. The northward transport at the bottom north of the equator and the southward transport south of the equator are related to the respective bottom water transports in the eastern basins of the Atlantic.

Table 4 gives an overview of (zonally integrated) meridional volume transports at 30°S, the equator and 30°N for four isopycnal layers representing major water masses in the Atlantic (see Table 5). Layer 1 represents the warm, near-surface waters and mean depths of its lower interface at 30°S, the equator and 30°N are 450, 280 and 500 m, respectively. The second layer reaches down to about 1450, 1300 and 1280 m depth at the three latitudes and encompasses the Antarctic Intermediate Water (AAIW, marked by a pronounced salinity

Table 5: Definition of isopycnal layers representing major water masses in the model domain.

Layer	Upper Boundary	Lower Boundary
1 upper layer	surface	$\sigma_0 = 26.8$
2 intermediate water	$\sigma_0 = 26.8$	$\sigma_2 = 36.75$
3 deep water	$\sigma_2 = 36.75$	$\sigma_4 = 45.90$
4 bottom water	$\sigma_4 = 45.90$	bottom

minimum at about 850 m depth; see Fig. 20a) and the upper third of the Circumpolar Deep Water (CDW; Peterson and Whitworth III, 1989) in the south and equatorial Atlantic and the Mediterranean Water in the north Atlantic. North Atlantic Deep Water (NADW) is represented in the third layer, and the fourth layer, which is present only in the western Atlantic, consists of bottom waters with potential temperatures below about 1.5°C (AABW). The layer definitions given above roughly coincide with layers 1 and 2, 3 to 6, 7 to 10 and 11 to 13 of Rintoul (1991).

Net (top to bottom) meridional transports across the three latitudes are small and account for the inflow through Bering Straits (0.9 Sv) and air-sea fresh-water fluxes. At all three latitudes the meridional circulation consists of northward flows in the top two layers and in the AABW layer at the bottom (30°S and equator) compensated by southward flow of NADW. The flow in the bottom layer (AABW; 3.1 Sv at 30°S) decreases and reverses along its northward path whereas the transport of NADW increases along its southward path, obviously due to incorporation of AABW and AAIW. The maximal southward transport within the NADW layer amounts to 15.8 Sv at 30°S and is comparable with results of Rintoul (1991) at the same latitude and with independent estimates of the overall strength of the meridional overturning cell (15 to 20 Sv; Warren, 1981; Roemmich and Wunsch, 1985; Broecker, 1979). At 30°N, however, the model southward transport of NADW (10.6 Sv) is significantly smaller than the literature values. The 3.1 Sv of northward flowing AABW at 30°S are in good agreement with direct current measurements in the Vema Channel (ca. 31°S) which indicated a northward flow of AABW of 4±1.2 Sv (Hogg *et al.*, 1982).

Note that the northward branch of the meridional overturning cell in the southern and equatorial Atlantic consists mainly of intermediate waters (AAIW) in layer 2 with only a relatively small contribution of warm surface waters. At 30°S, obviously, the poleward transport of the Brazil Current is closely matched by the broad northward return flow in the central south Atlantic and by the Benguela Current at the African coast resulting in small net meridional mass transport of surface waters. At the equator and in the subtropical

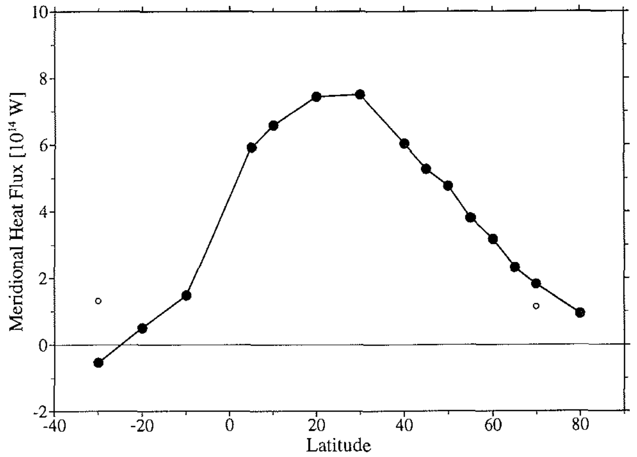

Fig. 29: Zonally integrated meridional heat fluxes for the UPW experiment. Values include advective and diffusive heat flux contributions and are for the upwind differencing scheme. Meridional heat fluxes calculated with the UPW circulation and mixing coefficients but using centered-in-space model temperatures are shown by open dots at 30°S and 70°N. At 20°N the two estimates are indistinguishable.

north Atlantic northward transport of surface water becomes more important relative to the transport of intermediate water indicating that AAIW is gradually converted into warmer, less dense near-surface water thereby loosing its southern characteristics (Schmitz and Richardson, 1991; Tsuchiya, 1989; see also Figs. 19a and 20a).

For the initial geostrophic flows of the model net meridional transports are large across 30°S and 30°N indicating that a reference level at 2500 db is inappropriate both in the subtropical south and north Atlantic. At the equator geostrophy can not be applied and initial cross-equatorial transports are set to zero. The pre-optimized circulation shows a meridional overturning cell of about the same strength as in the final UPW solution (about 12 Sv), however, the northward transport in the upper layers is about evenly distributed between the warm surface layer and the colder intermediate waters below whereas in the UPW flow field the contribution of intermediate waters to the overall northward transport in the Atlantic dominates.

Fig. 29 shows the meridional heat transport as a function of latitude calculated for the UPW solution. Due to the fact that in the upwind scheme the concentrations (temperatures) transported by a flow are not defined at the same position as the flow velocity itself but "upwind" of the flow, total heat and property transports can be systematically under- or overestimated in regions of strong temperature (property) gradients. At 30°S, for instance, the upwind scheme underestimates the total meridional heat flux because of using too low temperatures from south of 30°S for the flux calculation in the upper layers where flows are to the north and using the too high NADW temperatures from north of 30°S in the deep ocean with flows to the south. This effect amounts to almost 0.2 PW at 30°S but is much smaller in the tropical and polar north Atlantic as indicated by open dots in Fig. 29 which are calculated by using "centered" temperatures together with the UPW flows. Taking these effects into account, model heat transports north of 30°S are northward everywhere. A strong heat flux increase is observed in the tropical Atlantic indicating net heat gain of the ocean in this region. At 20°N the heat transport is maximal (about 0.75 PW) and heat fluxes steadily decrease north of 30°N corresponding to net heat loss of the ocean. Model heat fluxes are further discussed and evaluated in the context of the CS solution (using the centered-in-space differencing scheme) in section 5.3.

Vertical Flows

Vertical velocities in 1650 m depth for the UPW solution are shown in Fig. 30 and are discussed in comparison with results from pre-optimization shown in Fig. 13. As described above, vertical flows in the pre-optimization solution are weak due to the horizontal smoothness requirement applied to the w. Comparison with Fig. 30 shows that the requirement to correctly reproduce the observed temperature and salinity distributions leads to significant changes of the w field especially in the Southern Ocean, in the Norwegian/Greenland seas and south of the overflow regions at about 60°N. In these areas the magnitude of the vertical velocities w increases. Deep water formation develops in the Weddell and Greenland seas and in the Arctic Ocean, upwelling occurs in the southern Norwegian Sea, and strong downwelling found south of Denmark Straits and the Iceland-Faeroe Ridge is the result of increased deep southward flow across the overflows . Though probably not realistic on this large scale, generating a strong upwelling/downwelling cell in the Norwegian/Greenland seas for the model with its relatively coarse resolution and with a constant coefficient of vertical mixing is the only efficient mechanism to maintain the rapid vertical overturning in these areas known from observations and reflected by the very small vertical property gradients.

Consistent upwelling with average vertical velocities of about $50 \cdot 10^{-7}$ m s^{-1} (equivalent to about 150 m yr^{-1} or 37 Sv when integrated over the upwelling region) is observed in the zonal band south of the ACC between about 65 and 50°S. This upwelling is not present in the pre-optimization results and is introduced by the model obviously to correctly reproduce the upward sloping temperature and salinity isolines towards the Antarctic continent seen in Figs. 19 and 20.

Air-Sea Fluxes

Fresh-water and air-sea heat fluxes taken from the literature and from the final, optimal UPW solution are shown in Figs. 31 and 32. Error margins for the literature flux estimates are large ($\sigma_{E\text{-}P}, \sigma_Q = \pm 50\%$ are used in terms 2 and 9 of the cost function) and relatively large deviations between the "data" and the model values are tolerated. Main features in the Hellermann (1973) data (Fig. 31a) are (from south to north) loss of fresh-water due to

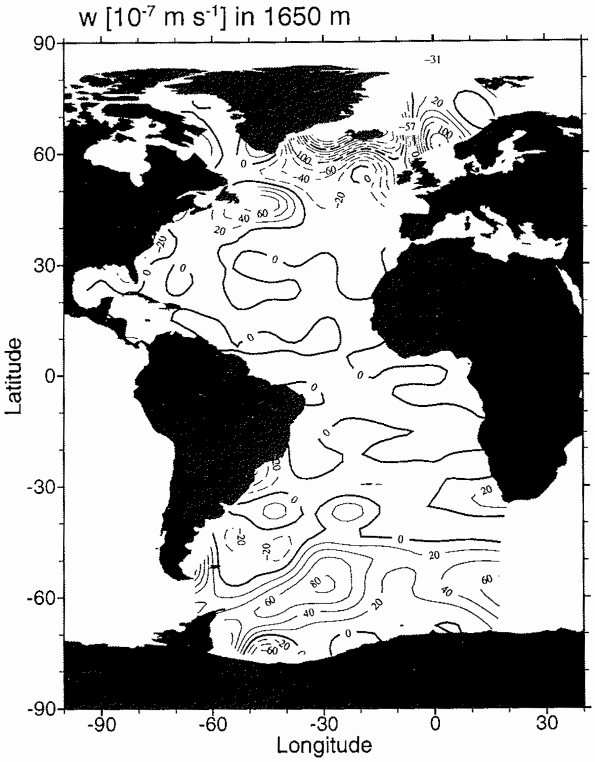

Fig. 30: Vertical velocities w [10^{-7} m s^{-1}] in 1650 m depth for the UPW experiment. Positive values (upwelling) are represented by solid lines and negative values (downwelling) by dashed lines.

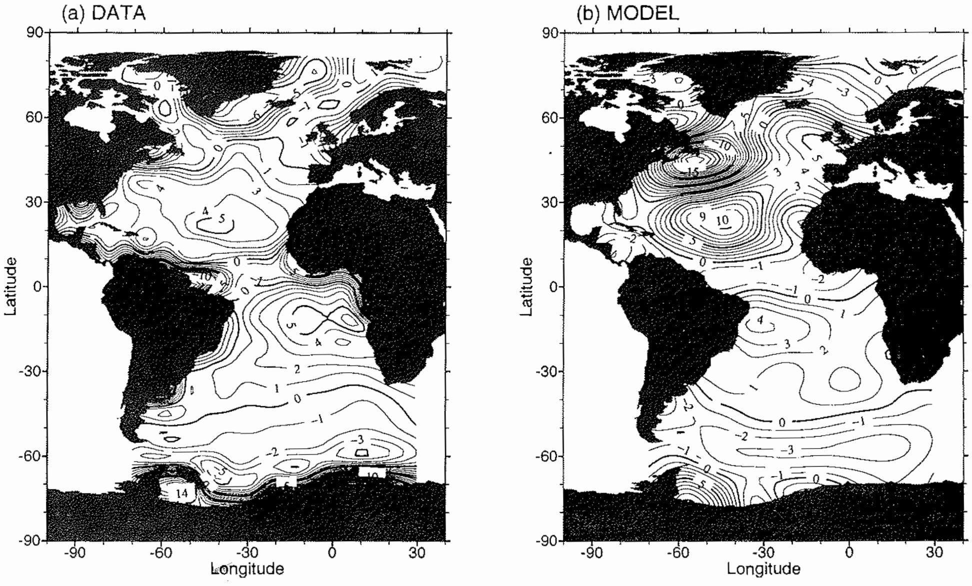

Fig. 31: Fresh-water fluxes [10^{-8} m s^{-1}] for values derived from (Hellermann, 1973) (Fig. 31a) and the UPW model solution (Fig. 31b). Positive values indicate loss to the atmosphere.

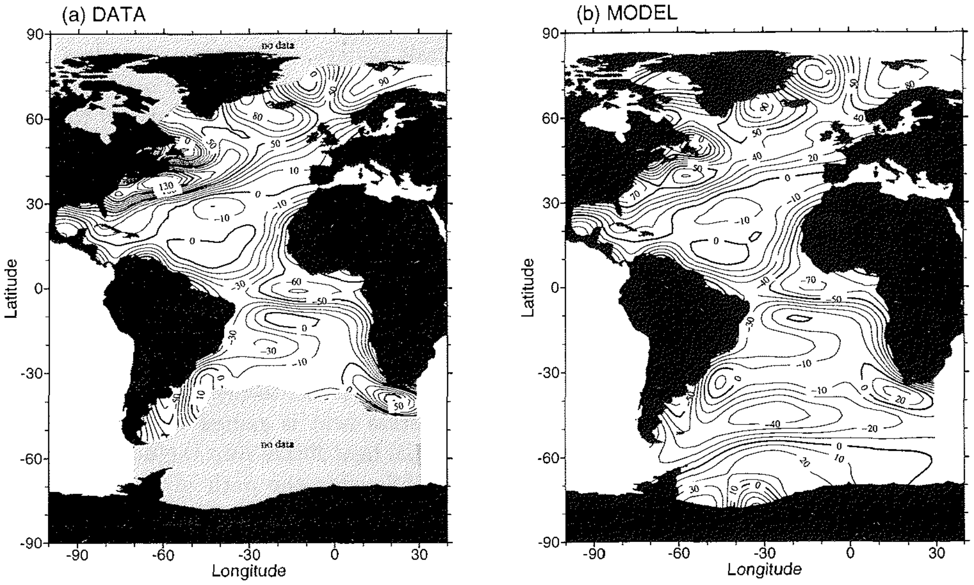

Fig. 32: Air-sea heat fluxes [W m^{-2}] for values from (Oberhuber, 1988) (Fig. 32a) and for the UPW model solution (Fig. 32b). Positive values indicate heat loss to the atmosphere.

ice formation and excess evaporation along the Antarctic continent, followed by an band of net fresh-water gain through ice melt and excess precipitation at about 60°S. In the subtropical areas (12°S and 20°N) distinct maxima of fresh-water losses to the atmosphere are due to evaporation exceeding precipitation and net gain of fresh-water is observed in the tropical Atlantic and in the north Atlantic north of about 50°N.

The model fresh-water fluxes (Fig. 31b) show a similar pattern, however, there are also significant differences. Fresh-water losses in the Weddell Sea are only about one third of Hellermann's values, the subtropical evaporation maxima are shifted towards the western basins and an intensified pair of highs and lows is developed in the north-west Atlantic. The low (precipitation exceeds evaporation) at Newfoundland Bank appears to be an artifact caused by the inability of the model (due to limited spatial resolution and large effective mixing, see below) to simulate the low salinities in the coastal waters inshore of the Gulf Stream that are caused by the southwestward flowing Labrador Current. Instead of diluting the saline Gulf Stream waters by this counterflow of low saline Labrador water, the model obviously resorts to the possibility of salt dilution by means of excessive precipitation.

The integrated net fresh-water flux north of 30°S in the model solution amounts to 0.4 Sv of water lost to the atmosphere suggesting that the Atlantic (north of 30°S) acts as a concentration basin. From Fig. 20a it can be seen that most of the northward transport of water across 30°S in the Atlantic (10 Sv of AAIW and 3.1 Sv of AABW; see Table 4) carries salinities smaller than the salinity of the southward flowing NADW, and net evaporation over the Atlantic is required to satisfy the overall salt budget. Net water vapor loss and export from the Atlantic to the Pacific and Indian Oceans of about the same magnitude as in the UPW solution are also observed by Schmitt *et al.* (1989), Baumgartner and Reichel (1975), Broecker *et al.* (1990) and Manabe and Stauffer (1988).

The annual mean air-sea heat flux data of Oberhuber (1988) (Fig. 32a) show loss of heat to the atmosphere in the entire northern and western Atlantic and gain of heat in most parts of the south Atlantic except near the Agulhas retroflection region where the ocean looses heat. South of about 40°S Oberhuber does not provide data because of lack of reliable climatological data. In this area the model heat fluxes are not tied to any data, and it is particularly interesting to investigate the heat flux results there (Fig. 32b). South of 40°S the distribution of model heat fluxes is smooth (smoothness requirement active in entire model domain) and exhibits a simple structure. Heat is lost to the atmosphere (max: 45 W m^{-2}) almost everywhere in Weddell Sea, whereas heat is gained by the ocean in the entire south Atlantic north of about 60°S. Maximal heat fluxes into the ocean (about 45 W m^{-2}) are observed in a zonal band roughly following the path of the Antarctic Circumpolar Current (ACC) between 60 and 45°S. Heat loss in Weddell Sea is due to very low air-temperatures together with strong winds, and the downward heat flux into the circumpolar waters north of Weddell Sea is probably caused by the equatorward shift (about 10° of latitude) of the ACC east of Drake Passage bringing relatively cold surface waters into areas of moderate air-temperatures. Net heat gain by the ocean in this region is also found in the maps of Bunker (1988). Integrated over the entire model domain, the Atlantic in the UPW solution is a net sink of heat (average downward flux -4 W m^{-2}). Fig. 32b suggests that this heat gain mainly occurs over the south Atlantic.

Mixing Coefficients

Mixing in the UPW model calculation is included in the heat and salt budgets and represented by a diagonal mixing tensor with constant coefficients in the entire model domain. Although being tied to best-guess values taken from the literature, the model selected optimal values for horizontal and vertical mixing coefficients $K_h = 151$ m^2 s^{-1} and $K_v = 0.08 \cdot 10^{-4}$ m^2 s^{-1} that are much smaller than the *a priori* values. Even with this small explicit mixing, the model simulated temperature and salinity distributions are much smoother than the observed fields (see Figs. 17 to 20). This is due to the inherent artificial mixing of the upwind differencing scheme (Roache, 1982)

$$\alpha = uL/2 \qquad (5.1)$$

where α is the coefficient of artificial mixing, u is the flow velocity and L is the grid size.

For typical velocities and the grid size of the model, artificial mixing coefficients are $\alpha_h = 5000 - 10,000$ m^2 s^{-1} and $\alpha_v = 1 - 4 \cdot 10^{-4}$ m^2 s^{-1} and are thus orders of magnitudes larger than the explicit mixing coefficients and also much larger than the *a priori* values. The UPW model experiment thus appears to be an overly diffusive representation of the ocean and realistic estimates of mixing coefficients can not be obtained. It should be noted that the model 'is aware' of the excessive mixing and tries to minimize the (explicit) coefficients.

5.3 Calculations with the Centered-in-Space Differencing Scheme (CS)

When the centered-in-space differencing scheme is used, the final, optimal value of the cost function F is considerably smaller (about one third) compared with the UPW experiment (Table 6). Comparison of the magnitudes of individual cost function terms for the UPW and CS cases (Table 6) shows that the CS solution is closer to the initial geostrophic velocity shear, exhibits smaller deviations of air-sea fresh-water and heat fluxes and produces temperature and salinity fields that deviate less from the observed distributions. Inspection of the horizontal distributions of model temperatures and salinities (not shown) reveals that the CS scheme is able to produce sharp and realistic property gradients in areas where the UPW scheme (due to the inherent artificial mixing) yields broad and too smooth transitions (see Figs. 18a and 18b). As a consequence, especially terms 13 and 14 of F, which measure systematic temperature and salinity deviations over larger scales (typically three grid-spacings) and which are relatively large for the UPW case because of systematically too high or too low model values on both sides of property fronts, are much smaller when the centered-in-space scheme is used. Optimal values for the iso- and diapycnal mixing coefficients ($K_h = 519$ m^2 s^{-1}, $K_v = 0.47 \cdot 10^{-4}$ m^2 s^{-1}; constant in the model domain) are close to the *a priori* values taken from the literature and are about one order of magnitude smaller than the effective mixing coefficients of the upwind scheme. The CS model diapycnal mixing coefficient amounts to about one half of the "classical" value of $1 \cdot 10^{-4}$ m^2 s^{-1} determined by Munk (1966) for the deep Pacific.

Zonally integrated flows for the CS run are displayed in Figs. 33a and 33b and exhibit an overall pattern that is similar to the UPW results in Figs. 28a and 28b. Differences are observed near 42°S, where the downwelling which in the UPW solution (Fig. 28a) reached down to about 2500 m depth is now confined to the upper 1000 m turning northward to feed the flow in AAIW layer between 1000 m and 600 m depth. The core of the northward flowing intermediate water (6 Sv isoline in Fig. 33b) monotonically rises from about 800 m depth at 32°S to about 400 m depth at the equator. As in the UPW solution, the upper part of the AAIW upwells to the ocean surface south of the equator, whereas the core of the AAIW crosses the equator before reaching the surface north of the equator and the deepest portion of AAIW continues its northward flow in about 800 m depth and is brought close to the surface north of 40°N.

The overall strength of the meridional overturning cell in the CS experiment (about 15 Sv at 30°S; see Table 7) roughly coincides with results for the UPW case, however, the southward transport of NADW is now (unlike in the UPW run) almost constant at all latitudes and amounts to about 13 Sv at 30°N. The flow in the bottom layer is northward everywhere decreasing from 3 Sv at 30°S (about the same as for UPW) to 1 and 0.3 Sv at the equator and 30°N, respectively. At 30°S no net northward transport of warm water (layer 1) is observed, and except for the 3 Sv of bottom water flow, the NADW transport is compensated by northward flow of AAIW (11.3 Sv). At the equator the relative contribution of warm surface water and intermediate water to the northward flow

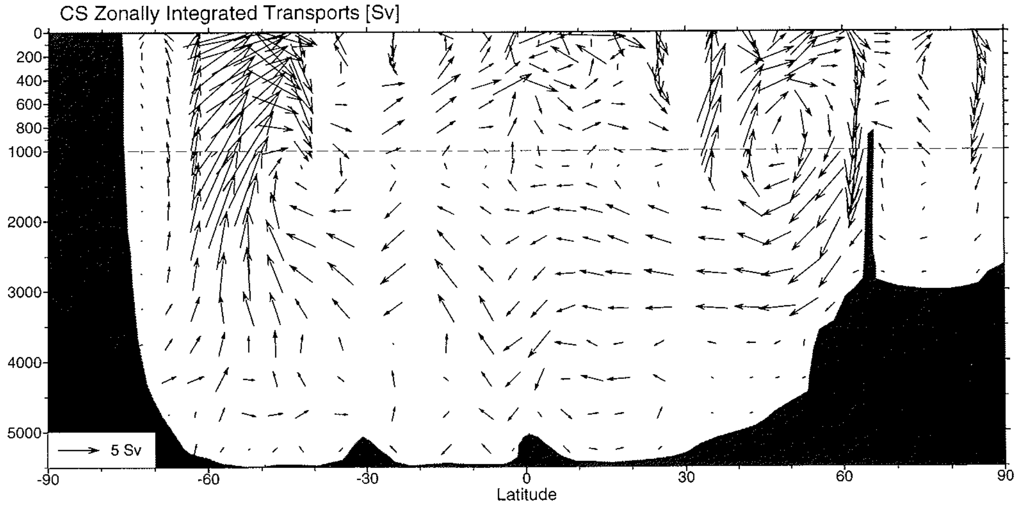

Fig. 33: Same as Fig. 28 but for the CS experiment.

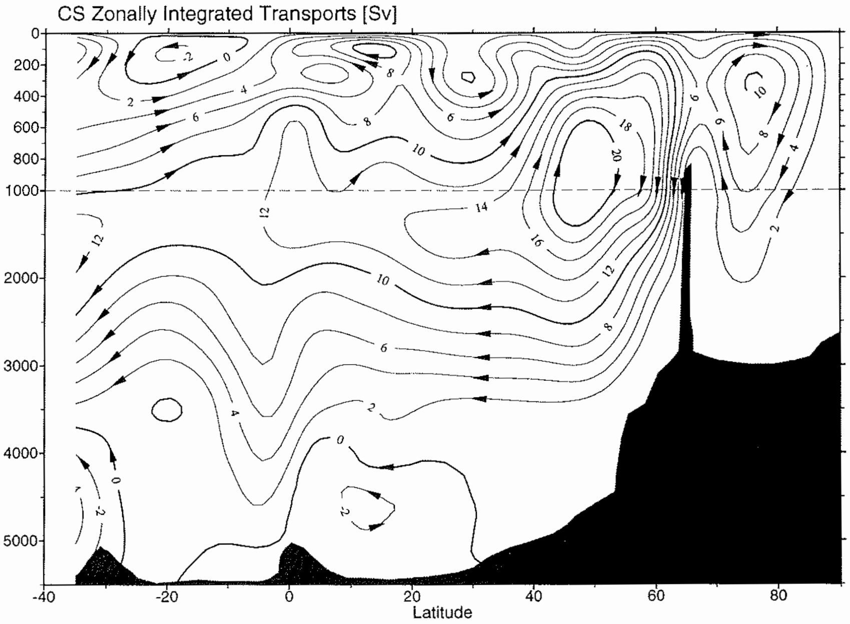

Fig. 33: Continued.

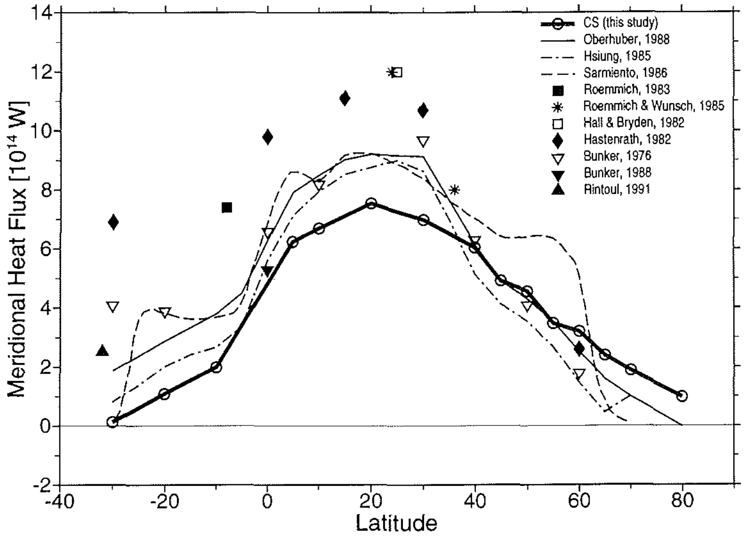

Fig. 34: Zonally integrated meridional heat fluxes for the CS experiment together with estimates from the literature.

is about 1:2 and at 30°N the warm surface water dominates. This splitting of the northward transport between the top two layers corresponds closely to results of the UPW experiment. The southward export of cold deep water from the Nordic Seas across the overflows near 63°N is somewhat smaller compared with UPW, the equatorial upwelling is somewhat larger and seems to originate at slightly greater depths and the Antarctic upwelling rate is smaller than in the UPW solution.

The meridional heat transport of the CS solution is shown in Fig. 34 together with independent heat transport estimates from the literature obtained by analysis of hydrographic sections, surface flux balances and from ocean circulation models. The thin solid line in Fig. 34 represents the northward oceanic heat transport based on Oberhuber's (1988) annual mean net air-sea fluxes assuming a northward heat transport at 70°N of 0.1 PW (Hastenrath, 1982; Hsiung, 1985). After initialization, the model starts with these heat flux values, and any difference of the final northward heat transport in the model from the Oberhuber (1988) curve is related to modifications of the model surface fluxes. Overall, model heat fluxes are smaller than literature values everywhere except north of 40°N. The maximal model heat transport is observed near 20°N (0.75 PW; see Table 8) and amounts to only 63% of the values of Hall and Bryden (1982) and Roemmich and Wunsch (1985), both based on transport calculations using hydrographic data. In the south Atlantic model heat fluxes decrease to small values, and at 30°S the heat flux is almost zero reflecting that

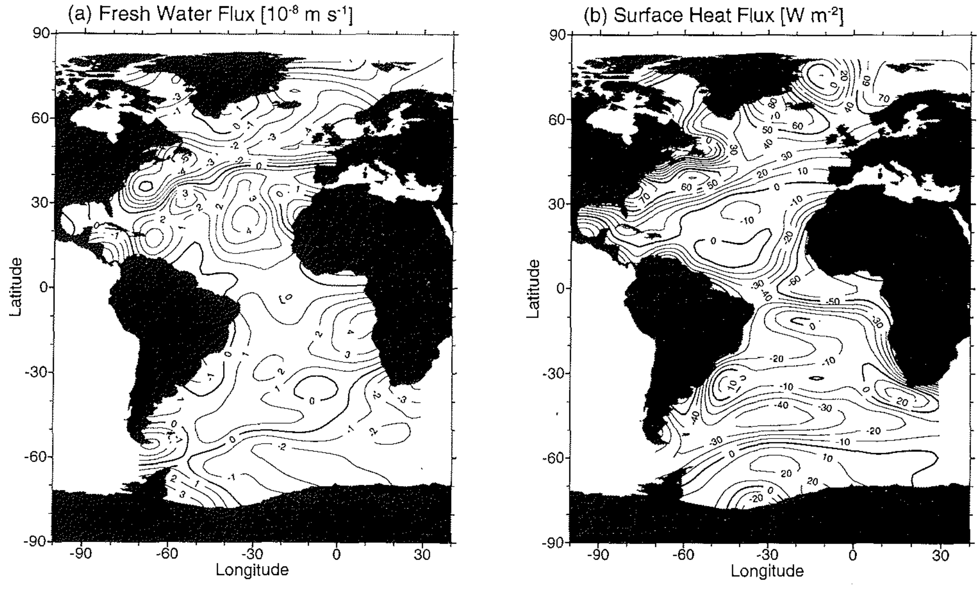
(a) Fresh Water Flux [10^{-8} m s^{-1}]

(b) Surface Heat Flux [W m^{-2}]

Fig. 35: (a) Air-sea fresh-water fluxes and (b) heat fluxes for the CS case.

in the zonal average no warm surface water contributes to the northward branch of the meridional overturning cell (Table 7).

Air-sea fresh-water and heat fluxes of the CS solution are displayed in Fig. 35. Comparison with Fig. 31 shows that the fresh-water fluxes are now much closer (see also terms 2 and 3 in Table 6) to the *E-P* data of Hellermann (1973) that are used for model initialization and reference. Most noticeably, the extreme precipitation respectively evaporation maxima south of Newfoundland and in the subtropical north Atlantic in the UPW solution (Fig. 31b) are no longer present in the CS results and values are close to *E-P* data. It appears that in the UPW solution the excessive precipitation south of Newfoundland is required to compensate the large salt transport across the Gulf Stream/Labrador Current property front (see Fig. 18a) due to the large artificial mixing of the upwind differencing scheme. With the much smaller diffusive transports in the CS run the need for fresh-water supply in this area is reduced. However, the CS solution still shows precipitation exceeding evaporation over large parts of the Gulf Stream path. The pattern of surface heat fluxes is similar to the UPW fluxes. The major difference to Oberhuber's (1988) data are the relatively small heat losses over the Gulf Stream in the west Atlantic. As in the UPW solution, overall, the Atlantic acts as a concentration basin loosing 0.23 Sv of fresh-water. The average net heat gain in the CS case amounts to 3.7 W m^{-2} (Table 8).

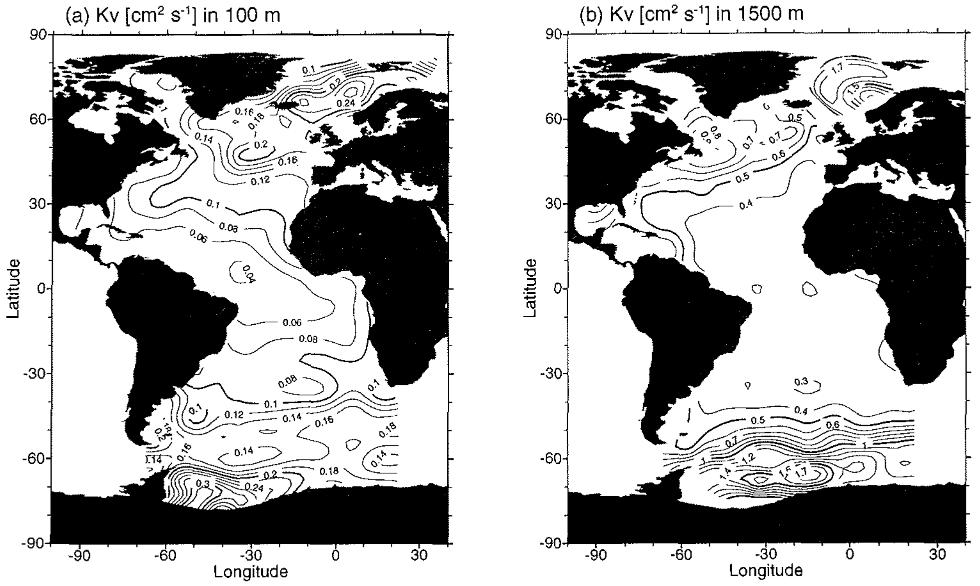

Fig. 36: Distributions of optimal diapycnal mixing coefficients K_v in (a) 100 m and (b) 1500 m depth as obtained by the CS-N experiment.

5.4 Diapycnal Mixing Linked to Stability (CS-N)

For the CS-N experiment the centered-in-space differencing scheme is used as for CS, but now mixing is parameterized differently. Diapycnal mixing coefficients are no longer assumed to be constant in the model domain but are set proportional to the inverse Brunt-Väisälä frequency (see sections 2.2.5 and 3.4) following suggestions of Gargett (1984) and Gargett and Holloway (1984). Because the spatial distribution of inverse Brunt-Väisälä frequency N^{-1} is derived from the hydrographic data, the only parameter to be determined is the constant a_0 in (3.7) which corresponds to the square of the model mixing parameter p_{kv} (see (3.6)). Other mixing parameterizations have been proposed in the literature, and related model runs are planned for the future. The second difference of the CS-N experiment compared with UPW and CS runs is the use of the isopycnal mixing tensor (3.9) which in regions of strongly sloping isopycnals like in the ACC belt results in a more effective vertical property transport.

The optimal value of the constant $a_0 = 0.72 \cdot 10^{-7}$ m^2 s^{-2} determined by the CS-N run is slightly smaller than the value of Gargett (1984) ($1 \cdot 10^{-7}$ m^2 s^{-2}). Diapycnal mixing coefficients obtained with this value of a_0 are shown in Figs. 36a, 36b and 37. It should be noted that the spatial variability of K_v reflects the spatial variation of inverse Brunt-

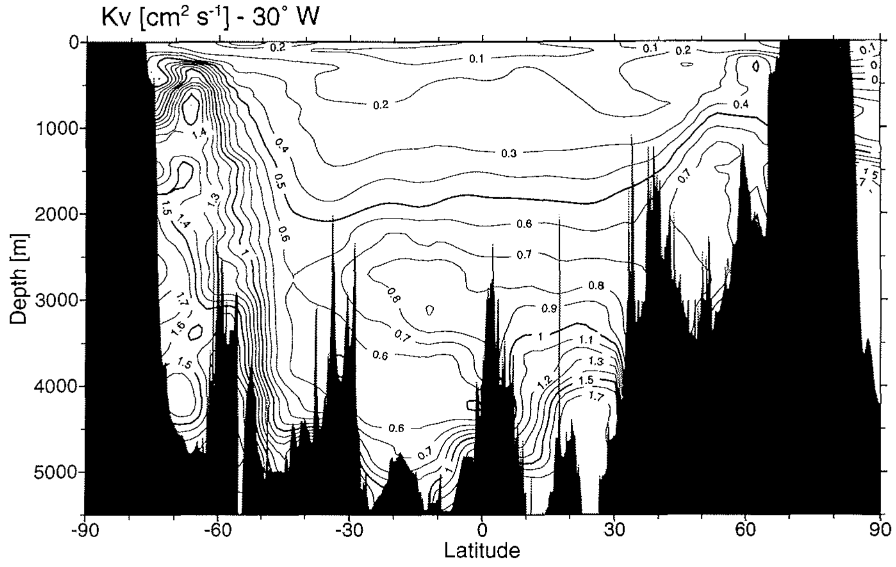

Fig. 37: Optimal diapycnal mixing coefficients K_v along 30°W in the Atlantic as obtained by the CS-N experiment.

Väisälä frequency in the Atlantic, the absolute values of the K_v, however, are determined by the model, the requirement of reproducing realistic temperature and salinity distributions probably being the most important constraint. In 100 m depth (Fig. 36a) very small values of about $0.05 \cdot 10^{-4}$ m^2 s^{-1} are observed in the strongly stratified thermocline of the tropical Atlantic. Values increase poleward and amount to about $0.2 \cdot 10^{-4}$ m^2 s^{-1} in the polar oceans. At greater depths (Fig. 36b) diapycnal mixing coefficients are larger. Values are about $0.35 \cdot 10^{-4}$ m^2 s^{-1} in the tropical and subtropical regions, they amount to about $0.7 \cdot 10^{-4}$ m^2 s^{-1} north of the Gulf Stream and exceed the Munk (1966) value in the Nordic and Weddell Seas (about $1.5 \cdot 10^{-4}$ m^2 s^{-1}). The meridional section of K_v along 30°W in Fig. 37 shows the increase of diapycnal mixing coefficients with depth, high values in the relatively homogenous deep water masses south of 60°S, in the Nordic Seas and in the deep eastern Atlantic between equator and 30°N.

Final, optimal values of total cost function and individual terms for the CS-N calculations (Table 6) are of about the same size as for the case of constant mixing coefficients and cartesian mixing tensor (CS run). Also, integrated volume and heat transports for the two cases are similar (Tables 7 and 8) indicating that the model solutions are relatively insensitive to details of the spatial dependence of mixing coefficients. On the basis of the present model, no specific parameterization of mixing coefficients appears to be preferable.

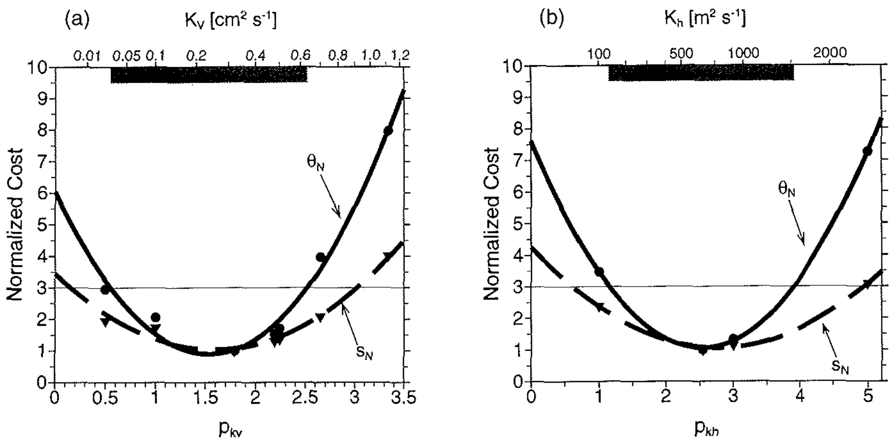

Fig. 38: Normalized values of cost function terms 13 (systematic temperature deviations θ_N; dots and solid line) and 14 (systematic salinity deviations s_N; triangles and dashed line) for (a) different diapycnal mixing parameters p_{kv} and (b) different isopycnal mixing parameters p_{kh} (for experiment CS-H).

The sensitivity of the model to different values of the (constant) diapycnal mixing coefficient K_v has been analyzed for the CS-H case (discussed in detail in the next section). For a specific, *a priori* choice of P_{kv}, term 15 of the cost function is used to force the model diapycnal mixing coefficient to the *a priori* value using a large weight factor for this term. Then, running the model to the minimum of F leads to adjustments of model flows and air-sea fluxes, the overall goal being to produce the best possible agreement between model property fields and observations, given the prescribed value for the diapycnal mixing. In case the final, optimal value of F and especially the magnitudes of terms measuring deviations between model property fields and observations (terms 11 to 14) depend strongly on p_{kv} and a narrow minimum is found, one could conclude that the model is able to determine diapycnal mixing coefficients well, whereas in case the cost function terms are relatively insensitive to p_{kv} the range of acceptable values is wide.

Model calculations for prescribed diapycnal mixing coefficients between 0.02 and 1.1 $\cdot 10^{-4}$ m^2 s^{-1} have been performed and normalized values of cost function terms 13 and 14, representative for systematic deviations between model temperatures, respectively salinities, and data, are shown in Fig. 38a. The Resulting values for both terms can be satisfactorily approximated by parabolas with the minimum position (0.25 $\cdot 10^{-4}$ m^2 s^{-1}) closely corresponding to the K_v value of the CS-H run (see below). Model/data salinity deviations (triangles and dashed curve) are much less dependent on mixing than temperature deviations (dots and solid curve) indicating that diffusive fluxes play a smaller role in salt budgets compared to heat budgets (because of relatively smaller concentration gradients). Taking the standpoint to reject solutions with systematic temperature deviations exceeding three times the optimal value a (large) range of acceptable diapycnal mixing coefficients between 0.03 and 0.62 $\cdot 10^{-4}$ m^2 s^{-1} is found. One can argue that the present model allows acceptable solutions with almost vanishing diapycnal mixing whereas values of K_v greater 0.8 $\cdot 10^{-4}$ m^2 s^{-1} (constant in model domain) are incompatible with available temperature data. Similar sensitivity studies for the isopycnal mixing coefficient K_h (Fig. 38b) also show parabolic dependence of model to data deviations on p_{kh}, with temperature again being more sensitive than salinity. Using the same criterion as above the range of acceptable values is $100 \leq K_h \leq 1500$ m^2 s^{-1} . It may be expected that the uncertainty of the constant a_0 that determines the absolute magnitudes of diapycnal mixing coefficients in the CS-N run (Figs. 36 and 37) is of the same order of magnitude as the uncertainty of K_v in the case of constant coefficients (see Fig. 38a) and thus probably amounts to about $\sigma_{a_0} = \pm 100\%$.

5.5 Adding Heat Flux Constraints (CS-H)

Common feature of the UPW, CS, and CS-N solutions presented above is a relatively weak meridional overturning cell with related relatively small northward heat transports (see Tables 7 and 8 and Fig. 34). With these results in mind the cost function F of the model was extended to include *a priori* heat transport constraints of the form

$$\frac{(\sum_i u_i \theta_i^* - H)^2}{\sigma_H^2} \tag{5.2}$$

where H is an *a priori* heat transport estimate across a given section, σ_H is its uncertainty, u_i and θ_i^* are volume flow and temperature value transported by the flow and summation is over all interfaces comprising the section. Additional cost function terms of this form were used to enforce meridional model heat fluxes at various latitudes (20°S: 0.7 PW, 10°S: 0.9 PW, 5°N: 1.0 PW, 20°N: 1.4 PW, 30°N: 1.0 PW, 40°N: 0.6 PW, 50°N: 0.4 PW) that are compatible with literature values (see Fig. 34) and are larger than the CS heat fluxes.

Table 6 shows that the final value of the cost function for this experiment is larger compared with CS and CS-N (factor 1.7) but still considerably smaller than the minimal value of F obtained with the upwind differencing scheme (UPW). The velocity shear and *E-P* deviations are only one half and the systematic temperature and salinity deviations (terms 13 and 14) are only about one third of the respective UPW values. Smoothness terms for horizontal velocities in the equatorial band, for the reference velocities u_r and for the vertical velocities w, however, are larger than in the UPW run indicating, for instance, rougher horizontal fields and probably larger magnitudes of the vertical velocities. In view of the additional and at first sight restrictive heat transport constraints in the cost function of the CS-H experiment, the overall increase of F compared with the previous centered-in-space runs CS and CS-N is surprisingly small. Because cost function values are still smaller than for the UPW case, the CS-H solution can be considered about as "good" with respect to overall model goals as the previous solutions UPW, CS and CS-N.

The relatively small increase of the total cost function value compared with the CS case suggests that the additional *a priori* heat transport constraints of the CS-H experiment

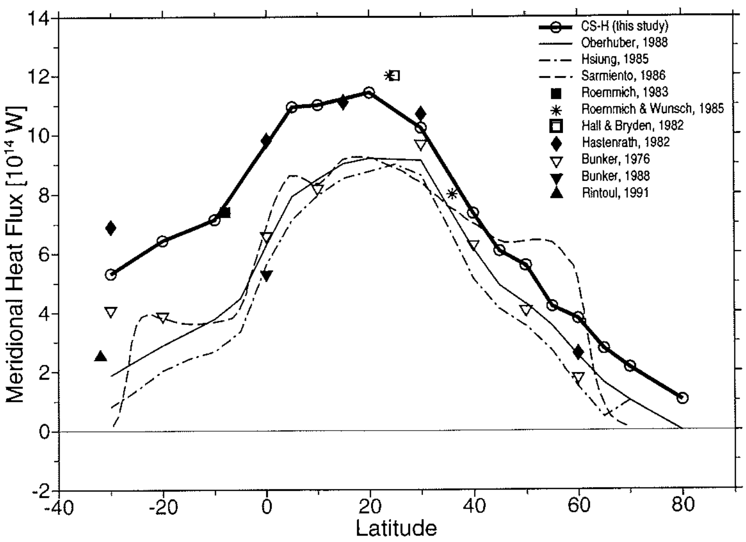

Fig. 39: Zonally integrated meridional heat fluxes for the CS-H experiment together with estimates from the literature.

could be satisfied. This is confirmed in Fig. 39 that shows zonally integrated northward heat fluxes of the CS-H solution together with estimates from the literature. Deviations from the *a priori* target values is usually less than 0.1 PW and comparison with Fig. 34 reveals that model heat transports are now between 0.3 and 0.5 PW higher than the CS fluxes. The largest increases are found in the subtropical south Atlantic. In contrast to the CS case, model heat fluxes for the CS-H experiment are on the higher end of published estimates. Values are systematically larger than results based on surface energy budgets (Oberhuber, 1988; Hsiung, 1985; Bunker, 1976) and also larger than the model heat fluxes of Sarmiento (1986). However, CS-H heat transports are still somewhat smaller than the estimates of Hastenrath (1982) at 32°S and Hall and Bryden (1982) and Roemmich and Wunsch (1985) at 24°N.

Volume transports at 30°N, the equator and 30°S in Table 7 show that the increased northward heat transport of the CS-H solution relative to the CS run is accompanied by a stronger meridional overturning cell. The southward transport of NADW in layer 3 that amounts to between 12.9 and 14.8 Sv in the CS case is increased by 35% to about 18.2 Sv at all three latitudes. The northward bottom water flow in layer 4 is almost identical to the CS case (3.0, 0.9 and 0.3 Sv at 30°S, the equator and 30°N, respectively) but the northward flow in the top two layers is larger now in order to compensate for the increased transport of NADW. Some differences are observed in the relative contributions of warm, near-surface water (layer 1) and intermediate water (layer 2) to the combined northward transport occurring in the upper 1500 m depth. At 30°S the northward flow, as in the CS solution, consists predominantly of AAIW, but in the CS-H case there is a significant contribution of warm water (27%) to the total northward flow. Near surface water and intermediate water contribute about equally at the equator, and at 30°N the northward transport of warm water dominates. It is interesting to note that the increased strength of meridional transports does not imply stronger deep water export from the Nordic Seas or stronger upwelling in the Antarctic and the equatorial band (see Table 7). Average net heat gain over the model domain (0.8 W m^{-2}) is much smaller compared with the CS solution whereas the net fresh-water loss of 0.17 Sv is of the same magnitude. Optimal values for iso- and diapycnal mixing (648 m^2 s^{-1} and 0.32 $\cdot 10^{-4}$ m^2 s^{-1}) are somewhat larger, respectively smaller compared with the CS solution.

The pattern of zonally integrated flows shown in Figs. 40a and 40b is similar to the corresponding pictures for the CS experiment (Figs. 33a and 33b) except that overall transport rates are larger for the CS-H case. A difference is the net northward near-surface flows at 30°S in the CS-H solution. Vertical velocities in 1650 m depth for the CS-H experiment shown in Fig. 41 are larger than the corresponding w's of the UPW solution (Fig. 30) especially in the central Atlantic where nearby upwelling/downwelling cells are frequent and the overall field is rougher, as expressed by the relatively large value of term 5 of the cost function (Table 6). Main features like the Antarctic upwelling, the upwelling near Newfoundland and the downwelling south of the overflows are seen in both solutions, CS and CS-H.

Air-sea fresh-water and heat fluxes of the CS-H solution are shown in Figs. 42a and 42b. Comparison of fresh-water fluxes with Hellermann's (1973) *E-P* data in Fig. 31a

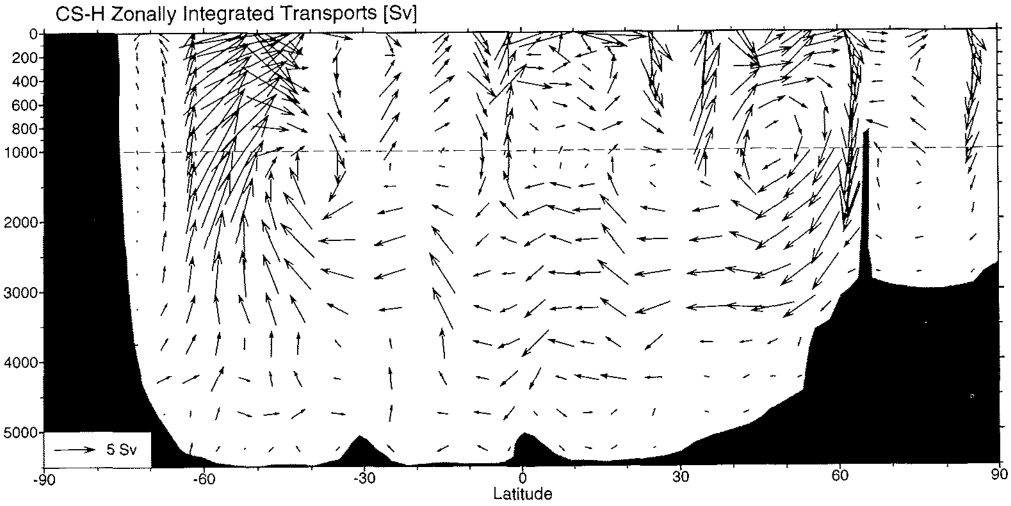

Fig. 40: Same as Fig. 28 but for the CS-H experiment (model with additional heat flux constraints).

shows broad agreement between the two fields. Net fresh-water gain is found in the equatorial region, evaporation exceeds precipitation (somewhat smaller values than Hellermann (1973)) in the subtropical north and south Atlantic and net fresh-water input occurs at high latitudes. Most noticeable differences are the shift of a precipitation maximum, which in Hellermann's data is located along the eastern coast of Greenland, to the south-east roughly following the position of Gulf Stream and North Atlantic Current and the restriction of net fresh-water loss (due to ice formation) to the western Weddell Sea whereas Fig. 31a shows large values of fresh-water loss all along the Antarctic coast. Air-sea heat fluxes of the CS-H solution (Fig. 42b) closely resemble Oberhuber's (1988) annual mean heat flux estimates (Fig. 32a). Unlike the CS solution that exhibited maximal heat losses along the Gulf Stream path of no more than 70 W m^{-2} (see Fig. 35b), the CS-H solution closely reproduces Oberhuber's estimate of 130 W m^{-2} in this area. Along the position of the ACC in the south Atlantic, where Oberhuber does not provide data, the CS-H solution (like UPW and CS solutions) shows net heat gain by the ocean.

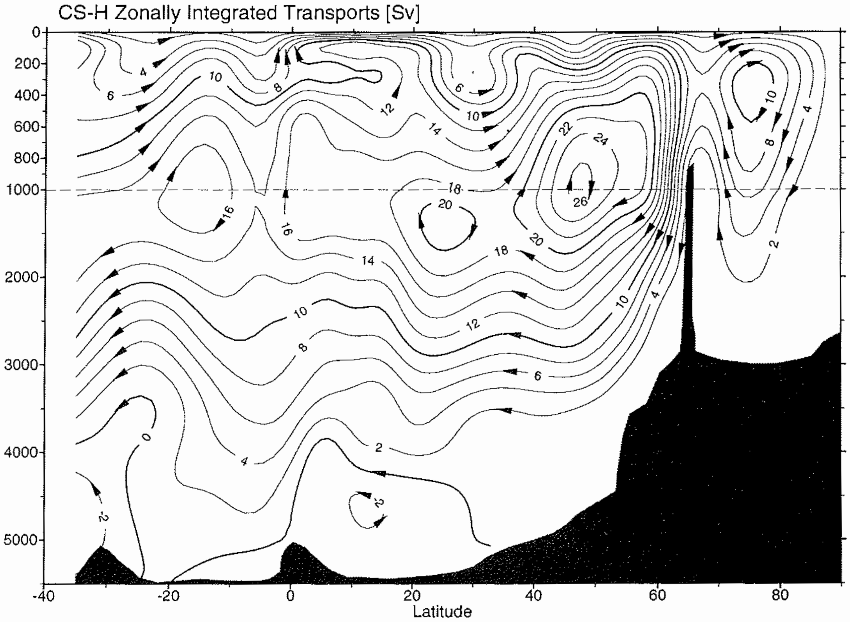

Fig. 40: Continued.

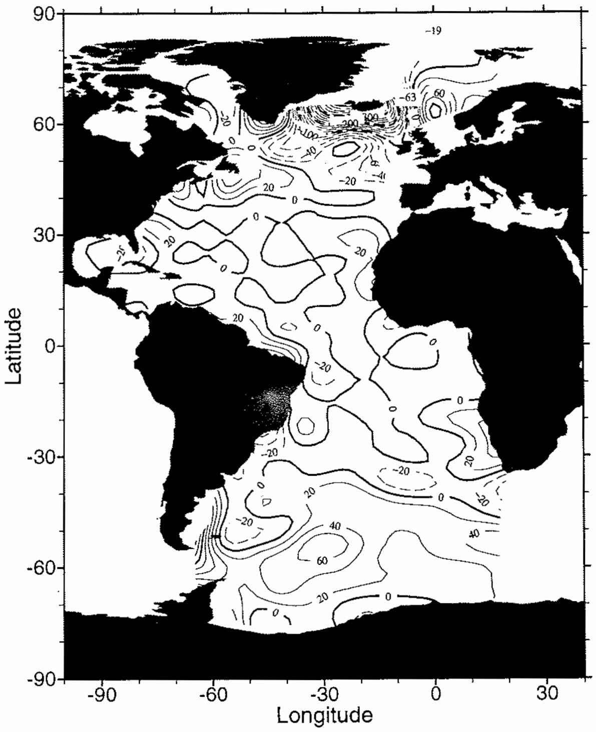

Fig. 41: Vertical velocities w [10^{-7} m s^{-1}] in 1650 m depth for the CS-H experiment. Positive values (upwelling) are represented by solid lines and negative values (downwelling) by dashed lines.

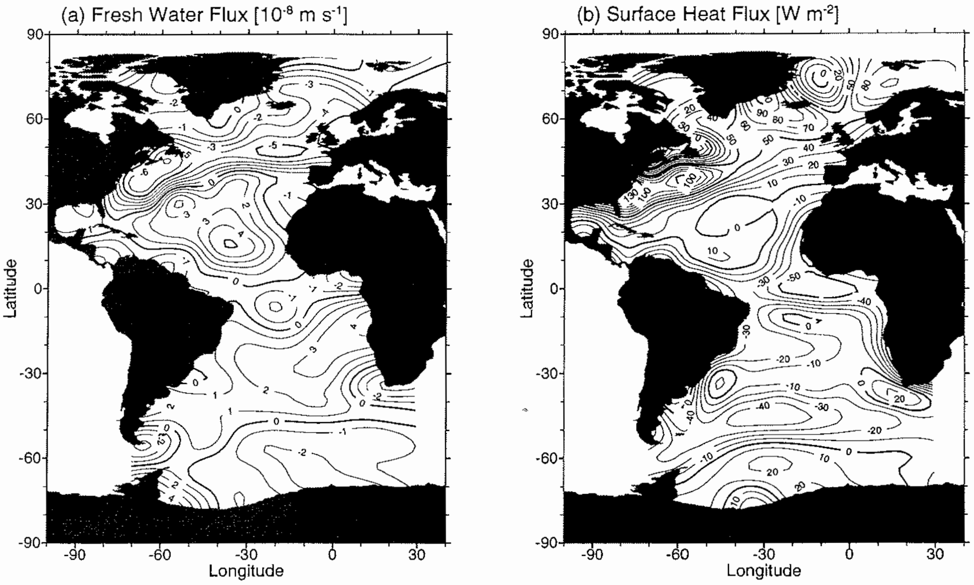
(a) Fresh Water Flux [10^{-8} m s^{-1}]

(b) Surface Heat Flux [W m^{-2}]

Fig. 42: (a) Air-sea fresh-water fluxes and (b) heat fluxes for the CS-H case.

Table 6: Weight factors and values of total cost function and individual terms (normalized to values of UPW case) for different numerical experiments. For meaning of terms see Table 1 and for a description of numerical experiments see Table 3.

	Term	Weight	UPW	CS	CS-N	CS-H
$\sum$	total	–	1	0.32	0.35	0.55
1:	velocity shear	1	1	0.56	0.54	0.65
2:	E-P data	10	1	0.32	0.31	0.44
3:	E-P smoothness	10	1	0.46	0.47	0.50
4:	linear vorticity	0.1	1	0.77	0.74	0.91
5:	w smoothness	50	1	1.02	0.98	1.28
6:	u_r smoothness	1	1	0.99	1.00	1.69
7:	smoothness equ. band	0.1	1	0.92	1.21	1.21
9:	Q data	1000	1	0.71	0.70	1.12
10:	Q smoothness	5	1	0.86	0.85	1.05
11:	θ boxwise	0.05	1	0.79	1.00	0.93
12:	s boxwise	0.05	1	0.78	0.96	0.92
13:	θ neighborhood	0.05	1	0.19	0.24	0.30
14:	s neighborhood	0.05	1	0.28	0.29	0.36

Table 7: Summary of model volume transports [Sv] for different numerical experiments. Positive values indicate northward or upward flux. For a description of numerical experiments see Table 3 and for layer definitions see Table 5 and section 5.2.5.

	UPW	CS	CS-N	CS-H
Layer transports at 30°N:				
Layer 1	8.5	9.3	9.3	13.4
Layer 2	1.1	2.1	1.8	3.4
Layer 3	-10.6	-12.9	-12.7	-18.4
Layer 4	-0.2	0.3	0.4	0.3
Layer transports at equator:				
Layer 1	2.0	4.2	4.2	8.7
Layer 2	8.2	8.2	8.3	7.4
Layer 3	-11.4	-14.3	-14.5	-18.0
Layer 4	0.3	1.0	1.0	0.9
Layer transports at 30°S:				
Layer 1	2.2	-0.1	-0.2	3.9
Layer 2	10.0	11.3	11.0	10.5
Layer 3	-15.8	-14.8	-14.6	-18.2
Layer 4	3.1	3.0	3.1	3.0
Deep (≥360 m) southward flow through Denmark Strait and across Iceland-Scotland-Ridge:	-8.7	-7.6	-7.6	-8.0
Equatorial upwelling [20°S – 15°N]:				
60 m	9.8	10.9	11.6	7.7
360 m	4.2	6.7	6.4	2.3
Antarctic upwelling:				
360 m	24.9	19.4	18.2	18.3
1650 m	37.0	33.3	31.4	36.6

Table 8: Heat fluxes, fresh-water fluxes and mixing coefficients for different numerical experiments (see Table 3 for a description of numerical experiments).

	UPW	CS	CS-N	CS-H
Meridional heat transport [PW]:				
50°N	0.48[1]	0.46	0.47	0.56
30°N	0.75[1]	0.70	0.72	1.02
20°N	0.75[1]	0.75	0.75	1.14
5°N	0.58[1]	0.62	0.63	1.09
10°S	0.15[1]	0.20	0.22	0.71
30°S	-0.05[1]	0.12	0.17	0.53
Average net heat gain [W m^{-2}] *over model domain:*[2]	4.0	3.7	3.7	0.8
Net fresh-water loss [Sv] *over model domain:*	0.30	0.23	0.24	0.17
Mixing coefficients				
K_h [m^2 s^{-1}]	≥5000[4]	519	573	648
K_v [$\cdot 10^{-4}$ m^2 s^{-1}]	≥1[4]	0.47	0.72[3]	0.32

[1] Using "upwind" temperatures with UPW flows (see text).

[2] Surface area of model domain: $8.99 \cdot 10^{13}$ m^2.

[3] Value of a_0 [10^{-7} m^2 s^{-2}] in $K_v = a_0 N^{-1}$. For spatial distributions of K_v see Figs. 36 and 37.

[4] Artificial mixing of the upwind scheme.

Chapter 6

Discussion and Conclusions

The adjoint method has been successfully applied to obtain optimal circulation, air-sea fluxes and mixing coefficients that, in a steady model with exact mass, heat and salt conservation, can satisfactorily reproduce the measured distributions of temperature and salinity in the Atlantic. Profiles of horizontal velocities in the optimal model solution resemble initial geostrophic velocity profiles except for constant velocity shifts (the previously unknown reference velocities u_r) and the model circulation is considered to be consistent with the principle of geostrophy. Changes to the shapes of the geostrophic profiles can be controlled and be kept small. The present method can be interpreted as a new approach to the classical problem of determining the reference velocities left unknown by pure geostrophic calculations. Here, the reference velocities are chosen in a way that makes the resulting circulation field mass conserving and leads to a correct prediction of temperature and salinity distributions in the ocean while satisfying heat and salt budgets exactly.

The different model objectives (preserving geostrophic shear, obtaining realistic temperature and salinity distributions, smoothness of various properties, etc.) are implemented and enforced by way of the model cost function F. All contributions to the cost function except for the smoothness and linear vorticity terms (see Table 1) are normalized by weighting with estimated variances σ^2, respectively. The weights α_i with which these normalized terms appear in the cost function F initially were all set to 1. Regular evaluations of intermediate model states in the course of the iterations showed that modifications of the α_i were necessary in order to obtain a final, optimal solution consistent with all of the requirements specified in the cost function (see Table 6 for final weights). For instance, terms 11 to 14 (deviations from temperature and salinity data) had to be down-weighted relative to term 1 (velocity shear), in order to keep changes of the model velocity shear small enough and still achieve realistic model temperature and salinity fields. Changes of the weights α_i of smoothness terms also were necessary to obtain reasonably smooth fields (see Fig. 30) while not compromising the other terms of the cost function too much. The final choice of weights α_i is to a certain extend subjective. One purpose of presenting the UPW model solution in detail (Figs. 17 to 22, 31 and 32) was to defend the particular choice of α_i by showing that the different requirements on the model solution are met satisfactorily.

The absolute flow velocities obtained by the model show a meridional overturning cell consisting of deep water formation in the Nordic Seas, export of deep water across the sills between Greenland, Iceland and Scotland and southward flow of NADW in the Atlantic. The NADW flow is compensated by northward flows of near-surface, intermediate and bottom water and by inflow through Bering Straits into the Arctic Ocean. The model transport rates of deep water from the Nordic Seas into the north Atlantic (8 Sv) and of AABW into the Brazilian Basin (3 Sv) are nearly identical for all model runs performed and are in good agreement with literature values.

All model solutions for the different numerical experiments indicate that at 30°N the northward flow compensating for the southward export of NADW is predominantly occuring in the warm surface layer. In the south Atlantic at 30°S, however, for all numerical experiments the northward flow in the upper 1500 m depth consists mainly of AAIW with only a small contribution of warm surface water (cold water path). This result is consistent with Schmitz and Richardson (1991) who claim that 45% (13 Sv) of the Florida Current transport are derived from AAIW thereby requiring a large northward flow of AAIW into the north Atlantic. The dominance of the northward transport of AAIW over the warm, near-surface water in the model solutions is in disagreement with Gordon (1986) who proposes that the southward flow of NADW is compensated mainly by northward flow within the upper layer (warm-water path), both in the north and south Atlantic.

The silicate distribution in the south Atlantic at 30°S (Fig. 24) together with a silicate budget of the Atlantic north of this latitude (assuming that this area is neither a major sink nor source for silicate) can be used to exclude such a scenario. Rough estimates of average silicate concentrations of the major water masses from Fig. 24 (surface layer: 2, AAIW: 30, NADW: 35, AABW: 100 μmol kg^{-1}) show that the net southward silicate transport by NADW and AABW flows can not be balanced by near-surface water because of negligible silicate content. Instead, a large input of silicate-rich water (AAIW) is required. Using transports from Table 7 (UPW) and the concentrations listed above, the required average silicate concentration of the AAIW component is estimated to be 25 μmol kg^{-1} which corresponds closely with silicate measurements in the core of the AAIW layer (see Fig. 24). In a later paper (Gordon *et al.*, 1992), the authors, on the basis of hydrographic and chlorofluoromethane data, draw a conclusion in line with present model transport estimates and silicate budget considerations and state that "the main supply of upper layer water crossing the Atlantic equator, compensating for Atlantic export of NADW, is drawn from AAIW". Because AAIW and AABW have lower salinities than NADW, at first sight, the dominance of Antarctic waters compensating for the southward export of NADW appears to be in conflict with salt conservation in the Atlantic. However, this potential conflict is resolved assuming that the Atlantic is a net evaporation basin, as observed in the model solutions (fresh-water loss about 0.2 Sv) as well as in other studies (Schmitt *et al.*,1989; Baumgartner and Reichel, 1975; Broecker *et al.*, 1990; Manabe and Stauffer, 1988).

Model vertical velocities show downward motion of deep water south of the overflows, net near-surface sinking in the centers of the subtropical gyres, upwelling in the equatorial region in the upper 500 m depth and upwelling in all depths at about 60°S around

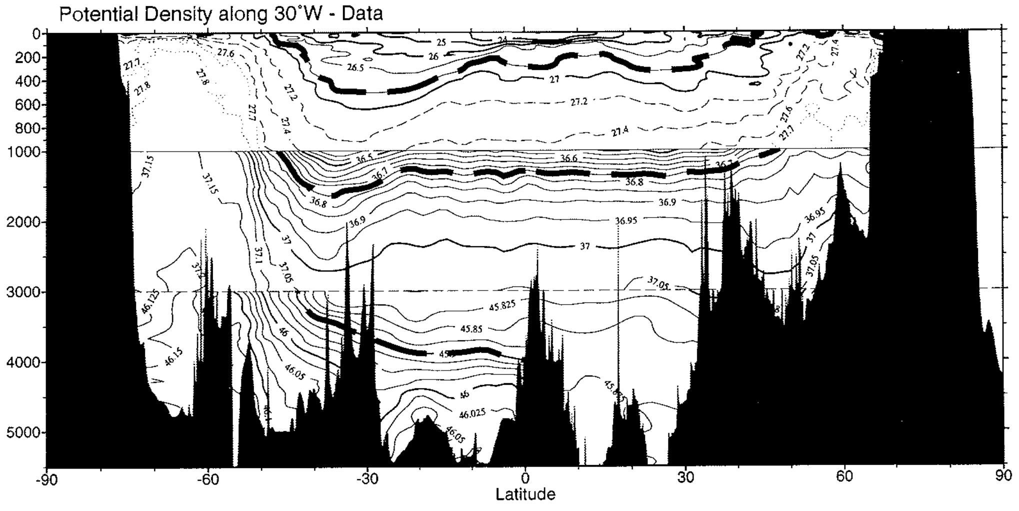

Fig. 43: Meridional section of potential density σ_0 (depth range 0 – 1000 m), σ_2 (1000 – 3000 m) and σ_4 (3000 m – bottom) along 30°W obtained from hydrographic station data. Layer interfaces used for transport estimates in Tables 4 and 7 are indicated by thick dashed lines.

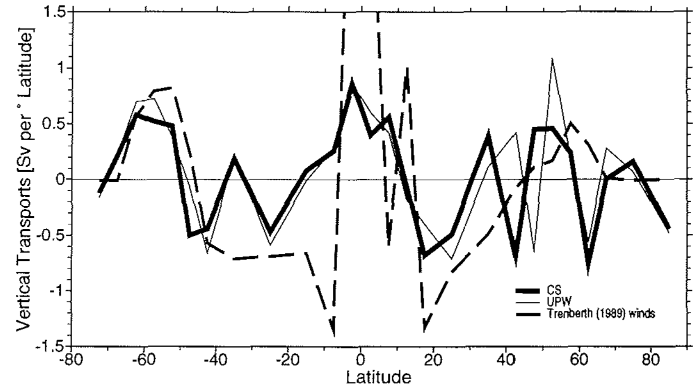

Fig. 44: Zonally integrated vertical transports (in Sv per degree latitude) in 60 m depth for the CS and UPW model solutions and for Ekman pumping based on Trenberth *et al.* (1989) winds. Positive values indicate upward transport.

Antarctica. The upwelling rates in the southern south Atlantic and in the equatorial band are consistent with independent estimates. Comparison of zonally integrated model flows (see Figs. 40a and 40b) with a meridional section of potential density along 30°W derived from the hydrographic station data (Fig. 43) shows that the orientation of vector averaged meridional and vertical model flows in most regions is in surprisingly good agreement with the orientation of isopycnals (see for instance the nearly horizontal southward flow of NADW between about 50°N and 30°S, the upward sloping of the NADW layer at about 45°S, the 'V-shape' flow patterns in the upper 1000 m depth between 50°S and 10°S and between 20°N and 40°N, etc.).

Zonally integrated vertical transports in 60 m depth are shown in Fig. 44 as a function of latitude together with the (zonally integrated) Ekman pumping calculated with the Trenberth *et al.* (1989) winds. Apart from the relatively large scatter of model values north of about 30°N and apart from the unreliable Ekman pumping estimates in the vicinity of the equator model curves and wind-derived Ekman pumping show similar spatial patterns of vertical motion including net upwelling between about 45 and 60° in the south and north Atlantic as well as in the equatorial region and downwelling in the south and north Atlantic subtropical gyres. It should be noted that in the model the vertical velocities are ultimately determined by the requirements to conserve mass and to reproduce realistic fields of temperature and salinity and that they are not directly induced by density gradients. The close similarity between orientation of zonally integrated model flows and the slopes of isopycnals as well as the overall agreement of model vertical transports in 60 m depth with the Ekman pumping calculated from wind data is remarkable especially because there are no explicit constraints on the w's that would enforce this behavior.

Model experiments CS and CS-H have shown that acceptable solutions differing substantially in the strength of the meridional overturning cell and in the magnitudes of the northward heat transport can be found. This indicates that the respective parameters meridional overturning and meridional heat flux are not well determined by a model based on the principle of geostrophy and including temperature and salinity data only. This finding is in line with results from inverse models that yield similar or even larger value ranges for mass and heat transports (Wunsch, 1984a; Wunsch, 1984b; Schlitzer, 1988). Also, large uncertainties of model determined mixing coefficients as observed in the model sensitivity runs (±100%) have been found in other studies as well (Olbers *et al.*, 1985; Schlitzer, 1988; Tziperman (1988)). In many cases (including the present model) model and data are consistent with zero mixing coefficients. A strategy for improving model estimates of mass and heat transports is given below.

Except for the few oceanographic parameters (strength of the meridional overturning cell, magnitude of meridional heat fluxes and coefficients of iso- and diapycnal mixing) for which dedicated sensitivity runs have been performed, for many other model parameters the ranges of acceptable values are still to be determined. Study of the variability of respective values from different numerical experiments yields some information on parameter uncertainty, however, a rigorous sensitivity and resolution analysis requires the calculation of eigenvalues and eigenvectors of the Hessian matrix $\mathbf{H} = \{\partial F/\partial p_i^* p_j^*\}$ (Thacker, 1988b; Tziperman and Thacker, 1989). The eigenvectors associated with the largest eigenvalues reveal those model parameters (or linear combinations of model parameters) that are well determined by the model, and the eigenvectors associated with very small eigenvalues reveal the model parameters (or linear combinations of parameters) for which no information is contained in the system and which can not be determined by the model. Computation of the Hessian $\mathbf{H}$ and its eigenvalues and eigenvectors for the size of the present model is very costly and beyond the scope of this study. Here, the main purpose is to demonstrate the feasibility of implementing the present model concept for a large region of the ocean, to show that satisfactory solutions can be obtained with moderate computational resources and that oceanographically useful information can be drawn from the model results.

It was noted repeatedly above that the spatial resolution of the present model is insufficient to allow proper representation of narrow boundary currents at the ocean surface (Brazil Current, Labrador Current, etc.) and in the deep ocean (deep western boundary current). This is clearly seen in the field of reference velocities at 2500 m depth shown in Fig. 23 (section 5.2.3). Underestimation of the deep western boundary current is seen as a possible explanation for the relatively weak southward transport of NADW in the standard run. A regional model of the Gulf Stream area with a higher spatial resolution (2° by 1° in longitude and latitude) was set up to demonstrate that inadequate resolution and underestimation of boundary currents is not a principle defect of the present model concept but just a matter of the grid size of the model. Absolute flow velocities in 3000 m depth for this higher resolution model are displayed in Fig. 45 and show a well developed, coherent southwestward flowing boundary current and the internal recirculation (for comparison see Wunsch and Grant, 1982 and Hogg, 1983). Mean velocities in the boundary current amount to between 3 and $6 \cdot 10^{-2}$ m s^{-1} and are much larger than deep flow velocities in this area for the Atlantic model (Fig. 23).

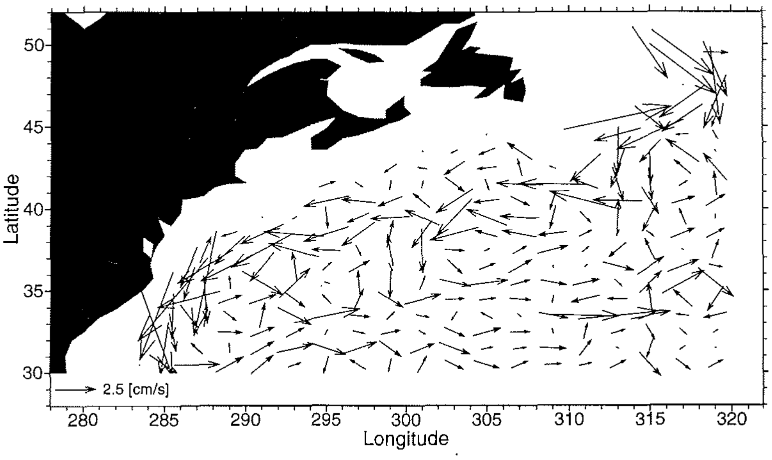

Fig. 45: Model velocities in 3000 m depth for a regional Gulf Stream model with 2°longitude by 1°latitude horizontal resolution. Arrows are vector averages of nearby zonal and meridional flows.

Apart from horizontal resolution the vertical grid spacing of the model is of concern especially in areas where thin layers of distinct water masses are found. Regions deserving special considerations are, for instance, Denmark Strait and Iceland-Scotland-Ridge in the north Atlantic where cold and dense southward flowing waters are observed in layers less than about 100 m thick just above the bottom (Worthington, 1969). In these areas, a large vertical grid spacing at the depth of the sill prohibits the correct representation of water masses because of averaging over too large depth ranges (bottom layer will be too warm) and is expected to lead to difficulties producing the correct NADW water-mass characteristics south of the overflows.

Given the relatively large value ranges for some important oceanographic parameters (meridional overturning, integrated mass and heat transports, mixing coefficients), all leading to roughly the same size of the cost function, it seems necessary for a better determination of these parameters to include additional, independent information like observations of nutrients and transient tracers (tritium and chlorofluoromethanes) in the present formalism. Common characteristics of transient tracers are their anthropogenic origin, vanishing natural concentrations and the time-dependent input into the ocean at the air-sea interface. It has been shown (Weiss *et al.*, 1985; Schlitzer *et al.*, 1991) that chlorofluoromethanes (CFMs) can be used to trace deep water flows and it is hoped that these data help to constrain deep water flow rates. Then, finding a circulation that is basically geostrophic but additionally reproduces the correct temperature, salinity, nutrient and tracer distributions can be regarded as an extended, automated version of Reid's (1989) method of manually choosing reference velocities in accordance with a wide variety of property fields. An advantage over Reid's method is that the resulting circulation fields of the model are guaranteed to be mass conserving and consistent with air-sea *E-P* estimates but also contain information on the vertical flows in the ocean as shown above.

A simulation of CFM-11 has been performed using flow field and mixing coefficients of the CS experiment. Results of this calculation along about 22°W in the Atlantic north of 10°S are shown in Fig. 46 together with data from Doney and Bullister (1992). The model CFM-11 distribution exhibits the overall features found in the observed field, namely high concentrations at the ocean surface, penetration of CFM-11 down to the bottom at high latitudes due to deep water formation, further sinking south of the overflows and a southward extending tongue of CFM-rich water indicating the southward spreading of NADW. A closer comparison of the two distribution, however, reveals significant differences. For instance, the model is not able to reproduce the relatively high CFM-11 concentrations down to about 800 m depth found in the observations north of 30°N probably because of missing deep reaching winter convection in the model, and in the depth range of the Upper North Atlantic Deep Water (UNADW: about 1400 to 2200 m depth) the tongue of CFM-rich water does not extend far enough south indicating that the southward spreading of NADW in the CS solution is too weak. Fig. 46 demonstrates that CFM data contain additional information not yet exploited in a model based on temperature and salinity data only and inclusion of nutrient and tracer data will help to constrain oceanic mass and heat transports better. Technological advances are expected to allow runs of an Atlantic model with much higher horizontal and vertical resolution including nutrients and transient tracers in addition to temperature and salinity on workstation-type computers in the near future.

CFM-11 [pmol kg^{-1}]

(a) OCEANUS 202 - Jun/88

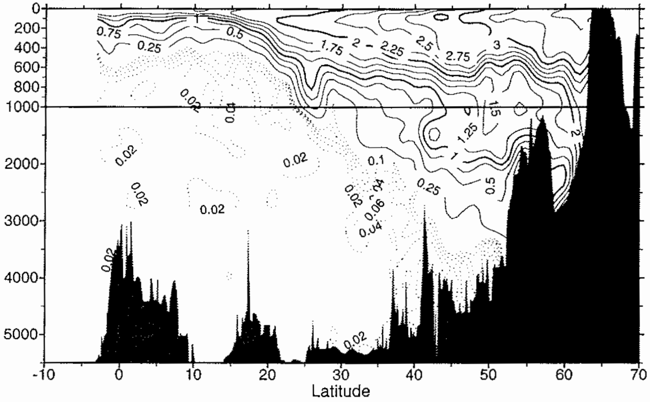

(b) MODEL 22°W - Mar/89

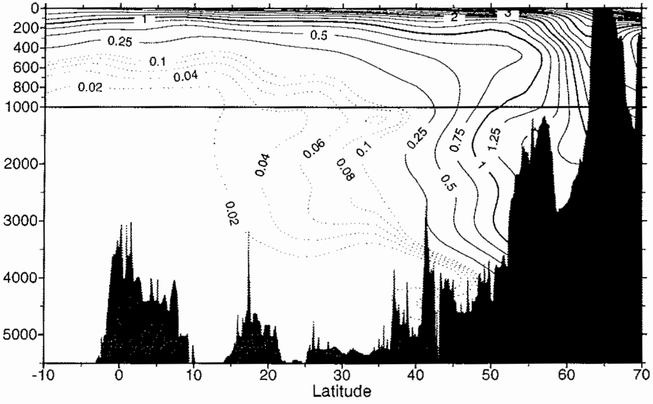

Fig. 46: (a) Meridional section of chlorofluoromethane CFM-11 from *Oceanus* cruise 202 (June, 1988; about 23°W; redrawn from Doney and Bullister, 1992) and (b) model distribution (CS) of CFM-11 along 22.5°W for March 1989. Note scale change of the vertical axis at 1000 m depth.

Acknowledgments

I would like to thank Prof. W. Roether for the invaluable support he provided me throughout the course of this research. I appreciate the independence he allowed me to develop and pursue new ideas, and I am grateful for his continuing encouragement and advice.

I have benefited greatly from many discussions with other scientists. Thanks are due to Carl Wunsch, Eli Tziperman, Jürgen Willebrand, Carlisle Thacker, Dirk Olbers, Olivier Talagrand and Jens Schröter. Wolfgang Roether, Carl Wunsch and Jochem Marotzke carefully read an early version of this manuscript. Their useful comments helped me to improve the presentation of model setup and results.

I am grateful to Worth Nowlin and Joe Reid who contributed hydrographic station data to be used in this study. Jean Charles Gilbert and Claude Lemaréchal provided the software of an efficient and reliable variable-storage quasi-Newton descent algorithm, and the Alfred-Wegener-Institute, Bremerhaven made computational resources available to me for performing the first model runs.

Thanks are also due to my colleagues in our group who have helped to create a relaxed working environment. Frequent coffee hours and (sometimes seemingly endless) discussions on the meaning of life and other related topics made an average working day enjoyable and were welcome diversions from the serious task of scientific research.

My special thanks go to my dear friend Sabine Vanselow. Her love and affection gave me the strength and endurance necessary to complete this work.

I want to dedicate this habilitation thesis to my parents Frieda and Willi Schlitzer who have supported my education through all the years.

References

Baumgartner, A. and E. Reichel, 1975: *The World Water Balance,* Oldenbourg–Verlag, Munich, Federal Republic of Germany.

van Bennekom, A. J. and G. W. Berger, 1984: Hydrography and silica budget of the Angola Basin, Neth. J. Sea Res., 17, 149–200.

Broecker, W. S., T.-H. Peng, J. Jouzel and G. Russel, 1990: The magnitude of global fresh-water transports of importance to ocean circulation, *Clim. Dyn., 4,* 73–79.

Broecker, W. S., 1979: A revised estimate for the radiocarbon age of North Atlantic deep water, *J. Geophys. Res., 84,* 3218–3226.

Bryan, K., 1969: Climate and the ocean circulation, III., The ocean model, *Mon. Weath. Rev., 97,* 806–827.

Bunker, A. F., 1988: Surface energy fluxes of the south Atlantic Ocean, *Monthly Weather Rev., 116,* 809–823.

Bunker, A. F., 1976: Computations of surface energy flux and annual air-sea interaction cycles of the North Atlantic Ocean, *Mon. Weath. Rev., 104,* 1122–1140.

Burkov, V. A., R. P. Bulatov and V. G. Neiman, 1973: Large-scale features of water circulation in the world ocean, *Oceanology, 13,* 325–332.

Coachman, L. K. and K. Aagaard, 1974: Physical oceanography of arctic and subarctic seas, in *Marine Geology and Oceanography of the Arctic Seas,* Springer–Verlag, New York, pp. 1–72.

Deacon, G. E. R., 1937: The hydrology of the Southern Ocean, *Discovery Reports, 15,* 1–124.

Defant, A., 1941: Quantitative Untersuchungen zur Statik und Dynamik des Atlantischen Ozeans. Die absolute Topographie des physikalischen Meeresniveaus und der Druckflächen sowie die Wasserbewegungen im Raum des Atlantischen Ozeans, in *Wissenschaftliche Ergebnisse der Deutschen Atlantischen Expedition auf dem Forschungs- und Vermessungsschiff "Meteor" 1925-27,* 6:2nd Part, 1, pp. 191–260.

Doney, S. C. and J. L. Bullister, 1992: A chlorofluoromethane section in the eastern North Atlantic, *Deep Sea Res., 39,* 1857–1883.

Fofonoff, N. P., 1981: The Gulf Stream system, in *Evolution of Physical Oceanography: Scientific Surveys in Honor of Henry Stommel,* edited by B. Warren and C. Wunsch, MIT Press, Cambridge, Mass., pp. 112–139.

Fukumori, I., F. Martel, and C. Wunsch, 1991: The hydrography of the north Atlantic in the early 1980s. an atlas., *Prog. Oceanog., 27,* 1–110.

Gargett, A. E., 1984: Vertical eddy diffusivity in the ocean interior, *J. Mar. Res., 42,* 359–393.

Gargett, A. E. and G. Holloway, 1984: Dissipation and diffusion by internal wave breaking, *J. Mar. Res., 42,* 15–27.

Gilbert, J. Ch. and C. Lemaréchal, 1989: Some numerical experiments with variable-storage quasi-Newton algorithms, *Mathematical Programming*, *45*, 407–435, 1989.

Gordon, A. L., R. F. Weiss, W. M. Smethie, and M. J. Warner, 1992: Thermocline and intermediate water communication between the south Atlantic and Indian oceans, *J. Geophys. Res., 97,* 7223–7240.

Gordon, A. L., 1986: Interocean exchange of thermocline water, *J. Geophys. Res., 91,* 5037–5046.

Gordon, A. L., E. J. Molinelli, and T. N. Baker, 1986: *Southern Ocean Atlas,* Amerind Publishing Co., New Dehli.

Gordon, A. L., 1971: Oceanography of antarctic waters, in: *Antarctic Research Series, Vol 15,* edited by J. Reid, American Geophysical Union, Washington, D.C. pp. 169–203.

Hall, M. M. and H. L. Bryden, 1982: Direct estimates and mechanisms of ocean heat transport, *Deep Sea Res., 29,* 339–359.

Hastenrath, S., 1982: On meridional heat transports in the World Ocean, *J. Phys. Oceanogr., 12,* 922–927.

Hellermann, S., 1973: The net meridional flux of water by the oceans from evaporation and precipitation estimates, *unpublished manuscript.*

Hestenes, M. R., 1975: *Optimization Theory,* John Wiley & Sons, Inc., New York.

Hogg, N. G., 1983: A note on the deep circulation of the western North Atlantic: its nature and causes, *Deep Sea Res., 30,* 945–961.

Hogg, N. G., P. Biscaye, W. Gardner, and W. J. Schmitz Jr., 1982: On the transport and modification of Antarctic Bottom Water in the Vema Channel, *J. Mar. Res., 40*(suppl), 231–263.

Hsiung, J., 1985: Estimates of global oceanic meridional heat transport, *J. Phys. Oceanogr., 15,* 1405–1413.

Kawase, M., 1987: Establishment of deep ocean circulation driven by deep water production, *J. Phys. Oceanogr., 17,* 2294–2317.

Le Dimet, F. and O. Talagrand, 1986: Variational algorithms for analysis and assimilation of meteorological observations: theoretical aspects, *Tellus, 38,* 97–110.

Leaman, K. D., E. Johns, and T. Rossby, 1989: The average distribution of volume transport and potential vorticity with temperature at three section across the Gulf Stream, *J. Phys. Oceanogr., 19,* 36–51.

Levitus, S., 1982, Climatological atlas of the world ocean, *Prof. Pap. 13*, Natl. Oceanic and Atmos. Admin., Rockville, Md..

Manabe, S. and R. J. Stauffer, 1988: Two stable equilibria of a coupled ocean-atmosphere model, *J. Climate, 1,*, 841–866.

Menke, W., 1984: Geophysical Data Analysis: Discrete Inverse Theory, Academic, San Diego, Calif..

Munk, W. H., 1966: Abyssal recipes, *Deep Sea Res., 13,* 707–730.

Niiler, P. P. and W. S. Richardson, 1973: Seasonal variability of the Florida Current, *J. Mar. Res., 31,* 144–167.

Nowlin, W. D., T. Whitworth III, and R. D. Pillsbury, 1977: Structure and transport of the Antarctic Circumpolar Current at Drake Passage from short-term measurements, *J. Phys. Oceanogr., 7,* 788–802.

Oberhuber, J. M., 1988: *An atlas based on the COADS data set: the budgets of heat, buoyancy and turbulent kinetic energy at the surface of the global ocean,* Technical Report 15, Max-Planck-Institut für Meteorologie, Hamburg.

Olbers, D. and M. Wenzel, 1989: Determining diffusivities from hydrographic data by inverse methods with applications to the Circumpolar Current, in *Oceanic Circulation Models: Combining Data and Dynamics*, edited by D. L. T. Anderson and J. Willebrand, Kluwer Academic Publishers, Dordrecht, pp. 95–139.

Olbers, D. J., M. Wenzel, and J. Willebrand, 1985: The inference of north Atlantic circulation patterns from climatological hydrographic data, *Rev. Geophys., 23,* 313–356.

Pacanowski, R. C. and S. G. H. Philander, 1981: Parameterization of vertical mixing in numerical models of tropical oceans, *J. Phys. Oceanogr., 11,* 1443–1451.

Paige, C. C. and M. A. Saunders, 1982: LSQR: An algorithm for sparse linear equations and sparse least squares, *ACM Trans. Math. Softw., 8,* 43–71.

Peterson, R. G. and T. Whitworth III, 1989: The Subantarctic and Polar Fronts in relation to deep water masses through the southwestern Atlantic, *J. Geophys. Res., 94,* 10,817–10,838.

Peterson, R. G. and L. Stramma, 1991: Upper-level circulation in the south Atlantic ocean, *Prog. Oceanog., 26,* 1–73.

Redi, M. H., 1982: Oceanic isopycnal mixing by coordinate rotation, *J. Phys. Oceanogr., 12,* 1154–1158.

Reid, J. L., 1989: On the total geostrophic circulation of the south Atlantic ocean: flow patterns, tracers, and transports, *Prog. Oceanog., 23,* 149–244.

Reid, J. L., 1981: On the mid-depth circulation of the world ocean, in *Evolution of Physical Oceanography: Scientific Surveys in Honor of Henry Stommel,* B. Warren and C. Wunsch (eds.), MIT Press, Cambridge, Mass., 70–111.

Richardson, P. L., 1985: Average velocity and transport of the Gulf Stream near 55°N, *J. Mar. Res., 43,* 83–111.

Richardson, P. L. and D. Walsh, 1986: Mapping climatological seasonal variations of surface currents in the tropical Atlantic using ship drifts, *J. Geophys. Res., 91,* 10,537–10,550.

Rintoul, S. R., 1991: South Atlantic interbasin exchange, *J. Geophys. Res., 96,* 2675–2692.

Roache, P. J., 1982: *Computational Fluid Dynamics,* Hermosa Publishers, Albuquerque, New Mexico.

Roemmich, D., 1983, The balance of geostrophic and Ekman transports in the tropical Atlantic ocean, *J. Phys. Oceanogr., 13,* 1534–1539.

Roemmich, D. and C. Wunsch, 1985: Two transatlantic sections: Meridional circulation and heat flux in the subtropical North Atlantic Ocean, *Deep Sea Res.*, 32, 619–664.

Sarmiento, J. L., 1986: On the north and tropical Atlantic heat balance, *J. Geophys. Res., 91,* 11,677–11,689.

Sarmiento, J. L. and K. Bryan, 1982: An ocean transport model for the North Atlantic, *J. Geophys. Res., 87,* 394–408.

Sarmiento, J. L., H. W. Feely, W. S. Moore, A. E. Bainbridge and W. S. Broecker, 1976: The relationship between vertical eddy diffusion and buoyancy gradient in the deep sea, *Earth Planet. Sci. Lett., 32,* 357–370.

Schlitzer, R., W. Roether, H. Oster, H. G. Junghans, M. Hausmann, H. Johannsen and A. Michelato, 1991: Chlorofluoromethane and oxygen in the eastern Mediterranean, *Deep Sea Res., 12,* 1531–1551.

Schlitzer, R., 1989: Modeling the nutrient and carbon cycles of the north Atlantic. 2. New production, particle fluxes, CO_2 gas exchange, and the role of organic nutrients, *J. Geophys. Res., 94,* 12,781–12,794.

Schlitzer, R., 1988: Modeling the nutrient and carbon cycles of the north Atlantic. 1. Circulation, mixing coefficients, and heat fluxes, *J. Geophys. Res., 93,* 10,699–10,723.

Schlitzer, R., 1987: Renewal rates of east Atlantic deep water estimated by inversion of ^{14}C data, *J. Geophys. Res., 92,* 2953–2969.

Schlitzer, R., 1993: Objective analysis with variable scale lengths, *manuscript in preparation.*

Schmitt, R. W., P. S. Bogden, and C. E. Dorman, 1989: Evaporation minus precipitation and density fluxes for the north Atlantic, *J. Phys. Oceanogr., 19,* 1208–1221.

Schmitz, Jr., W. J. and P. L. Richardson, 1991: On the sources of the Florida Current, *Deep Sea Res., 38(suppl.),* S379–S409.

Schott, F. and H. Stommel, 1978: Beta spirals and absolute velocities in different oceans, *Deep Sea Res., 25,* 961–1010.

Sverdrup, H. U., 1933: On vertical circulation in the ocean due to the action of the wind with application to conditions within an Antarctic Circumpolar Current, *Discovery Rept., 7,* 139–170.

Swallow, J. C. and L. V. Worthington, 1969: Deep currents in the Labrador Sea, *Deep Sea Res., 16,* 77–84.

Tchernia, P., 1980: *Descriptive Regional Oceanography,* Pergamon, Oxford.

Thacker, W. C., 1988a: Fitting models to inadequate data by enforcing spatial and temporal smoothness, *J. Geophys. Res., 93,* 10,655–10,665.

Thacker, W. C., 1988b: *Three lectures on fitting numerical models to observations,* Technical Report GKSS 87/E/65, GKSS Forschungszentrum, Geesthacht.

Trenberth, K. E., J. G. Olson, and W. G. Large, 1989: *A global ocean wind stress climatology based on ECMWF analyses,* Technical Report NCAR/TN-338+STR, National Center for Atmospheric Research, Boulder.

Tsuchiya, M., 1989: Circulation of Antarctic Intermediate Water in the north Atlantic Ocean, *J. Mar. Res., 47,* 747–755.

Tziperman, E., 1988: Calculating the time-mean oceanic general circulation and mixing coefficients from hydrographic data, *J. Phys. Oceanogr.*, 18, 519–525.

Tziperman, E. and W. C. Thacker, 1989: An optimal control/adjoint-equations approach to studying the oceanic general circulation, *J. Phys. Oceanogr., 19,* 1471–1485.

Warner, M. J. and R. F. Weiss, 1992: Chlorofluoromethanes in south Atlantic Antarctic Intermediate Water, *Deep Sea Res., 39,* 2053–2075.

Warren, B., 1981: Deep circulation of the world ocean, in *Evolution of Physical Oceanography: Scientific Surveys in Honor of Henry Stommel*, B. Warren and C. Wunsch (eds.), MIT Press, Cambridge, Mass., 6–41.

Weiss, R. F., J. L. Bullister, R. H. Gammon, and M. J. Warner, 1985: Atmospheric chlorofluoromethanes in the deep equatorial Atlantic, *Nature, 314,* 608–610.

WOCE, 1988: World Ocean Circulation Experiment. Implementation Plan, Vol. I, Technical Report WMO/TD No. 242, World Meteorological Organization.

Worthington, L. V., 1970: The Norwegian Sea as a mediterranean basin, *Deep Sea Res., 17,* 77–84.

Worthington, L. V., 1969: An attempt to measure the volume transport of Norwegian Sea overflow water through the Denmark Strait, *Deep Sea Res., 16*(suppl.), 421–432.

Wunsch, C., 1984a: An eclectic Atlantic Ocean circulation model, Part I, The meridional flux of heat, *J. Phys. Oceanogr., 14,* 1712–1733.

Wunsch, C., 1984b: An estimate of the upwelling rate in the equatorial Atlantic based on the distribution of bomb radiocarbon and quasi-geostrophic dynamics, *J. Geophys. Res., 89,*, 7971–7978.

Wunsch, C. and J.-F. Minster, 1982: Methods for box models and ocean circulation tracers: Mathematical programming and nonlinear inverse theory, *J. Geophys. Res.*, *87,* 5747–5762.

Wunsch, C. and B. Grant, 1982: Towards the general circulation of the north Atlantic ocean, *Prog. Oceanogr., 11,* 1–59.

Wüst, G., 1935: Wiss. Ergeb. Dtsch. Atlantischen Exped. Forschungs- und Vermess. Meteor 1925-1927, 6(1st part, 2), p. 180 , (English translation by the Al-Ahram Center for Scientific Translations, 1978) in *Schichtung und Zirkulation des Atlantischen Ozeans: Die Stratosphäre,* edited by W. J. Emery, Amerind, New Delhi, pp. 112.